NORTHWESTERN UNIVERSITY

Factors Modifying Neurodevelopmental Disorder-Related Phenotypes in *Scn2a K1422E* Mice

A DISSERTATION

SUBMITTED TO THE GRADUATE SCHOOL
IN PARTIAL FULFILLMENT OF THE REQUIREMENTS

for the degree

DOCTOR OF PHILOSOPHY

Neuroscience

By

Dennis Michael Echevarria-Cooper

EVANSTON, ILLINOIS

June 2023

Abstract

SCN2A encodes the Nav1.2 voltage-gated sodium channel, which is thought to contribute to the development of the central nervous system. Pathogenic variants in *SCN2A* have been associated with neurodevelopmental disorders (NDD), including developmental and epileptic encephalopathies (DEE), intellectual disability (ID), and autism spectrum disorder (ASD). These disorders represent a significant public health burden, affecting roughly 1 in 6 children in the United States. However, the pathogenic mechanisms of *SCN2A* variants are complex and require further elucidation. For example, sex differences have been reported in a number of NDD, including epilepsy and ASD. Furthermore, recurrent and inherited variants in *SCN2A* show wide phenotypic heterogeneity among individuals. This suggests that genetic and environmental factors may contribute to variable expressivity of the phenotype.

Some *SCN2A* variants fit into a framework wherein gain-of-function missense variants that increase neuronal excitability lead to DEE, while loss-of-function variants that reduce neuronal excitability lead to ID/ASD. One unique case less easily classified using this framework is the *de novo* missense variant *SCN2A*-p.K1422E, associated with infant-onset developmental delay, infantile spasms, and features of ASD. Prior structure-function studies demonstrated that K1422E substitution alters Nav1.2 ion selectivity, conferring calcium permeability, lowering overall conductance, and conferring resistance to tetrodotoxin (TTX). As part of this work and based on heterologous expression data, a compartmental neuron model incorporating K1422E channels was developed that predicted reductions in peak action potential (AP) speed. To further investigate the effects of the p.K1422E variant on cellular excitability and neurological/neurobehavioral phenotypes, a novel mouse model ($Scn2a^{K1422E}$) was generated using CRISPR/Cas9 genome

editing. Excitatory neurons in neocortex exhibited features indicative of functional K1422E-containing Nav1.2 channels, including lower current density with a TTX-insensitive component, reduced AP speed, and aberrant calcium influx occurring during the Nav-mediated rising phase of the AP. Analysis of behaving animals revealed a mix of phenotypes, including infrequent spontaneous seizures, altered susceptibility to chemically induced seizures, reduced anxiety-like behavior and alterations in olfactory-guided social behavior.

Scn2a^{K1422E} females showed a reproducible, non-unimodal distribution of flurothyl-induced seizure thresholds. Women with epilepsy often show a cyclical pattern of altered seizure susceptibility during specific phases of the menstrual cycle which can be attributed to fluctuations in hormones and corresponding changes in neurosteroid levels. To determine whether the estrous cycle affects susceptibility to flurothyl-induced seizures, estrous cycle monitoring was performed in female mice that had undergone ovariectomy (OVX), sham surgery, or no treatment prior to seizure induction. Removing the influence of circulating sex hormones via OVX did not affect the non-unimodal distribution of flurothyl seizure thresholds observed in *Scn2a*^{K1422E} females. Additionally, flurothyl seizure thresholds were not associated with estrous cycle stage in mice that underwent sham surgery or were untreated. Interestingly, untreated *Scn2a*^{K1422E} females showed evidence of disrupted estrous cyclicity, an effect not previously described in a genetic epilepsy model.

Genetic modifiers can contribute to variability in disease phenotypes associated with rare driver mutations. Accordingly, different genetic backgrounds across inbred rodent strains have been shown to influence disease-related phenotypes, including those associated with *Scn2a*-related

NDD. The *Scn2a*^{K1422E} mouse model was developed as an isogenic line maintained on the C57BL/6J (B6) strain. To determine if background strain affects phenotype severity in the *Scn2a*^{K1422E} mouse model, phenotypes of *Scn2a*^{K1422E} mice on B6 and [DBA/2J×B6] F1 hybrid strains were compared. Convergent evidence from neurobehavioral assays demonstrated lower anxiety-like behavior in *Scn2a*^{K1422E} mice compared to WT and further suggested that this effect is more pronounced on the B6 background compared to the F1D2 background. Although there were no strain-dependent differences in occurrence of rare spontaneous seizures, response to the chemoconvulsant kainic acid (KA) revealed differences in seizure generalization and lethality risk, with variation based on strain and sex.

The work described in this dissertation establishes the *Scn2a*^{K1422E} mouse model as a sharable resource for future studies on the consequences of altered Nav1.2 ion selectivity and serves as a case study highlighting the importance of considering modifying factors of disease phenotypes that present as complex traits. Continued examination of phenotypic heterogeneity in the *Scn2a*^{K1422E} mouse model using diverse genetic reference panels may enable the identification of highly penetrant phenotypes and modifier genes that could provide clues about the primary pathogenic mechanism of the K1422E variant. In addition, examining strain level effects could reveal genetic backgrounds with unique susceptibility profiles that would be relevant for future studies on specific traits such as seizure susceptibility. Properly validated animal models can help refine genotype-phenotype correlations for *SCN2A*-related disorders, enhance our understanding of disease mechanisms, and support the development of targeted therapeutic strategies.

Acknowledgments

The work described herein was completed with an immense amount of personal and professional support from a truly inspiring cohort of family, friends, and mentors. This achievement belongs to all of them; may it stand forever as a tribute to their hard work and dedication.

Lucky by Dennis Echevarria-Cooper

As I finish my PhD training, near the end of my 30th year
I think about what brought me here
And one thing comes to mind: luck

I am lucky to have parents and grandparents who understand the value of education
Not as a means of making money, but as a way to broaden my horizons
Who taught me to take responsibility
To not hesitate in the face of the inordinately obstructive
And that neither distance nor death can diminish the support of family

I am lucky to have brothers (and sisters) who have shared my struggles
Paragons of hard work, and of thinking outside the box
Of caring for others, and of pursuing passion

I am lucky to have the most adorable niece in the world
Who reminds me to live life fully
And that we were not put here to suffer fools

I am lucky to have old friends who exist outside this bubble
Chosen family who lift me up and hear me out
And who aren't afraid to put me in my place

I am lucky to have new friends made inside the bubble
Contemporaries in asking hard questions and making poor choices
Who find beauty in the absurd, and meaning in chaos

I am lucky to have had two labs worth of coworkers and teachers
Showing me the ropes of mouse wrangling
Teaching me E-phys for the tenth time
Making games out of arrival announcements
Or finding folly in the latest film

I am lucky to have had a fair and balanced committee
Scientists of superior quality
Always building me up, never tearing me down

I am lucky to have had a mentor beyond compare
Who took in a headstrong novice
Loud, with a talent for theatrics
And taught him the dignity of quiet confidence in carefully cultivated expertise
A master class in mentoring based on mentee needs
Who always saw me as a person first
Through pandemic and injury
Through failure and triumph

And finally I am lucky that on day one of this journey
I met the love of my life
And exactly two years later
She became my wife
My partner in bothering animals
My kayak comrade
My daily reminder to stop and rest
I owe you my life
And will spend the rest of it loving and supporting you

Thank you

Shiloh Echevarria-Cooper PhD

Sylvia Echevarria-Cooper

Jack Echevarria-Cooper

Barbara Gonzalez MA

Franklin Echevarria

Barbarita Rodriguez Rodriguez

Juan Gerardo Gonzalez PhD

Aida Rosado-Echevarria MA

Franklin Echevarria

Franklin Echevarria PhD

Kenneth Echevarria MS RDN

Mary Stewart Montague MD

Avery Korns MS

Aida Carolina Echevarria

John Cotton III

Steve Rakow

John Cotton II

Velrah Cotton

Melissa Rakow

Ashley Cotton

Rogan Grant

Lynn Ren PhD

Sarah Lurie PhD

Jennifer Kearney PhD

Alfred George Jr. MD

Geoffrey Swanson PhD

Alicia Guemez Gamboa PhD

Kevin Bender PhD

Nicole Hawkins PhD

Christopher Thompson PhD

Sunita Misra MD PhD

Sam Kang PhD

Erin Baker PhD

Levi Barse MBS MSL

Alexandra Huffman

Tyler Thaxton

Sam Duarte

Nathan Speakes

Conor Dixon

The George Lab

The NUIN Program

Sally McIver PhD

The CLIMB Program

Toni Gutierrez PhD

List of Abbreviations

AIS: axon initial segment
ASD: autism spectrum disorder
ANOVA: analysis of variance
AP: action potential
B6: C57BL/6J mouse strain
Cas9: CRISPR associated protein 9
CRISPR: Clustered Regularly Interspaced Short Palindromic Repeats
D2: DBA/2J mouse strain
ddPCR: digital drop polymerase chain reaction
DEE: developmental and epileptic encephalopathies
DMEM - Dulbecco's modified Eagle's medium
EEG: electroencephalogram
F1D2: F1 offspring from C57BL/6J.*Scn2a*$^{K1422E/+}$ male × DBA/2J wild-type female
Flurothyl: Bis(2,2,2-trifluoroethyl) ether
GABA: γ-aminobuteric acid
GoF: gain-of-function
GTCS: generalized-tonic clonic seizure
GXTx-1E: guangxitoxin-1E
ID: intellectual disability
IP: intraperitoneal
KA: kainic acid
LoF: loss-of-function
MJ: myoclonic jerk
NDD: neurodevelopmental disorder
OVX: ovariectomy
PCR: polymerase chain reaction
PBS: phosphate buffered saline
PMT: photomultiplier tubes
PTV: protein-truncating variant
RMSE: root-mean-squared error
RT-PCR: reverse transcription-polymerase chain reaction
SC: subcutaneous
SD: standard deviation
SeLFNIE: self-limited familial neonatal infantile epilepsy
SEM: standard error of the mean
SPF: specific pathogen free
SUDEP: sudden unexpected death in epilepsy
TTX: tetrodotoxin
WT: wild-type

For Ben

Hope cannot be synthesized or quantified.

It is something felt, and something given.

Table of Contents

List of Figures

List of Tables

Chapter 1. Introduction

1.1 Background and Significance

Neurodevelopmental disorder-related phenotypes are complex traits

The nervous system is the dynamic interface between many organisms and their environment, responsible for integrating sensory input and homeostatic information as well as coordinating behavioral outputs. Perhaps unsurprisingly, the development and maintenance of this system is a complex and highly regulated process. One can imagine then that disruptions in the development of the nervous system can have a dramatic impact on function. Neurodevelopmental disorders (abbreviated as NDD going forward) are somewhat loosely defined, as illustrated in *DSM-5* where NDD are described as a group of conditions with onset in the developmental period characterized by deficits that produce impairments of functioning[1]. Commonly considered NDD include intellectual disability (ID), Communication Disorders, Autism Spectrum Disorder (ASD), Attention-Deficit/Hyperactivity Disorder, Neurodevelopmental Motor Disorders, and Specific Learning Disorders[1,2]. NDD can have considerable symptom overlap, shared comorbidities, and wide clinical heterogeneity. Rapid advances in molecular biology, genetics, and genomics have revealed substantial genetic contributions to "classical" NDDs that often overlap with other neurological and neuropsychiatric disorders such as early onset epilepsy syndromes and schizophrenia[3–12]. Thus, the classification of NDD is continually being expanded and refined on the basis of shared etiology[2,13].

Semantics aside, NDD represent a significant public health burden, affecting an estimated 1 in 6 children in the United States[14,15]. As previously mentioned, these disorders can often be attributed to genetic abnormalities[3–12]. The unspoken promise of molecular genetics is that a thorough understanding of genotype (i.e., the genetic constitution of an organism, including disease-causing variants) and its contribution to phenotype (i.e., an organism's observable traits, including those associated with disease) will enable more accurate prediction-based treatment decisions that yield better clinical outcomes. The genetic architecture of most NDD is polygenic, with multiple low frequency and/or common genetic variants exerting small to intermediate effects on disease risk in a combinatorial fashion[2,16–18]. As such, disease phenotypes associated with polygenic NDD are complex traits with equally complex genotype correlations. In some cases, rare genetic variants (either inherited or *de novo*) with major effects on the function of a single gene can account for NDD phenotypes[16–18]. One such example is Dravet syndrome, a genetic epilepsy syndrome in which more than 80% of cases are caused by mutations in *SCN1A*[19,20]. One might expect genotype-phenotype correlations to be more readily elucidated in the context of these "monogenic" disorders. In actuality, presumed monogenic disorders often show considerable phenotypic variation and complex genotype-phenotype correlations[21–23]. This suggests that even in NDD with strong driver mutations, disease phenotypes are complex traits influenced by other genes, environmental factors, and the inherent buffering capacity of multilevel biological networks[21–28]. Therefore, our understanding of NDD etiology must involve mechanistic dissection of pathological variants, not in isolation, but in the larger context of pathways and processes that drive complex traits.

Voltage gated sodium channels

Early-onset epilepsy syndromes, ASD, ID, and developmental delay (DD) account for approximately 40% of NDD[14]. Moreover, genetic variants in voltage-gated sodium channels are increasingly associated with these NDD[29–31]. Voltage-gated sodium channels are large, multidomain protein complexes that facilitate plasma membrane depolarization in excitable cell types such as neurons and myocytes. Before the existence of sodium channels, cellular depolarization was mediated by calcium-selective channels or nonselective cation channels[32,33]. As such, changes in membrane potential were linked to alterations in intracellular calcium and associated downstream calcium-dependent signaling. Sodium channels are thought to have evolved in part to allow cells to separate changes in voltage from calcium signaling. The genes encoding voltage-gated sodium channel paralogs are evolutionarily related and basic channel structure is highly conserved across species orthologs[34]. A homology model of channel structure and a schematic of channel functional states originally published in a review by Sanders et al. (2018) [35] are shown in **Figure 1.1**. A 260-kDa alpha subunit forms the voltage-dependent, sodium-selective pore of the channel, while two 30-kDa auxiliary beta subunits modulate channel function and localization[36,37]. The alpha subunit consists of four internally homologous domains (I-IV), each with six transmembrane segments (S1-S6; **Figure 1.1A**). These internal repeat domains are linked by two large cytoplasmic loops (I/II, II/III) as well as a short, highly conserved cytoplasmic linker between domains III and IV[38]. Discrete protein domains critical for channel function have been revealed using site-directed mutagenesis. The extracellular residues linking the S5 and S6 segments of each domain come together to form the pore through which sodium ions travel (**Figure 1.1A & B**)[39]. Sodium selectivity is conferred by a highly conserved filter comprised of four critical residues (Asp-Glu-Lys-Ala or DEKA; **Figure 1.1A & B**)[40]. These channels evolved from a primordial channel with mixed selectivity, where the selectivity filter has a glutamic acid (E) substituted for lysine (K) in the 3rd transmembrane domain[41,42]. Interestingly, some invertebrates express more primitive Nav1 channels containing the DEKA selectivity filter that nevertheless appear to have some calcium permeability[43]. This suggests that additional aspects of Nav1 evolution, including changes to other residues lining the pore may confer additional ion selectivity/permeability properties[44].Voltage-gated sodium channels undergo conformational changes between three general states: closed, open, and inactivated (**Figure 1.1C**). The voltage dependence of channel opening is conferred by charged residues in the S4 segments of each repeat (**Figure 1**). Depolarization of the plasma membrane results in minor translocation of the S4 segments, allowing ions to flow through the channel[45–47]. Fast inactivation is mediated by the domain III/IV linker via mechanisms that have yet to be fully resolved (**Figure 1.1C**)[48,49]. Thus, voltage-gated sodium channels are responsible for the initiation and propagation of action potentials by allowing the selective passage of sodium ions across the plasma membrane in response to depolarization[50]. In the central nervous system, voltage-gated sodium channel paralogs Nav1.1, 1.2, 1.3 and 1.6 exhibit differential expression levels in excitatory and inhibitory cells[51]. Therefore, it is critical to dissect the unique functions of voltage-gated sodium channel isoforms in order to understand their differential influence on the central nervous system in health and disease[29–31].

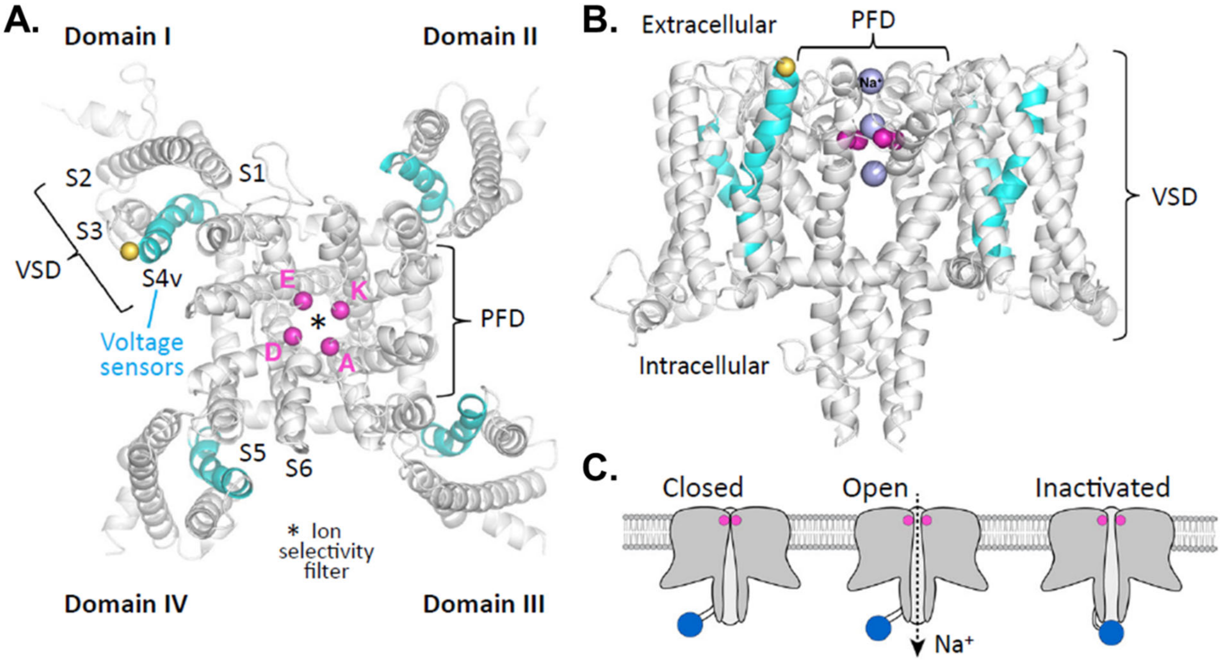

Figure 1.1 Overview of voltage-gated sodium channels. Adapted from Figure 1B-D of Sanders et al. (2018)[35]. (A) Homology model of generic voltage-gated sodium channel transmembrane region, top view. Functional and structural domains are labeled. Transmembrane segments of Domain I are labeled S1-S6. S1-S4v represents the voltage-sensing domain (VSD). The voltage-sensing segments are labeled S4v and colored cyan. S5-S6 of Domain I-IV comprise the pore-forming domain (PFD). The ion selectivity filter is represented by an asterisk. The Cα carbons from each residue (DEKA) of the filter are represented by pink spheres. The Cα carbon of the residue that differs between the developmentally regulated splice isoforms of Na$_V$1.2 is represented as a yellow sphere. (B) Homology model of generic voltage-gated sodium channel transmembrane region, side view. Sodium passing through the ion selectivity filter is represented by purple spheres. (C) Functional states of voltage-gated sodium channels. Channels are closed at resting membrane potential. Depolarization of the plasma membrane results in channel opening, allowing sodium ion flux. Fast inactivation occurs via a hinged lid mechanism (blue) that results in occlusion of the ion conducting pore

SCN2A and Na$_V$1.2

SCN2A encodes the Na$_V$1.2 voltage-gated sodium channel alpha subunit that is expressed predominantly in the central nervous system. While Na$_V$1.2 is expressed in most neuronal cell types to some degree, it is highly expressed in the glutamatergic pyramidal cells of the neocortex[52,53]. Other regions with notable expression of Na$_V$1.2 include the hippocampus, brainstem, and cerebellum[54–57]. At the subcellular level, the distribution of Nav1.2 within different axonal compartments changes across development[58]. Animal models have been used extensively to study changes in the distribution of Nav1.2 across development. Comparatively, the first postnatal week of life in mice corresponds to late gestation through the first year of life in humans[59]. During this period of early development in mice, Nav1.2 is the major sodium channel isoform expressed in the axon and axon initial segment of pre-myelinated axons[55,60]. Thus, Nav1.2 is responsible for the initiation and propagation of action potentials in these cells[61]. Later in development, Nav1.2 is replaced by Nav1.6 at the distal axon initial segment and at the nodes of Ranvier in myelinated axons[62]. Nav1.6 has a lower voltage threshold of activation compared to Nav1.2 and becomes the main driver of action potentials in myelinated axons[63,64]. At this stage, Nav1.2 is still highly expressed in unmyelinated axons. In myelinated axons, Nav1.2 becomes restricted to the proximal axon initial segment and is thought to be involved in the backpropagation of action potentials from the axon initial segment to the soma[52,55,60]. Nav1.2 is also expressed in the somatodendritic compartment throughout life and has been shown to influence dendritic excitability and synaptic plasticity in the neocortex[58,65,66]. Thus, Nav1.2 is an important contributor to neuronal communication during development and in local circuits in the mature brain. Furthermore, developmentally-regulated splice events affect Nav1.2 channel conductance and influence action potential shape[67–69]. The combination of developmentally regulated changes in splicing and subcellular distribution may influence the effect of disease-causing genetic variants at different points in brain development, underscoring the need for studying variants in their native environment.

SCN2A-related NDD

Large-scale genetic studies provide evidence suggesting *SCN2A* is a major genetic driver of NDD. Furthermore, *SCN2A* variants show wide phenotypic heterogeneity and have been reported in a number of early-onset epilepsy syndromes, as well as ASD, ID, and schizophrenia[3,5,7,9,10,70–80]. Efforts to better understand the clinical spectrum of *SCN2A*-related NDD have generally involved functional annotation of pathogenic variants to establish genotype-phenotype correlations. This process has established a general framework wherein variants with particular effects on channel function have been associated with three major categories of *SCN2A*-related NDD[35,70–72,74,81–83]. A visual schematic of this framework originally published in a review by Sanders et al. (2018) [35] is shown in **Figure 1.2**. *SCN2A* variants are increasingly associated with developmental and epileptic encephalopathies (DEE), an umbrella term including severe epilepsy syndromes such as Otahara syndrome, epilepsy of infancy with migrating focal seizures, infantile spasms (West syndrome), and Lennox-Gastaut syndrome[77,78,84–91]. The term DEE was proposed as part of the 2017 Classification of the Epilepsies to denote an epilepsy associated with developmental impairment that may be due to both the underlying etiology (developmental encephalopathy) and superimposed epileptic activity (epileptic encephalopathy)[92]. Furthermore, an epilepsy syndrome refers to a cluster of electroclinical features such as seizure type, EEG patterns (synchronized synaptic activity recorded in populations of neurons), and imaging features that tend to occur together, but does not necessarily have a single etiological diagnosis[92]. DEE phenotypes account for 60-70% of *SCN2A*-related disorders[35,71,72]. *SCN2A* variants associated with DEE are largely (77%) missense, occur *de novo*, and most often result in gain of function (GoF) effects[70–72,84]. Missense *SCN2A* variants are also associated with self-limited familial neonatal-infantile epilepsy (SeLFNIE, previously benign-familial neonatal infantile seizures) which is characterized by early-onset seizures that spontaneously remit over time[93–95]. It is theorized that this spontaneous remittance is due to the developmental shift in expression of Nav1.2 relative to Nav1.6[71,72,96]. The SeLFNIE phenotype accounts for approximately 20% of *SCN2A*-related disorders[72]. Functional characterization of SeLFNIE-associated variants in heterologous expression systems revealed mainly GoF effects that are less severe than those associated with DEE[68,72,84,96,97]. In addition, the majority (>80%) of *SCN2A* variants associated with SeLFNIE are inherited rather than *de novo*[72]. *SCN2A* variants associated with ID and/or ASD are mainly (75%) protein-truncating variants (PTVs) characterized by loss-of-function (LoF) effects[70–73]. ID/ASD phenotypes account for approximately 16% of *SCN2A* disorders and sometimes present with comorbid seizures starting later in life[71,72].

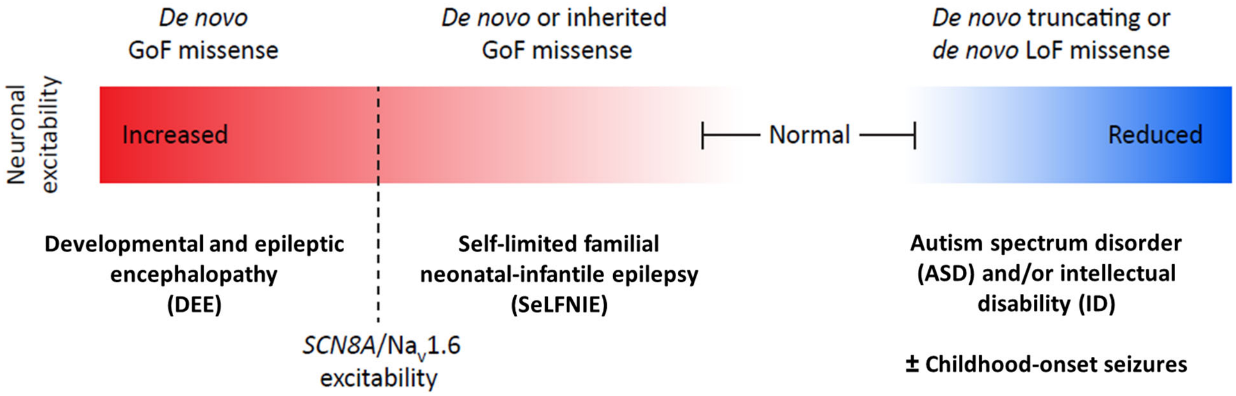

Figure 1.2 Current model of *SCN2A* pathophysiology. Adapted from Figure 2 of Sanders et al. (2018). Severe gain-of-function (GoF) missense variants, resulting in increased neuronal excitability, lead to developmental and epileptic encephalopathies (DEE) with neonatal or early infantile onset. Less dramatic GoF missense variants lead to self-limited familial neonatal-infantile epilepsy (SeLFNIE), which resolves before 2-year-of-age without apparent long-term neurological sequelae. The threshold that distinguishes DEE and SeLFNIE variants may be related to the developmental shift in expression of Na$_V$1.2 relative to Na$_V$1.6, such that Na$_V$1.6 may be able to functionally compensate for less severe GoF variants. In contrast, loss-of-function (LoF) missense variants and protein-truncating variants (PTVs) that reduce neuronal excitability lead to intellectual disability (ID) and/or autism spectrum disorder (ASD). Some of these cases have co-morbid seizures starting later in life, typically months after onset of encephalopathy associated with GoF variants.

As more variants are characterized, it is becoming increasingly evident that this GoF/LoF framework does not fully capture the phenotypic complexity of *SCN2A*-related NDD. For example, a number of missense variants resulting in LoF have been associated with DEE and SeLFNIE phenotypes[71,98–100]. Functional annotation of *SCN2A* variants often reveals effects that span multiple aspects of channel function (e.g. voltage dependence, kinetics). These effects can be considered GoF or LoF with regard to individual channels, but the effect of a given variant of the intrinsic properties of neurons represents a complex summation of channel-level effects[35,71,82]. For example, the DEE-associated variants *SCN2A*-p.L1342P and p.S1336Y were both shown to have mixed effects on channel function, but were considered to be overall GoF with regard to neuronal excitability[82,83,101]. More recently, Crawford and colleagues attempted to further refine the genotype-phenotype relationships of *SCN2A*-related disorders by mapping existing data onto a standardized phenotyping framework for quantitative analysis[102]. In line with previous studies, this study found that individuals with PTVs were significantly less likely to have seizures compared to those with missense variants[70,74,81,102]. In addition, this study expanded upon prior work associating variants located in the S5-S6 pore loop with ASD phenotypes[70,102]. Most notably, this study used logistic principal component analysis to predict variant function and found that variants associated with DEE phenotypes did not reliably map onto a binary GoF/LoF classification[102]. Continued efforts to establish genotype-phenotype correlations for *SCN2A*-related disorders can be supported by properly validated animal models of recurrent and mixed-effect variants.

Modeling SCN2A-related NDD

Current mouse models of *Scn2a* recapitulate some aspects of *SCN2A*-related NDD. In 2001, Kearney and colleagues developed the $Scn2a^{Q54}$ model that has a gain-of-function mutation

(GAL879-881QQQ) in *Scn2a*. Development of this model occurred prior to the discovery of voltage-gated sodium channel variants in humans. Thus, the GAL879-881QQQ mutation is not patient-specific. *Scn2a*^{Q54} mice are hemizygous for mutant Nav1.2 and develop a juvenile-onset epilepsy phenotype characterized by focal motor seizures[103]. Over time the phenotype evolves to include secondary generalization, status epilepticus, and premature death[103]. In addition, the mice display repetitive/perseverative behaviors suggestive of autistic-like traits[103]. Isolated and slice recordings of hippocampal neurons from *Scn2a*^{Q54} mice show elevated persistent current and increased excitability, respectively[103,104]. Initial characterization of the *Scn2a*^{Q54} model marked the first reported association between a voltage-gated sodium channel and epilepsy or ASD. Furthermore, these results provided supportive evidence for human genetic studies[29,96,105–109]. Despite recapitulating some aspects of *SCN2A*-related disorders, the *Scn2a*^{Q54} model has technical limitations stemming from the mutagenesis techniques available at the time of model development. First, the model was developed by random insertion of a transgene that drives overexpression of mutant Nav1.2 in a nonnative locus and may be subject to positional effects. Second, the transgene itself consists of rat cDNA under the control of a neuron specific enolase (*Eno2*) promoter and an SV40 late polyadenylation signal. Thus, the transgene may not faithfully recapitulate endogenous expression. This highlights the need for new models of *SCN2A* variants with higher construct validity.

Scn2a knockout models also recapitulate some aspects of *SCN2A*-related NDD associated with LoF PTVs[58,110–117]. Given that homozygous knockout of *Scn2a* is associated with perinatal lethality, most studies are conducted using various *Scn2a* haploinsufficient models[54,58,110–116]. However, conditional knockout methods have been used to produce viable homozygous mice with more severe *Scn2a* deficiency[58,117]. Behavioral abnormalities reported in *Scn2a* deficient mice vary across research groups and may reflect differences in methodological practices as well as inherent variability of behavioral data[118,119]. Anxiety-related behavior and social behavior are frequently assessed in mouse models of ASD-related genes, including *Scn2a*[120]. Reductions in anxiety-like behavior have been reported in *Scn2a* deficient mice, although the opposite effect has also been reported[58,111,112,117]. Similarly inconsistent effects on social behavior have also been reported in *Scn2a* deficient mice[112,114–116]. Although ASD is typically associated with social behavior deficits[121], hyper-social behaviors such as inappropriate social approach and enhanced direct social interaction have been reported in various ASD-associated genetic mouse models[122,123]. This highlights the heterogeneity of ASD-associated phenotypes as well as the complexity of modeling human social behavior in animals. As previously mentioned, ID/ASD phenotypes associated with LoF PTVs in *SCN2A* sometimes present with co morbid seizures[71,72]. In humans, clinical observations of seizures have been used in conjunction with EEG patterns (recorded either during or in between seizures) to classify different types of epilepsy and define epilepsy syndromes[92]. While it has been noted that some EEG patterns in rodents show some similarities with normal and pathological EEG patterns seen in humans, the primary utility of rodent EEG is to identify biomarkers that distinguish treatment and control groups[124]. EEG recording has been used to evaluate neurological phenotypes in *Scn2a* deficient mice with conflicting results. Ogiwara and colleagues described spike-and-wave discharges characteristic of absence epilepsy in *Scn2a* haploinsufficient mice, while other groups reported no observable seizures in the same model[54,110,113]. It has been shown that progressively severe deficiency of Nav1.2 expression is associated with paradoxical and cell-autonomous hyperexcitability in excitatory neurons from the neocortex and striatum, suggesting a possible mechanism for seizures due to *SCN2A* LoF[125,126].

Comparatively few models of *SCN2A* GoF variants that recapitulate DEE phenotypes have been developed, an example of which is the *Scn2a^{A263V}* model. This variant was shown to result in an increased persistent sodium current, and is associated with neonatal epilepsy in humans[127]. Frequent spontaneous seizures were reported in mice homozygous for the p.A263V variant, whereas heterozygotes exhibited infrequent non-convulsive seizures[128,129]. Generating more animal models of missense *SCN2A* variants associated with DEE phenotypes as well as mixed effect variants will help us further refine genotype-phenotype correlations for *SCN2A*-related NDD.

SCN2A K1422E

In many cases, variants have consistent biophysical effects on channel function that permit easy categorization within the GoF or LoF paradigm. Variants that show more complex effects on channel function can be harder to place and are often associated with seizure onset around 1-year-of-age[35,71,99]. One biophysically remarkable example is the *de novo* missense variant *SCN2A*-p.K1422E, which was identified in a child with infant-onset developmental delay and infantile spasms that were refractory to treatment, as well as features of ASD[85]. This variant disrupts one of the four critical residues within the ion-conducting pore domain of Nav1.2 that confer selectivity for sodium over all other cations, converting the positively charged amino acid lysine (K) to the negatively charged amino acid glutamic acid (E)[130–132]. As previously mentioned, voltage-gated sodium channels evolved from a primordial channel with mixed selectivity, where the selectivity filter has a glutamic acid (E) substituted for lysine (K) in the 3rd transmembrane domain[41,42]. Thus, the p.K1422E variant can be seen as an evolutionary reversion at the selectivity filter[32,33]. Previous biophysical characterizations of rat Nav1.2 channels expressed in *Xenopus* oocytes suggest that p.K1422E alters channel ion selectivity, increasing permeation for potassium and calcium[130,132]. In addition, calcium has been shown to antagonize K1422E channels, reducing overall current density[130]. Furthermore, the p.K1422E variant prevents binding of the neuronal sodium channel antagonists tetrodotoxin (TTX) and saxitoxin that bind to the outer vestibule[133,134]. TTX blocks wild-type neuronal Nav1.1, Nav1.2, Nav1.3 and Nav1.6 channels. Therefore, isolated recordings of TTX-insensitive mutant channels can be achieved by applying TTX. The critical importance of the Lysine 1422 residue in determining sodium selectivity and sensitivity to sodium channel blockers provides strong support for continued study of the p.K1422E variant.

Given the unique properties of K1422E in heterologous expression systems, it is difficult to understand how it might affect the intrinsic properties of neurons. This is further complicated by inherent differences in intracellular processes when comparing neuronal cells and heterologous expression systems[135]. This underscores the need to study the p.K1422E variant in disease relevant tissue. In **Chapter 2**, I describe our assessment of K1422E channel function in heterologous expression systems to see if we could recapitulate previous findings[130,132]. We used that data to develop a channel model and compartmental neuronal model to provide testable predictions for how K1422E affects neuronal function. To further investigate this, we generated a novel mouse model carrying the *SCN2A*-p.K1422E variant and examined effects on cellular excitability using electrophysiological and imaging techniques. We also characterized neurological/neurobehavioral phenotypes in *Scn2a*^{K1422E} mice.

Sex Differences in NDD

Historically, biological sex has been neglected as a variable in both human and non-human research, with a strong bias towards male subjects[136]. Despite this bias, it is widely accepted that sex differences are present at multiple levels of organization in the central nervous system[137–139]. This suggests that biological sex is an important variable to consider in the context of neuropathology. As an aside, the terms “sex” and “gender” are often incorrectly conflated. “Sex” refers to any number of interrelated biological features such as chromosomes, gene expression profiles, hormones, and anatomy that distinguish the classifications of male, female, and sometimes intersex[140,141]. “Gender” refers to a psychosocial construct of roles, behaviors, activities, attributes, opportunities, and relationships that individuals perceive of themselves in relation to a spectrum of identities including, but not limited to, man and/or woman[141,142]. I will reference sex as a biological variable in the following chapters, distinguishing male and female mice as determined by external genitalia. Mice either do not have gender, or if they do, we certainly lack the ability to ask them about it. As such, gender is not relevant for the purposes of this dissertation. Sex differences have been reported in a number of NDD including ID, ASD, schizophrenia, and epilepsy[143–148]. Notably, an increased male prevalence has been reported for several NDD including ID, ASD, and epilepsy[144,149,150]. Studies looking at patterns of risk variation between males and females suggest that clinical manifestations of at least some NDD require a higher mutational burden for females, leading to the idea of a “female protective effect”[144]. One hypothesis proposed to explain this effect in relation to ASD is that variation at one or more genetic loci confers sex-specific protection to females[151–153]. Another hypothesis implicates fetal androgen exposure in sex-differential risk for ASD[153,154].

Epilepsy represents a diverse group of conditions for which differences between males and females can vary across different types of seizures[143,147–149]. The neurobiological basis for sex differences in seizure susceptibility is likewise varied and the subject of ongoing research[147,148]. One area that has received significant attention involves the reciprocal relationship between sex hormones and seizure susceptibility. It has been widely documented that women with epilepsy often show a cyclical pattern of altered seizure susceptibility during specific phases of the menstrual cycle[155–157]. This pattern of "catamenial epilepsy" affects between 25-75% of women with epilepsy[158]. The association between seizure susceptibility and the menstrual cycle can be attributed to fluctuations in hormones and corresponding changes in neurosteroid levels[147,148,156,159]. Studies using rodent models of epilepsy reveal complex, sometimes contradictory effects of ovarian hormones and neurosteroids on seizure susceptibility. In general, estradiol is proconvulsant and progesterone (along with its neurosteroid derivative allopregnalone) is anticonvulsive[147,148,160]. To date, the effects of the estrous (menstrual) cycle on seizure susceptibility have not been evaluated in the context of an epilepsy-associated genetic variant. In **Chapter 3**, I describe our investigation of estrous cycle effects on susceptibility to induced seizures in the *Scn2a*^{K1422E} mouse model.

Modifiers of SCN2A-related NDD

As was previously highlighted, a growing body of literature has been dedicated to cataloging disease-causing *SCN2A* variants based on their association with distinct biophysical defects in channel function. Missense variants resulting in a GoF have been associated with DEE phenotypes while missense variants and nonsense variants resulting in a LoF have been associated with ASD/ID[70,71,74,81,82]. Although the biophysical properties of mutant channels likely contribute to phenotype expressivity, recurrent and inherited variants in *SCN2A* show wide phenotypic heterogeneity, even among individuals with the same variant[70,71,91] This suggests that factors beyond the primary pathogenic mechanism of a given variant may contribute to the presence of/variation in a particular phenotype. These factors might include genetic, epigenetic, and environmental modifiers. It is becoming increasingly evident that background genome variation (i.e., modifiers) can affect the phenotypic properties of presumed "monogenic" disorders, but this can be difficult to study in the context of rare diseases with small patient populations [21,22,24–28].

Inbred populations (strains) of research animals are a double-edged sword when it comes to modeling disease. On the one hand, the isogenic* nature of these animals makes them attractive for use as biological replicates in transgenic experiments[161]. One the other hand, the genetic background of particular strains may interact with the variant gene of interest in a way that compromises analysis of disease-related phenotypes[162]. However, these properties can be leveraged to study the effect of genetic modifiers in animal models of disease. Accordingly, different genetic backgrounds across rodent strains have been shown to influence disease phenotypes, including seizure susceptibility[103,162–170]. For example, it has been shown previously that the DBA/2J mouse strain exhibits a high rate of spontaneous spike-wave discharges associated with behavioral arrest and increased susceptibility to induced seizures[171–175]. Furthermore, it has been demonstrated that genetic background dramatically influences the epilepsy phenotype described in the *Scn2a*^{Q54} mouse model. *Scn2a*^{Q54} mice on a C57BL/6J background (B6) displayed adult-onset seizures and a mild survival deficit (>75% survival at 6 months) compared to WT mice on the same background. Meanwhile, *Scn2a*^{Q54} mice on a mixed [B6 × SJL] F1 background

---

* Inbred strains are homozygous at ≥ 98.6% of loci, making them *virtually* isogenic (citation in text)

displayed juvenile-onset seizures and a more severe survival deficit (25% survival at 6 months) compared to mutant animals on a pure B6 background[103,163]. Since then, a number of epilepsy modifier loci and genes (*Hlf, Kcnv2, Cacna1g, Kcnq2, Scn1a*) responsible for the B6/SJL strain-dependent effect have been identified using both classical genetic mapping strategies and a candidate gene approach[163,169,176–183]. Importantly, these studies only reflect the B6/SJL strain effect in a single model of *SCN2A*-related NDD. The effects of background strain on NDD-related phenotypes in other *Scn2a* mouse models remain largely unexplored. In **Chapter 4**, I describe our evaluation of strain-dependent effects on neurobehavioral and seizure phenotypes in the *Scn2a*^{K1422E} mouse model.

1.2 Overview of Data Chapters

The entirety of data presented in **Chapter 2** is published:

Dennis M Echevarria-Cooper, Nicole A Hawkins, Sunita N Misra, Alexandra M Huffman, Tyler Thaxton, Christopher H Thompson, Roy Ben-Shalom, Andrew D Nelson, Anna M Lipkin, Alfred L George Jr, Kevin J Bender, Jennifer A Kearney, Cellular and behavioral effects of altered Na$_V$1.2 sodium channel ion permeability in *Scn2aK1422E* mice, *Human Molecular Genetics*, Volume 31, Issue 17, 1 September 2022, Pages 2964–2988, https://doi.org/10.1093/hmg/ddac087

Supplemental figures from the published version have been integrated into the text of **Chapter 2** with no modifications. The methods section has been expanded to include more procedural details. Drs. Jennifer A. Kearney, Kevin J. Bender, Alfred L. George, and I conceived the experiments. Functional characterization experiments in heterologous expression systems were performed by Dr. Christopher H. Thompson. *In silico* modeling was performed by Dr. Roy Ben-Shalom. The genetically engineered mice were generated with the assistance of Lynn Doglio in the Northwestern University Transgenic and Targeted Mutagenesis Laboratory. Mouse transcript and protein expression experiments were performed by Dr. Nicole Hawkins and myself, with assistance from Levi Barse. Mouse neuron culture and electrophysiology experiments were performed by Dr. Christopher H. Thompson with assistance from Dr. Sam Kang. *Ex-vivo* electrophysiology and two-photon imaging experiments were performed by Drs. Andrew D. Nelson and Anna M. Lipkin. Video-EEG monitoring experiments were performed by Drs. Nicole A. Hawkins, Sunita N. Misra, and myself. Flurothyl seizure induction experiments were performed by myself. Neurobehavioral assays were performed by Alexandra M Huffman, Tyler Thaxton, and myself. This work was supported by the National Institutes of Health (grant numbers: R21 OD025330 to J.A.K., U54 NS108874 to A.L.G. and J.A.K., R01 MH125978 to K.J.B., F32 MH125536 to A.D.N., KL2TR001424 to S.N.M.); Simons Foundation Autism Research Initiative (grant numbers: 629287 and 513133 to K.J.B.); National Science Foundation (grant number: 1650113 to A.M.L.); Epilepsy Foundation of Greater Chicago (Rovner Fellowship to S.N.M.); FamileSCN2A (Action Potential Grant to S.N.M.).

The data presented in **Chapter 3** are unpublished with the exception of the initial flurothyl seizure induction experiments comparing female cohorts which are published in Echevarria-Cooper et al. (2022; full citation on previous page)[184]. Data from the aforementioned experiments are also shown in **Figure 2.9F** as they appear in Echevarria-Cooper et al. (2022)[184]. For use in **Chapter 3**, the aforementioned data are replotted in **Figure 3.1** and then collapsed across cohorts and presented as “WT Naïve” and “E/+ Naïve” in **Figure 3.3B**. Dr. Jennifer A. Kearney and I conceived the experiments. All experiments and analyses were performed by myself with assistance from Dr. Kearney.

The data presented in **Chapter 4** are also unpublished. Drs. Jennifer A. Kearney, Nicole A. Hawkins, and I conceived the experiments. Video-EEG monitoring experiments were performed by Dr. Hawkins and analyzed by Drs. Kearney, Hawkins, and myself. Kainic acid status epilepticus induction experiments were performed by Dr. Hawkins and analyzed by myself, with assistance from Sahithi Gangavarapu. Neurobehavioral assays were performed by myself with assistance from Dr. Erin M. Baker.

Chapter 2. Characterization of *Scn2a*^{K1422E} Mice

2.1 Introduction

Pathogenic variants in *SCN2A* are a major risk factor for neurodevelopmental disorders (NDDs), with more than 250 heterozygous genetic variants having been described in association with a wide range of clinical phenotypes[35]. *SCN2A* encodes the voltage-gated sodium channel Nav1.2 and is highly expressed in neurons of the central nervous system. Severe gain-of-function (GoF) missense variants, resulting in increased neuronal excitability, lead to developmental and epileptic encephalopathies (DEE) with neonatal or early infantile onset, including Ohtahara syndrome and epilepsy of infancy with migrating focal seizures[71,72,83,84]. Less dramatic GoF missense variants lead to self-limited seizures, which resolve before 2-year-of-age without apparent long-term neurological sequelae[70,97]. In contrast, loss-of-function (LoF) missense variants and protein-truncating variants (PTVs) that reduce neuronal excitability early in development and synaptic plasticity later in development lead to intellectual disability (ID) and/or autism spectrum disorder (ASD)[58,70,73]. Some of these cases have co-morbid seizures starting later in life, typically months after onset of encephalopathy associated with GoF variants[71].

In many cases, variants have consistent biophysical effects on channel function that permit easy categorization within the GoF or LoF paradigm. Variants that show more complex effects on channel function can be harder to place and are often associated with seizure onset around 1-year-of-age[35,71,99]. One biophysically remarkable example is the *de novo* missense variant *SCN2A*-p.K1422E, which disrupts one of the four critical residues within the ion-conducting pore domain of Nav1.2 that confer selectivity for sodium over all other cations[130–132]. This variant alters the overall charge of the ion selectivity filter, converting the positively charged amino acid, lysine (K), to the negatively charged amino acid glutamic acid (E). The resultant channel, which has been studied in heterologous expression systems, loses sodium selectively, instead becoming a mixed, non-selective cation channel with apparent permeability for sodium, potassium and calcium with diminished overall conductance[130,132]. Furthermore, the K1422E variant prevents binding of the neuronal sodium channel antagonists tetrodotoxin (TTX) and saxitoxin that bind to the outer vestibule[133,134].

To our knowledge, K1422E is the only variant within the existing *SCN2A* patient population that affects ion selectivity, contrasting markedly with other variants that commonly alter voltage dependence, kinetics or trafficking[35,70,72,83,185]. Given the unique properties of K1422E in heterologous expression systems, it is difficult to understand how it might affect the intrinsic properties of neurons. To investigate this, we generated a mouse model carrying the *SCN2A*-p.K1422E variant and examined effects on cellular excitability using electrophysiological and imaging techniques. Excitatory neurons in neocortex exhibited features indicative of functional K1422E-containing Nav1.2 channels, including lower current density with a TTX-insensitive component and aberrant calcium influx occurring during the Nav-mediated rising phase of the action potential (AP). Analysis of behaving animals revealed a mix of phenotypes, including infrequent spontaneous seizures, reduced anxiety-like behavior and alterations in olfactory-guided social behavior. Thus, these data suggest that altering Nav1.2 ion selectivity results in cellular and behavioral phenotypes that partially mirror those observed in other models of *Scn2a* dysfunction, in addition to features that are entirely unique to K1422E.

2.1 Materials and Methods

Heterologous cell electrophysiology

Heterologous expression of human Nav1.2 WT (Addgene #162279)[186] or K1422E was performed in HEK293T cells. Cells were grown in 5% CO_2 at 37°C in Dulbecco modified Eagle's medium (DMEM) supplemented with 10% fetal bovine serum, 2 mM L-glutamine, 50 units/mL penicillin and 50 µg/mL streptomycin. Cells were transiently co-transfected with Nav1.2 and the accessory β_1 and β_2 subunits (2 µg total plasmid DNA was transfected with a cDNA ratio of 10:1:1 for Nav1.2:β_1:β_2 subunits) using Qiagen SuperFect reagent (Qiagen, Valencia, CA, USA). Human β_1 and β_2 cDNAs were cloned into plasmids encoding the CD8 receptor (CD8-IRES-hβ_1) or enhanced green fluorescent protein (EGFP) (EFGP-IRES-hβ_2), respectively, as transfection markers[187,188]. Cells were passaged 24 hr after transfection and incubated 24 hr before their use in electrophysiology experiments. Transfected cells were dissociated by brief exposure to trypsin/EDTA, resuspended in supplemented DMEM medium, and allowed to recover for ∼30 min at 37°C in 5% CO_2. Only cells positive for CD8 antigen and GFP fluorescence were used for electrophysiological studies.

Dissociated cells were placed into a recording chamber on the stage of an inverted microscope with epifluorescence capability. After allowing the cells to settle for 10 min, sodium currents were recorded in the whole-cell patch configuration of the patch-clamp technique[187–190]. Whole-cell voltage-clamp recordings were made at room temperature using an Axopatch 200B amplifier (Molecular Devices, LLC, Sunnyvale, CA, USA). Patch pipettes were pulled from borosilicate glass capillaries (Harvard Apparatus Ltd, Edenbridge, Kent, UK) with a multistage P-1000 Flaming-Brown micropipette puller (Sutter Instruments Co., San Rafael, CA, USA) and fire-polished using a microforge (Narashige MF-830; Tokyo, JP) to a resistance of 1.5–2.5 MΩ. The pipette solution consisted of (in mM): 10 NaF, 105 CsF, 20 CsCl, 2 EGTA, and 10 HEPES with pH adjusted to 7.35 with CsOH and osmolality adjusted to 300 mOsmol/kg with sucrose. The recording solution was continuously perfused with bath solution containing (in mM): 145 NaCl, 4 KCl, 1.8 $CaCl_2$, 1 $MgCl_2$, 10 glucose and 10 HEPES with pH adjusted to 7.35 with NaOH and osmolality 310 mOsmol/kg. For sodium-free recordings, the bath solution contained (in mM): 120 NMDG, 4 KCl, 10 $CaCl_2$, 2 $MgCl_2$, 10 glucose and 10 HEPES with pH adjusted to 7.35 with HCl and osmolality 310 mOsmol/kg.

Mice

Scn2a^{K1422E} mice on the C57BL/6J strain were generated using CRISPR/Cas9 to introduce the modification of K1422 by homology directed repair. A single nucleotide change was introduced in codon 1422 (AAA > GAA), resulting in a glutamate residue being encoded at the modified position. A single guide RNA (TCCTTTAAATGTGGCCTGTA) with low predicted off-target effects, and a 151 bp repair oligo:

(5′- CCTTGTTTCCACTTTTACTCTGATAATCTATTTCCTAAACTATAAAAAGAGAAGAAGTATATATGTTGATTGTTTTACAGGCCACATTT**G**AAGGATGGATGGATATCATGTATGCAGCTGTTGACTCAAGAAATGTAAGTTTACTTTGG)

were delivered to C57BL/6J embryos at the two-cell stage using electroporation by the Northwestern University Transgenic and Targeted Mutagenesis Laboratory. Potential founders were screened by PCR of genomic DNA using primers outside the repair oligo homology region (**Table 2.1**), and the region of interest was cloned into pCR-TOPO (ThermoFisher) and Sanger sequenced. The mosaic K1422E founder was backcrossed to C57BL/6J mice (Jackson Labs,

#000664, Bar Harbor, ME) to generate N1 offspring. N1 offspring were genotyped by Sanger sequencing to confirm transmission of the K1422E editing event and were screened for off-target events by Sanger sequencing of all potential sites with <3 mismatches. N1 males with the confirmed on-target event and without predicted off-target events were bred with C57BL/6J females to establish the line *Scn2a*^{em1Kea} (MGI:6390565), which is maintained as an isogenic strain on C57BL/6J by continual backcrossing of *Scn2a*$^{K1422E/+}$ heterozygous mice (abbreviated as *Scn2a*$^{E/+}$) with inbred C57BL/6J mice. Heterozygous *Scn2a*$^{E/+}$ and *Scn2a*$^{+/+}$ (wild-type, abbreviated as WT) mice for experiments were obtained from this breeding at generations >N3.

Table 2.1 List of primers and probes

Assay	**Description**	**Sequence**
Founder Screening PCR	2A Primer 1	5’-AGCTCATCTATCACCTTGAACC
	2A Primer 2	5’-AAAGAAACGAATCCCCAACAAAA
Genotyping *Scn2a*^{K1422E}	Primer 1	5’-GTGGTAGAAATATCCAGAATGCTTCCC
	Primer 2	5’-CTTGAGTCAACAGCTGCATACATGA
	Probe 1 (WT allele)	5’-VIC-CATCCATCCTTTAAATGT-NFQ
	Probe 2 (mutant allele)	5’-FAM-TCCATCCTTCAAATGT-NFQ

Abbreviations: FAM, FAM reporter dye; VIC, VIC reporter dye; NFQ, non-fluorescent quencher

Mice were maintained in a specific pathogen free (SPF) barrier facility with a 14 h light/10 h dark cycle and access to food and water ad libitum. Both female and male mice were used for all experiments. All animal care and experimental procedures were approved by the Northwestern University and UC San Francisco Animal Care and Use Committees in accordance with the National Institutes of Health Guide for the Care and Use of Laboratory Animals. Principles outlined in the ARRIVE (Animal Research: Reporting of *in vivo* Experiments) guideline were considered when planning experiments[191].

Genotyping

DNA was isolated from tail biopsies using the Gentra Puregene Mouse Tail Kit according to the manufacturer's instructions (Qiagen, Valenica, CA, USA). Genomic DNA was digested with BamHI-HF (New England Biolabs, Ipswich, MA, USA) at 37°C for 1 h, diluted 1:1 with nuclease-free water and used as template for digital droplet PCR (ddPCR) using ddPCR Supermix for Probes (No dUTP) (Bio-Rad, Hercules, CA, USA) and a custom TaqMan SNP Genotyping Assay (Life Technologies, Carlsbad, CA, USA) (**Table 2.1**). Reactions were partitioned into droplets using a QX200 droplet generator (Bio-Rad). PCR conditions were 95°C for 10 min, then 44 cycles of 95°C for 30 s and 60°C for 1 min (ramp rate of 2°C/s) and a final inactivation step of 98°C for 5 min. Following amplification, droplets were analyzed on a QX200 droplet reader with Quantasoft v1.6.6 software (Bio-Rad).

Transcript analysis

Whole brain total RNA was extracted from WT and *Scn2a*$^{E/+}$ mice at 4 weeks of age using TRIzol reagent according to the manufacturer's instructions (Invitrogen, Carlsbad, CA, USA). First-strand cDNA was synthesized from 2 μg of total RNA using oligo(dT) primer and Superscript IV reverse transcriptase (RT) according to the manufacturer's instructions (Life Technologies). First-strand cDNA samples were diluted 1:3 and 5 μL was used as template. Quantitative ddPCR was performed using ddPCR Supermix for Probes (No dUTP) (Bio-Rad) and TaqMan Gene Expression Assays (Life Technologies) for mouse *Scn2a* (FAM-MGB-Mm01270359_m1) and *Tbp* (VIC-MGB-Mm00446971_m1) as a normalization standard. Reactions were partitioned into droplets using a QX200 droplet generator (Bio-Rad). Thermocycling conditions and analysis were performed as described for genotyping. Both assays lacked detectable signal in no-RT controls.

Relative transcript levels were expressed as a ratio of *Scn2a* concentration to *Tbp* concentration (normalized to the mean ratio for WT mice), with 7–8 biological replicates per genotype, balanced by sex. Statistical comparison between groups was made using Student's *t*-test (GraphPad Prism, San Diego, CA, USA).

Immunoblotting

Whole brain membrane proteins were isolated from WT and *Scn2a*$^{E/+}$ mice at 4 weeks of age. Membrane fractions (50 µg/lane) were separated on a 7.5% SDS-PAGE gel and transferred to nitrocellulose. Blots were probed with anti-Nav1.2 pAb (Alomone Labs, Jerusalem, ISR; #ASC-002, RRID: AB_2040005; 1:200 dilution) or anti-Nav1.1 (Alomone Labs, Jerusalem, ISR; #ASC-001, RRID: AB_2040003; 1:200 dilution) or anti-Nav1.6 (Alomone Labs, Jerusalem, ISR; #ASC-009, RRID: AB_2040202; 1:500 dilution) and anti-mortalin/GRP75 mAb (Antibodies Inc, Davis, CA, USA; Neuromab N52A/42, RRID: 2120479; 1:1000 dilution), which served as a normalization standard. Alexa Fluor 790 goat anti-rabbit antibody (Jackson ImmunoResearch, West Grove, PA, USA; #111-655-144, RRID: AB_2338086; 1:10 000 dilution) and 680 goat anti-mouse antibody (Jackson ImmunoResearch; #115-625-146; RRID: AB_2338935; 1:10 000 dilution) were used to detect signal on an Odyssey imaging system (Li-COR, Lincoln, Nebraska USA). Relative protein levels were determined by densitometry with Image Studio (Li-COR) and expressed as a ratio of Nav1.x to GRP75 (normalized to the mean ratio for WT mice), with 7–8 biological replicates per genotype, balanced by sex. Statistical comparison between groups was made using Student's *t*-test (GraphPad Prism).

Cortical neuron culture and electrophysiology

Cortical neuron cultures were derived from P0 mice that were rapidly genotyped prior to euthanasia. Genomic DNA was PCR amplified with 2A primer 1 and 2A primer 2 (**Table 2.1**), and product was digested with HpyAV (New England Biolas, Ipswich, MA, USA) resulting in a 398 bp fragment for WT and 238 and 160 bp fragments for the K1422E mutant allele. Whole-cell voltage-clamp recordings of cortical pyramidal neurons were performed at DIV 15–17. Pyramidal neurons were identified morphologically as cells with large pyramidal shaped cells bodies. All recordings were performed at room temperature using an Axopatch 200B amplifier (Molecular Devices) in the absence and presence of 500 nM TTX and 500 nM TTX + 100 nM Guangxitoxin 1E (GxTx-1E). Patch pipettes were pulled from borosilicate glass capillaries (Harvard Apparatus Ltd, Edenbridge, Kent, UK) with a multistage P-97 Flaming-Brown micropipette puller (Sutter Instruments) and fire-polished using a microforge (Narashige MF-830) to a pipette resistance of 1.5–2.5 MΩ. The pipette solution consisted of (in mM) 5 NaF, 105 CsF, 20 CsCl, 2 EGTA and 10 HEPES with pH adjusted to 7.35 with CsOH and osmolarity adjusted to 280 mOsmol/kg with sucrose. The recording chamber was continuously perfused with a bath solution containing in (mM) 120 NaCl, 4 KCl, 10 HEPES, 1.8 $CaCl_2 \cdot 2H_2O$, 1 $MgCl_2 \cdot 6H_2O$ and 20 tetraethylammonium chloride with pH adjusted to 7.35 with HCl and osmolarity adjusted to 310 mOsmol/kg with sucrose.

Voltage-clamp pulse generation and data collection were done using Clampex 10.4 (Molecular Devices). Somatic currents were isolated using a pre-pulse to −45 mV, as previously described[192]. Whole-cell capacitance was determined by integrating capacitive transients generated by a voltage step from −120 to −110 mV filtered at 100 kHz low pass Bessel filtering. Series resistance was compensated with prediction >70% and correction > 80% to assure that the command potential was reached within microseconds with a voltage error <3 mV. Leak currents were subtracted by using an online P/4 procedure. All whole-cell currents were filtered at 5 kHz low pass Bessel filtering and digitized at 50 kHz. Whole-cell sodium conductance ($G_{\max}$) for each cell was calculated according to $G_{\max} = I/(V - V_{Na+})$, where I is the peak current amplitude, V is the applied voltage and V_{Na+} is the measured equilibrium potential for the cell.

Acutely dissociated neuron electrophysiology

Hippocampal pyramidal neurons from P21-P24 WT or *Scn2a*$^{E/+}$ were isolated as previously described[169,193]. Mice were deeply anesthetized with isoflurane then rapidly decapitated. The brain was promptly removed under aseptic conditions and placed in ice-cold dissecting solution containing (in mM) 2.5 KCl, 110 NaCl, 7.5 $MgCl_2 \cdot 6H_2O$, 10 HEPES, 25 dextrose, 75 sucrose, 1 pyruvic acid, and 0.6 ascorbic acid with pH adjusted to 7.35 with NaOH. Coronal slices (400 µm) were made through the hippocampi using a Leica VT 1200 vibratome (Leica Microsystems Inc., Buffalo Grove, IL, USA) in ice-cold dissecting solution bubbled with 95% O_2/5% CO_2. Slices were incubated for one hour at 30°C in artificial CSF (ACSF, in mM: 12 4 NaCl, 4.4 KCl, 2.4 $CaCl_2 \cdot 2H_2O$, 1.3 $MgSO_4$, 1 NaH_2PO_4, 26 $NaHCO_3$, 10 glucose, and 10 HEPES with pH adjusted to 7.35 with NaOH) bubbled with 95% O_2/5% CO_2. Hippocampi were dissected from the slices with micro-forceps and digested for 15 min at room temperature with proteinase (2 mg/ml) from *Aspergillus melleus* Type XXIII in dissociation solution (in mM: 82 Na_2SO_4, 30 K_2SO_4, 5 $MgCl_2 \cdot 6H_2O$, 10 HEPES, and 10 dextrose with pH adjusted to 7.35 with NaOH), then washed multiple times with dissociation solution containing 1 mg/ml bovine serum albumin and allowed to recover for ≥10 min in the same solution before mechanical dissociation by gentle trituration with sequentially fire-polished Pasteur pipettes of decreasing diameter. The cell suspension was allowed to settle on coverslips for 15 min before experiments. Unless otherwise stated, all chemicals were purchased from Sigma-Aldrich (St. Louis, MO, USA).

Whole-cell voltage-clamp recordings were made at room temperature using an Axopatch 200B amplifier (Molecular Devices) in the absence and presence of 500 nM TTX. Patch pipettes were pulled from borosilicate glass capillaries (Harvard Apparatus Ltd, Edenbridge, Kent, UK) with a multistage P-97 Flaming-Brown micropipette puller (Sutter Instruments) and fire-polished using a microforge (Narashige MF-830) to a pipette resistance of 1.5–2.5 MΩ. The pipette solution consisted of (in mM) 5 NaF, 105 CsF, 20 CsCl, 2 EGTA and 10 HEPES with pH adjusted to 7.35 with CsOH and osmolarity adjusted to 280 mOsmol/kg with sucrose. The recording chamber was continuously perfused with a bath solution containing in (mM) 20 NaCl, 100 N-methyl-D-glucamine, 10 HEPES, 1.8 $CaCl_2 \cdot 2H_2O$, 2 $MgCl_2 \cdot 6H_2O$ and 20 tetraethylammonium chloride with pH adjusted to 7.35 with HCl and osmolarity adjusted to 310 mOsmol/kg with sucrose.

Voltage-clamp pulse generation and data collection were done using Clampex 10.4 (Molecular Devices). Whole-cell capacitance was determined by integrating capacitive transients generated by a voltage step from −120 to −110 mV filtered at 100 kHz low pass Bessel filtering. Series resistance was compensated with prediction >70% and correction >90% to assure that the command potential was reached within microseconds with a voltage error <3 mV. Leak currents were subtracted by using an online P/4 procedure. All whole-cell currents were filtered at 5 kHz low pass Bessel filtering and digitized at 50 kHz.

Modeling

Channel biophysical properties and models were generated in the NEURON environment (v7.5) as previously described[58,70,194]. The K1422E variant was modeled by first introducing potassium permeability to an established Nav1.2 channel model at a ratio of 1:0.7 (Na:K), and assuming that Cs^+ and K^+ permeability were comparable, as determined previously[130]. Subsequently, calcium permeability was increased to levels that best captured the reversal potential observed in HEK293T cells (**Figure 2.1C)**, with reversals for Na^+, Cs^+ ($\approx K^+$) and Ca^{2+} determined from the Goldman-Hodgkin-Katz equation. This was best described by relative permeabilities for Na^+, K^+ and Ca^{2+} of 1:0.7:0.8. This K1422E channel model was incorporated into previously established models of cortical pyramidal cells with baseline distributions of Nav1.2 and Nav1.6 set as previously described[58,70], based on a pyramidal cell model by Hallerman et al. (2012)[194]. The variant channel was incorporated at a 50:50 ratio with a WT Nav1.2 allele. In order to better match empirical observations of reduced current density due to calcium antagonism, an additional K1422E variant model was developed by reducing the number of K1422E channels relative to WT. APs were generated with a 2.1 nA current applied at the soma.

Ex vivo whole-cell electrophysiology

Experiments were performed in accordance with guidelines set by the University of California Animal Care and Use Committee, and 250-µm-thick coronal slices containing medial prefrontal cortex were obtained from *Scn2a*$^{E/+}$ and WT littermate mice of both sexes aged P35–45. Cutting solution contained, in mM: 87 NaCl, 25 $NaHCO_3$, 25 glucose, 75 sucrose, 2.5 KCl, 1.25 NaH_2PO_4, 0.5 $CaCl_2$ and 7 $MgCl_2$, bubbled with 5% CO_2/95% O_2. After cutting, slices were incubated in the same solution for 30 min at 33°C, then at room temperature until recording. Recording solution contained, in mM: 125 NaCl, 2.5 KCl, 2 $CaCl_2$, 1 $MgCl_2$, 25 $NaHCO_3$, 1.25 NaH_2PO_4 and 25 glucose, bubbled with 5% CO_2/95% O_2, with an osmolarity of ~310 mOsmol.

For whole-cell recording of layer 5b pyramidal cells, slices were visualized using Dodt contrast optics on a purpose built 2-photon microscope. Patch electrodes were pulled from Schott 8250 glass (3–4 MΩ tip resistance) and filled with a solution containing, in mM: 113 K-gluconate, 9 HEPES, 4.5 $MgCl_2$, 14 Tris2-phosphocreatine, 4 Na2-ATP, 0.3 Tris-GTP, 600 μM OGB-5 N, 0.1 μM EGTA and 20 μM AlexaFluor 594; ~290 mOsmol, pH 7.2–7.25. Electrophysiological data were acquired using a Multiclamp 700B amplifier (Molecular Devices) and custom routines in IgorPro (Wavemetrics, Portland, OR, USA). Data were acquired at 50 kHz and Bessel filtered at 20 kHz. Recordings were made using quartz electrode holders to minimize electrode drift within the slice, enabling stable imaging of diffraction-limited spots in close proximity to the recording electrode (Sutter Instruments). Recordings were excluded if series resistance exceeded 14 MΩ or if the series resistance changed by greater than 20% over the course of the experiment. Fast pipette capacitance, as measured in cell-attached voltage clamp mode (typically 10–12 pF), was compensated 50% in current-clamp recordings, and data were corrected for a 12 mV junction potential.

Two-Photon Imaging

Imaging was performed as described previously[195]. A Coherent Ultra II laser was tuned to 810 nm and epifluorescence and transfluorescence were collected through a 60×, 1.0 NA objective and a 1.4 NA oil immersion condenser, respectively (Olympus). Dichroic mirrors and band-pass filters (575 DCXR, ET525/70m-2p, ET620/60m-2p, Chroma) were used to split fluorescence into red and green channels. HA10770-40 photomultiplier tubes (PMTs, Hamamatsu) selected for >50% quantum efficiency and low dark counts captured green fluorescence (Oregon Green BAPTA 5 N). Red fluorescence (AlexaFluor 594) was captured using R9110 PMTs (Hamamatsu).

Fluorescence data were collected in a pointscan configuration, where the laser was parked at single diffraction-limited spots along the AIS membrane. Data were collected over a series of 5 points spanning 2 µm (e.g. separated by 0.5 µm), in regions either 3–5 µm from the axon hillock (proximal AIS) or 28–30 µm from the axon hillock (distal AIS). Each point was imaged at 20 kHz for 25 ms preceding and 100 ms following an AP. Individual points were imaged in a sequence of 2, 4, 1, 3, 5, with 2 being the point most proximal to the soma. Individual APs within the set of 5 points were separated by 250 ms. Data were averaged over 40 repetitions for each site and subsequently averaged over all five spots for a total averaging of 200 sampled APs. Data were then smoothed using a 40-point binomial filter in IgorPro for analysis. Calcium transients were normalized to saturating conditions ($\Delta G/G_{\mathrm{sat}}$), which was calculated as $\Delta(G/R)/(G/R)_{\mathrm{max}}\times 100$, where G/R_{max} is the maximal fluorescence in saturating calcium (2 mM). Transient onset was defined as the time at which signals exceeded root-mean-squared noise levels of the 20 ms period preceding AP onset.

Video-EEG monitoring

Male and female WT and *Scn2a*$^{E/+}$ mice were implanted with prefabricated 3-channel EEG headmounts (Pinnacle Technology, Lawrence, KS, USA) at 4–6 weeks of age. Briefly, mice were anesthetized with ketamine/xylazine and place in a stereotaxic frame. Headmounts with four stainless steel screws that serve as cortical surface electrodes were affixed to the skull with glass ionomer cement. Anterior screw electrodes were 0.5–1 mm anterior to bregma and 1 mm lateral from the midline. Posterior screws were 4.5–5 mm posterior to bregma and 1 mm lateral from the midline. EEG1 represents recordings from right posterior to left posterior (interelectrode distance ≈ 2 mm). EEG2 represents recordings from right anterior to left posterior (interelectrode distance ≈ 5 mm). The left anterior screw served as the ground connection. Following at least 48 h of recovery, tethered EEG and video data were continuously collected from freely moving mice with Sirenia acquisition software (Pinnacle Technology) using a sampling rate of 400 Hz as previously described[196]. At least 96 h of EEG data were acquired from each subject [WT range: 96–672 h/mouse ($n = 17$ mice; 5–11 weeks of age); *Scn2a*$^{E/+}$ range: 168–672 h/mouse ($n = 15$ mice; 5–13 weeks of age)]. Raw data was notch filtered with a 1 Hz window around 60 and 120 Hz prior to analysis. Video-EEG records were manually reviewed with Sirenia software, MATLAB (MathWorks, Natick, MA, USA) and EEGLAB (Swartz Center for Computational Neuroscience, CA, USA) by two independent reviewers blinded to genotype. Spontaneous seizures were defined as isolated events with an amplitude of ≥3 times baseline, duration of ≥10 s and that show evolution in power and amplitude. Epileptiform discharges were defined as isolated events with a spike and overriding fast activity, an amplitude of ≥3 times baseline, duration of 150–500 ms and with increased power in frequencies >20 Hz compared with baseline. Samples with high baseline artifact were excluded from analysis.

Flurothyl seizure induction

Susceptibility to seizures induced by the chemoconvulsant flurothyl (Bis(2,2,2-trifluoroethyl) ether, Sigma-Aldrich, St. Louis, MO, USA) was assessed in WT and *Scn2a*$^{E/+}$ mice at 6–9 weeks of age. Flurothyl was introduced into a clear, plexiglass chamber (2.2 L) by a syringe pump at a rate of 20 μL/min and allowed to volatilize. Latencies to first MJ, generalized tonic–clonic seizure (GTCS) with loss of posture, and time interval between these phases were recorded (*n* = 19–20 per genotype and sex). Groups were compared as indicated in **Table 2.2** (GraphPad Prism), with sexes considered separately.

Neurobehavioral assays

Male and female WT and *Scn2a*$^{E/+}$ mice were tested between 6 and 11 weeks of age. Male and female mice were tested separately with at least a 1 h delay between sessions. For all experiments, mice were acclimated in the behavior suite with white noise for 1 h prior to behavioral testing. At the end of each procedure, mice were placed into a clean cage with their original littermates. Behavioral testing was performed by experimenters blinded to genotype. For the initial cohort of mice, evaluation occurred over 6 weeks, with one assay performed each week: week 1—zero maze; week 2—light–dark exploration; week 3—open field; week 4—rotarod; week 5—three-chamber social interaction and week 6—olfactory habituation/dishabituation test. The remaining assays were performed on a new cohort of mice, with one assay performed each week: week 1—marble burying; week 2—Y-Maze (not reported) and week 3—buried food. For all measures, males and females were considered separately. Statistical comparisons between groups were made using Student's *t*-test or two-way repeated measures ANOVA with Sidak's post-hoc comparisons, unless otherwise indicated (**Table 2.2**).

Zero maze

Mice were evaluated for anxiety-related behavior in an elevated zero maze at 6 weeks of age. The maze consists of an annular platform (diameter 46 cm; elevation 50 cm) that is divided into equally sized quadrants, alternating between open and enclosed (wall height 17 cm). This configuration lacks the ambiguous center region associated with the elevated plus maze[197]. Individual mice were placed near an enclosed arm of the maze and allowed to freely explore for 5 min. Limelight software (Actimetrics, Wilmette, IL, USA) was used to video record each trial. Ethovison XT software (Noldus, Leesberg, VA, USA) was used to track the position of the mouse, and calculate distance traveled, mean velocity and time spent in closed or open arms ($n = 12$–14 per genotype and sex). Trials where mice fell off the maze were excluded from analysis.

Light-dark exploration

Mice were evaluated for anxiety-related behavior in a light–dark box at 7 weeks of age. The plexiglass box is divided into equally sized light (400 lx) and dark (0 lx) sections (20 × 40 cm) separated by a central partition plate with a small opening (3 × 5 cm) to allow transit between sections. Individual mice were placed in the center of the light section, facing away from the dark section, and allowed to freely explore for 10 min. Limelight software was used to video record each trial. Ethovison XT software was used to track the position of the mouse, and calculate time spent in light or dark sections ($n = 13$–15 per genotype and sex).

Open field

Mice were evaluated for baseline activity and anxiety-related behavior in an open field at 8 weeks of age. Individual mice were placed in the center of an open field arena (46 × 46 cm) and allowed to freely explore for 30 min. Limelight software was used to video record each trial. Ethovison XT software was used to track the position of the mouse, and calculate total distance traveled, mean velocity and time spent in the periphery (9 cm from wall) and center (28 × 28 cm) (*n* = 13–15 per genotype and sex).

Rotarod

Mice were evaluated for motor coordination and balance using an accelerating rotarod (Panlab, Harvard Apparatus, Barcelona, Spain) at 9 weeks of age. Up to 5 mice were placed on the rotating rod that accelerated from 4 to 40 RPM over 5 min. Mice were given three trials per day for 3 consecutive days with an inter-trial interval of 15 min. Latency to fall from the rotating rod was automatically recorded (*n* = 11–14 per genotype and sex).

Three-chamber social interaction

Mice were evaluated for sociability and preference for social novelty using a three-chamber social interaction test at 10 weeks of age. The three-chamber apparatus consists of a plexiglass box divided into equally sized chambers (21 × 42 cm) separated by transparent plates with small openings (3 × 5 cm) to allow transit between chambers. All chambers were subject to uniform illumination (170 lx). One wire cylinder-shaped cage was placed in the center of each side chamber and used to enclose a sex-matched, 8–12-week-old C57BL/6J stranger mouse during the testing phase of the assay. During an initial habituation phase, individual test mice were placed in the middle of the center chamber and allowed to freely explore for 10 min. During the first test phase (sociability), a stranger mouse was randomly placed in a wire cage in one of the side chambers and the test mouse was allowed to freely explore for 10 min. During the second testing phase (social novelty), the stranger mouse from the sociability phase remained in place and was then considered familiar. Then, a second stranger mouse was placed in the wire cage in the opposite side chamber and the test mouse was allowed to freely explore for 10 min. Limelight software was used to video record each trial. Ethovison XT software was used to track the position of the test mouse, and calculate time spent in each chamber and time spent sniffing stranger mice or empty wire cage ($n = 11$–14 per genotype and sex). Trials where mice spent >10% of trial time on top of the wire cages were excluded.

Olfactory habituation/dishabituation test

Olfactory impairment could interfere with social behaviors, therefore olfactory discrimination for social and non-social odor was evaluated in 11-week-old mice as previously described[198]. Dry applicators were used to present odor stimuli to test mice: non-social odors—distilled water, almond extract (McCormick, Hunt Valley, MD, USA; 1:100 dilution) and banana extract (McCormick; 1:100 dilution); social odors—unfamiliar social cage (same sex), unfamiliar social cage (opposite sex). During an initial habituation phase, individual mice were placed in a clean testing cage with a clean dry applicator and allowed to freely explore for 30 min. During the testing phase, odor stimuli were presented to test mice for three consecutive trials each (15 trials total) in the following order: (i) distilled water, (ii) almond extract, (iii) banana extract, (iv) same sex cage and (v) opposite sex cage. Each odor was presented for 2 min with an inter-trial interval of 1 min. Trials were video recorded and sniffing time was evaluated manually by an independent reviewer blinded to genotype ($n = 13$–14 per genotype and sex).

Marble burying task

Marble burying was evaluated in 6-week-old mice to assess phenotypes related to anxiety and obsessive-compulsive behavior. Individual mice were placed in a clean testing cage with 4 cm of bedding and acclimated for 15 min. Mice were then briefly removed from the cage while bedding was flattened and 20 marbles were evenly placed across the cage in a 5 × 4 matrix with a small open space at the front of the cage. A baseline image of the cage was taken prior to reintroduction of the mouse and reimaged after the 30 min trial. The two images were compared for the number of marbles buried, defined by at least 50% of the marble being submerged under the bedding (n = 13–14 per genotype and sex).

Buried food test

Mice were evaluated for olfactory-guided behavior using a buried food task at 8 weeks of age as previously described[198]. Teddy Grahams (Nabisco, Hanover, NJ, USA) have been established as a palatable food stimulus in this assay. In order to familiarize test mice with the stimulus odor, one cookie was placed in the home cage of all subjects for 3–4 consecutive days prior to testing. In order to drive olfactory-guided behavior, mice were transferred to a clean cage with their original littermates without access to food 15–18 h before testing. On the testing day, single cookies were buried in a random corner of clean cages with 3 cm of bedding. Individual mice were placed in a clean testing cage and latency to find the food stimulus was recorded (n = 13–14 per genotype and sex). Mice that failed to find the food stimulus after 15 min received a latency score of 900 s.

Statistical analysis

Table 2.2 summarizes statistical tests used for all comparisons along with computed values. D’Agostino and Pearson tests for normality were used to determine parametric versus non-parametric test selection. F test to compare variances was used to determine where to apply correction for unequal standard deviations.

Table 2.2 Statistical comparisons

Figure	Comparison	Test	Value	Post Hoc
2.1	Sodium Current Density at -10 mV (**E**)	Student's t-test	p=0.0033	n/a
	Sodium Current Reversal Potential (**D**)	Student's t-test	p=0.0109	n/a
	Calcium Current Density at -10 mV (**E**)	Student's t-test	p<0.0001	n/a
2.3	*Scn2a*^{K1422E} Expression (**D**)	Student's t-test	p=0.5162	n/a
	Na$_V$1.2-K1422E Expression (**E**)	Student's t-test	p=0.5327	n/a
2.4	Na$_V$1.1 Expression (**A**)	Student's t-test	p=0.9624	n/a
	Na$_V$1.6 Expression (**E**)	Student's t-test	p=0.2565	n/a
2.5	Total Sodium Current Reversal Potential (**D**)	Student's t-test	p=0.0012	n/a
	TTX-Sensitive Current Reversal Potential (**D**)	Student's t-test	p<0.0001	n/a
	TTX-Insensitive Current Reversal Potential (**D**)	Student's t-test	p=0.7027	n/a
2.6	Total Sodium Current Reversal Potential (**D**)	Student's t-test	p=0.0364	n/a
	TTX-Sensitive Current Reversal Potential (**D**)	Student's t-test	p=0.0006	n/a
	TTX-Insensitive Current Reversal Potential (**D**)	Student's t-test	p=0.6964	n/a
2.7	Peak Action Potential Speed (**D**)	Student's t-test	p=0.01	n/a
2.8	Calcium Transient Amplitude (**E**)	Student's t-test	p=0.014	n/a
	Calcium Transient Onset (**D**)	Student's t-test	p<0.001	n/a
2.9	Male GTCS Flurothyl (**E**)	Welch's t-test	p<0.0001	n/a
	Female GTCS Flurothyl (**E**)	Kolmogorov-Smirnov test	p=0.0282	n/a
	Male MJ Flurothyl (**F**)	Student's t-test	p=0.8813	n/a
	Male Time for Seizure Progression (**F**)	Mann-Whitney test	p<0.0001	n/a
	Female MJ Flurothyl (**F**)	Mann-Whitney test	p=0.7126	n/a
	Female Time for Seizure Progression (**F**)	Kolmogorov-Smirnov test	p=0.0350	n/a
2.10	Male Zero Maze (**A**)	Student's t-test	p=0.0023	n/a
	Female Zero Maze (**A**)	Welch's t-test	p=0.0297	n/a
	Male Light-Dark Exploration (**B**)	Student's t-test	p=0.0367	n/a
	Female Light-Dark Exploration (**B**)	Mann-Whitney test	p=0.0367	n/a
	Male Open Field (**E**)	Mann-Whitney test	p=0.0556	n/a
	Female Open Field (**E**)	Mann-Whitney test	p=0.0167	n/a
	Male Marble Burying (**D**)	Mann-Whitney test	p=0.0019	n/a
	Female Marble Burying (**D**)	Mann-Whitney test	p<0.0001	n/a
	Male Rotarod (**E**)	Two-way repeated measures ANOVA	F(1.511,34.76)=8.450, p=0.0022 (Main Effect: Test Day) F(1,23)=10.18, p=0.0041 (Main effect: Genotype)	Sidak's
	Female Rotarod (**E**)	Two-way repeated measures ANOVA	F(1.594,36.65)=6.646, p=0.0059 (Main effect: Test Day) F(1,23)=1.249, p=0.2752 (Main Effect: Genotype)	Sidak's
2.11	Male Three-chamber – Sociability (**A**)	Two-way repeated measures ANOVA	F(1,24)=9.198, p=0.0057 (Target x Genotype) F(1,24)=57.28, p<0.0001 (Main effect: Target)	Sidak's
	Female Three-chamber – Sociability (**A**)	Two-way repeated measures ANOVA	F(1,22)=35.17, p<0.0001 (Main effect: Target)	Sidak's
	Male Three-chamber – Social Novelty (**B**)	Two-way repeated measures ANOVA	F(1,26)=19.02, p=0.0002 (Main Effect: Target) F(1,26)=11.85, p=0.0020 (Main Effect: Genotype)	Sidak's
	Female Three-chamber – Social Novelty (**B**)	Two-way repeated measures ANOVA	F(1,22)=9.145, p=0.0062 (Main Effect: Target) F(1,22)=6.081, p=0.0219 (Main Effect: Genotype)	Sidak's
2.12	Male Olfactory Habituation/Dishabituation	Multiple t-tests	p=0.0005 (Same Sex 1) p=0.0307 (Same Sex 2)	Holm-Sidak
	Female Olfactory Habituation/Dishabituation	Multiple t-tests	p=0.0045 (Same Sex 1)	Holm-Sidak

2.3 Results

K1422E alters channel ion permeability in heterologous expression systems

Previous biophysical characterizations of rat Na$_V$1.2 channels expressed in *Xenopus* oocytes suggested that K1422E alters channel ion selectivity, increasing permeation for potassium and calcium[130,132]. Thus, before assessing K1422E function in mice, we first assessed channel function in HEK293T cells to see if we could recapitulate these effects by expressing human Na$_V$1.2 and the accessory β_1 and β_2 subunits. Current density was significantly lower in cells expressing K1422E compared with wild-type (WT) channels (Current density at −10 mV: WT: -427.6 ± 95.7 pA/pF, $n = 7$, K1422E: -72.0 ± 18.7 pA/pF, $n = 7$, $P = 0.0033$) (**Figure 2.1B & C**). Furthermore, the reversal potential was more hyperpolarized (WT: 66.4 ± 1.1 mV, $n = 7$, K1422E: 34.4 ± 1.2 mV, $n = 7$, $P < 0.0001$; **Figure 2.1D**), suggestive of enhanced potassium permeability. To test whether K1422E channels were also permeable to calcium, recordings were made in sodium-free solutions with a higher calcium concentration (10 mM). Consistent with previous studies of bacterial and vertebrate Na$_V$1 channels[131,199], the WT channel showed no inward calcium-mediated current under these conditions (WT: 4.3 ± 0.5 pA/pF, $n = 7$). By contrast, K1422E channels supported appreciable inward current (WT: -44.4 ± 16.2 pA/pF, $n = 7$, $P = 0.0109$), indicating that the variant promoted calcium permeability (**Figure 2.1B & E**).

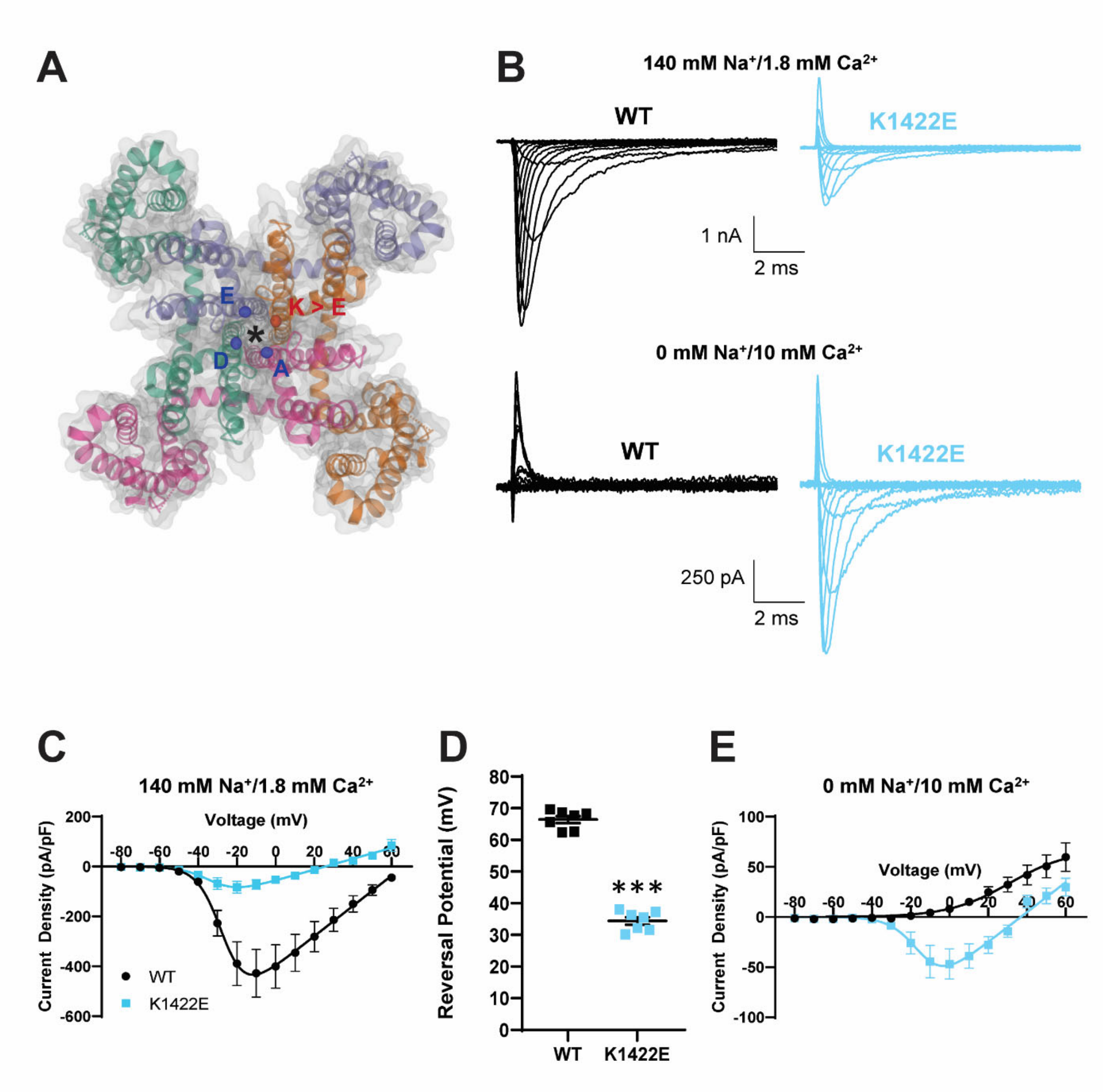

Figure 2.1 Heterologous expression of K1422E in HEK293T cells reveals altered ion selectivity. (**A**) Homology model of voltage-gated sodium channel alpha subunit (PDB 6MWA Na_VAb, residues1-239). Four internally homologous domains coalesce with four-fold symmetry around an ion conducting pore denoted by an asterisk. The Cα carbons from each residue (DEKA) of the highly conserved ion selectivity filter are represented by colored ellipses. The red ellipse denotes the Cα carbon from the K1422 residue that is substituted for glutamate (E) in the *Scn2a*^{K1422E} model. (**B**) Representative whole-cell sodium currents (top) and calcium currents (bottom) from WT (left) and K1422E (right) expressing cells. (**C**) Summary current–voltage relationship of whole-cell sodium current showing reduced sodium current density of K1422E at −10 mV ($P = 0.0033$). (**D**) Sodium reversal potential of WT and K1422E expressing cells ($P < 0.0001$). (**E**) Summary current–voltage relationship of whole cells calcium current showing increased calcium flux at −10 mV for K1422E ($P = 0.0109$). All data are plotted as mean ± SEM of $n = 7$ cells.

Given the unique properties of K1422E in heterologous expression systems as demonstrated in previous work and recapitulated here, it is difficult to understand how it might affect the intrinsic properties of neurons[130,132]. This is further complicated by inherent differences in intracellular processes when comparing neuronal cells and heterologous expression systems[135]. Thus, we developed a channel model and compartmental neuronal model to provide testable predictions for how K1422E affects neuronal function (**Figure 2.2)**. The K1422E variant was modeled first by introducing potassium permeability to an established Nav1.2 channel model at a ratio of 1:0.7 (Na:K), and assuming that Cs^+ and K^+ permeability were comparable, as determined previously[130]. Subsequently, calcium permeability was increased to levels that best captured the reversal potential observed in HEK293T cells, with reversals for Na^+, Cs^+ ($\approx K^+$) and Ca^{2+} determined from the Goldman-Hodgkin-Katz equation (**Figure 2.1C**). This was best described by relative permeabilities for Na^+, K^+ and Ca^{2+} of 1:0.7:0.8. Resultant current density relative to WT was reduced modestly in the model, but less markedly as observed in experiments (**Figure 2.2A & B**)[130]. This is because calcium has been shown to antagonize K1422E channels, reducing overall current density[130]. We therefore developed an additional channel model with reduced current density to match empirical observations, which was mimicked by reducing the number of K1422E channels relative to WT. This K1422E channel model was incorporated into previously established models of cortical pyramidal cells[70] at a 50:50 ratio with a WT Nav1.2 allele, and at reduced relative density to mimic increased calcium antagonism. APs generated by somatic current injection had features consistent with partial LoF conditions, with reductions in peak AP speed that approached, but did not match those observed in *Scn2a*$^{+/-}$ model neurons (**Figure 2.2C & D**; 6.4, 16.2 and 26.8% for reduction in AP speed for K1422E without calcium antagonism, with calcium antagonism, and *Scn2a*$^{+/-}$ conditions, respectively).

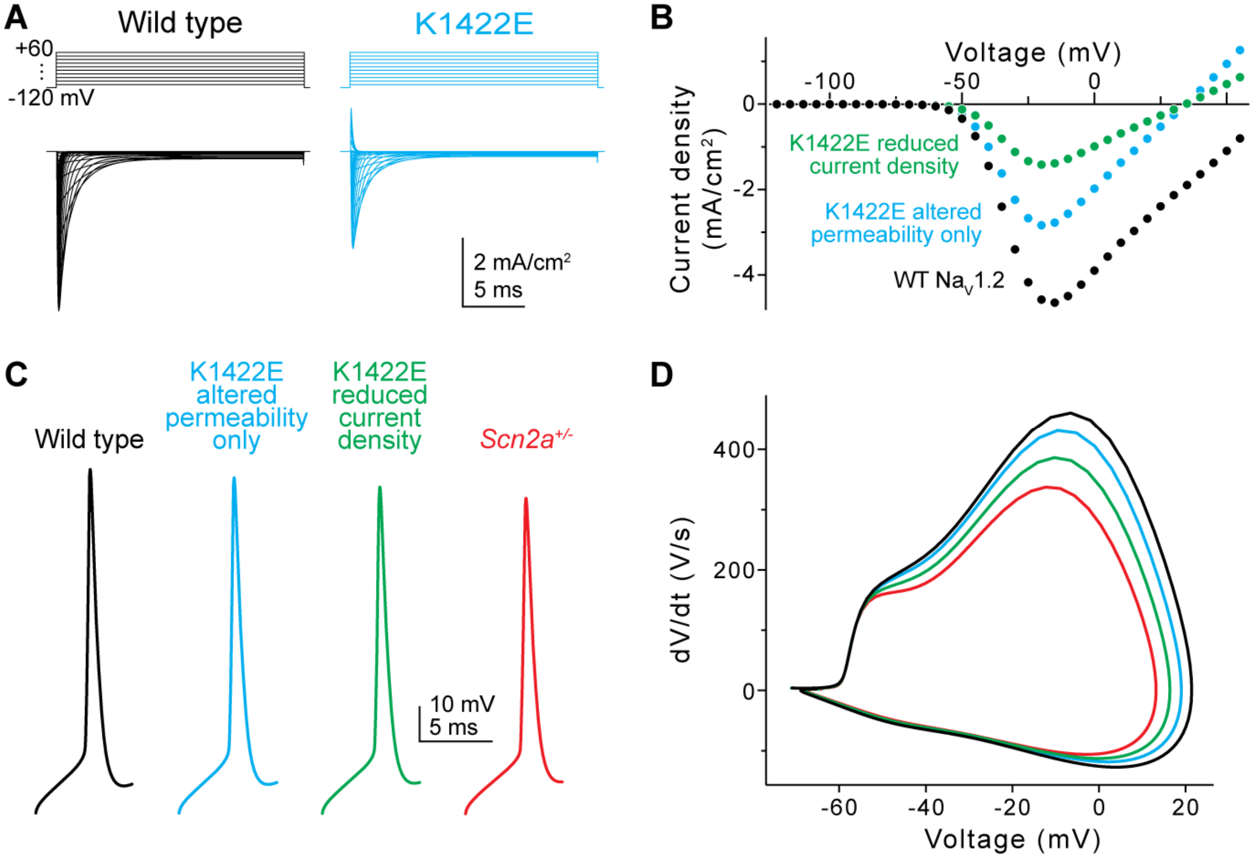

Figure 2.2 ***In silico*** **simulations of K1422E in neocortical pyramidal cells.** (**A**) Current evoked from simulated WT (black) and K1422E (cyan) channels in response to voltage steps from −120 to +60 mV (10 mV increments). (**B**) Current–voltage relationship for WT and K1422E channels. With altered permeability for K and Ca, K1422E current were reduced ~50% compared with WT, with a reversal at +33 mV (cyan). Reductions in current density to mimic calcium antagonism were required to match empirical results (green, compared with **Figure 2.1C**). (**C**) APs measured via a somatic electrode site in a model of a neocortical layer 5b pyramidal cell (identical to Spratt *et al.*[9]). +/K1422E conditions were modeled with or without reduced current density (cyan, green) and compared with WT (+/+) and haploinsufficient conditions (+/−, red). (**D**) Phase-plane plots of APs in (C).

Generation and initial characterization of Scn2a^{K1422E} mice

We developed an *in vivo* model of the NDD-associated *SCN2A*-p.K1422E pathogenic variant by using clustered regularly interspaced short palindromic repeats (CRISPR)/CRISPR-associated protein 9 (Cas9) genome editing to introduce the K1422E single nucleotide variant into mouse *Scn2a* via homology directed repair (**Figure 2.3A**). *Scn2a*$^{K1422E/+}$ heterozygous mutants (abbreviated as *Scn2a*$^{E/+}$) were born at the expected Mendelian ratios and there was no difference in body weight compared with WT littermates when measured at 4 weeks (WT: 13.5 ± 0.36 g, $n = 13$, *Scn2a*$^{E/+}$: 13.6 ± 0.49 g, $n = 14$, $P = 0.8349$, Student's *t*-test). We used droplet digital reverse transcription-polymerase chain reaction (RT-ddPCR) and immunoblotting to evaluate whole brain expression of *Scn2a* transcript and Nav1.2 protein, respectively, and observed no difference in expression between *Scn2a*$^{E/+}$ and WT mice (**Figure 2.3B-D**). Furthermore, we did not observe any difference in expression of Nav1.6 and Nav1.1 channels (**Figure 2.4**). Similar to constitutive knockout of *Scn2a*, mice homozygous for K1422E (*Scn2a*$^{E/E}$) exhibit 100% mortality by postnatal day 1 (P1)[54]. Because *SCN2A*-associated NDD is associated with heterozygous variants, our experiments focused on comparing *Scn2a*$^{E/+}$ mice to WT littermate controls.

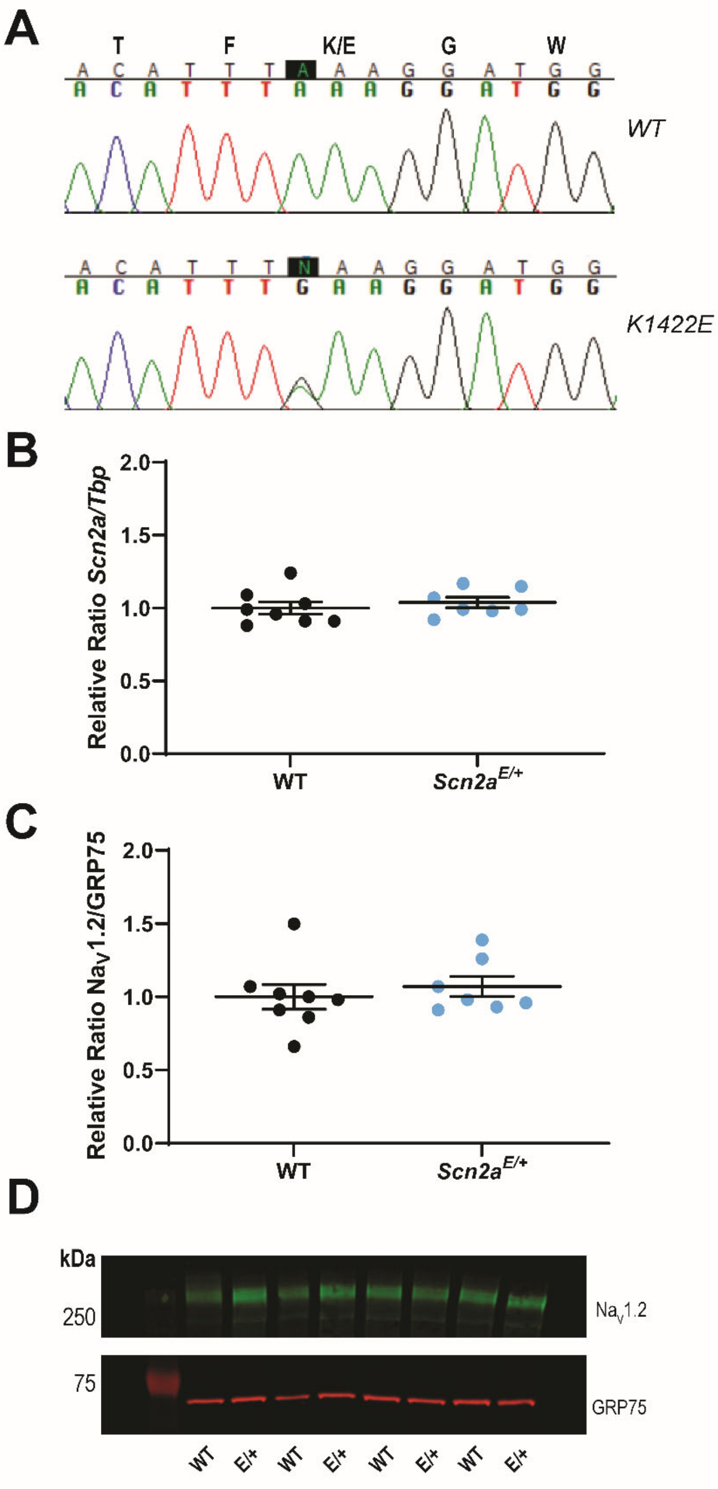

Figure 2.3 Generation and molecular characterization of *Scn2a*^{K1422E} mice. (**A**) Sequencing chromatograms of *Scn2a* genomic PCR products with the first nucleotide of the K1422E codon highlighted in black. Top chromatogram from a WT littermate control mouse shows homozygosity for the WT nucleotide at the K1422E codon. Bottom chromatogram from a heterozygous *Scn2a*$^{E/+}$ mouse shows heterozygosity for the single nucleotide change introduced by CRISPR/Cas9 genome editing and homology directed repair. (**B**) Relative expression of whole brain *Scn2a* transcript in WT and *Scn2a*$^{E/+}$ mice assayed by RT-ddPCR. Relative transcript levels are expressed as a ratio of *Scn2a* concentration to *Tbp* concentration (normalized to WT average). There was no difference in transcript expression between genotypes ($P = 0.5162$; $n = 7–8$ mice per genotype). (**C**) Relative expression of whole brain Na$_V$1.2 protein in WT and *Scn2a*$^{E/+}$ mice assayed by immunoblotting. Quantification is expressed as a ratio of Na$_V$1.2 immunofluorescence relative to GRP75/Mortalin (normalized to WT average). There was no difference in protein expression between genotypes ($P = 0.5327$; $n = 7–8$ mice per genotype). For both (B and C), circles represent samples from individual mice, horizontal lines represent mean and error bars represent SEM. (**D**) Representative immunoblot. Bands corresponding to Na$_V$1.2 (MW: 260 kDa) are visualized in green (Alexa Fluor 790), while bands corresponding to GRP75 (MW: 75 kDa) are visualized in red (Alexa Fluor 680).
]]>

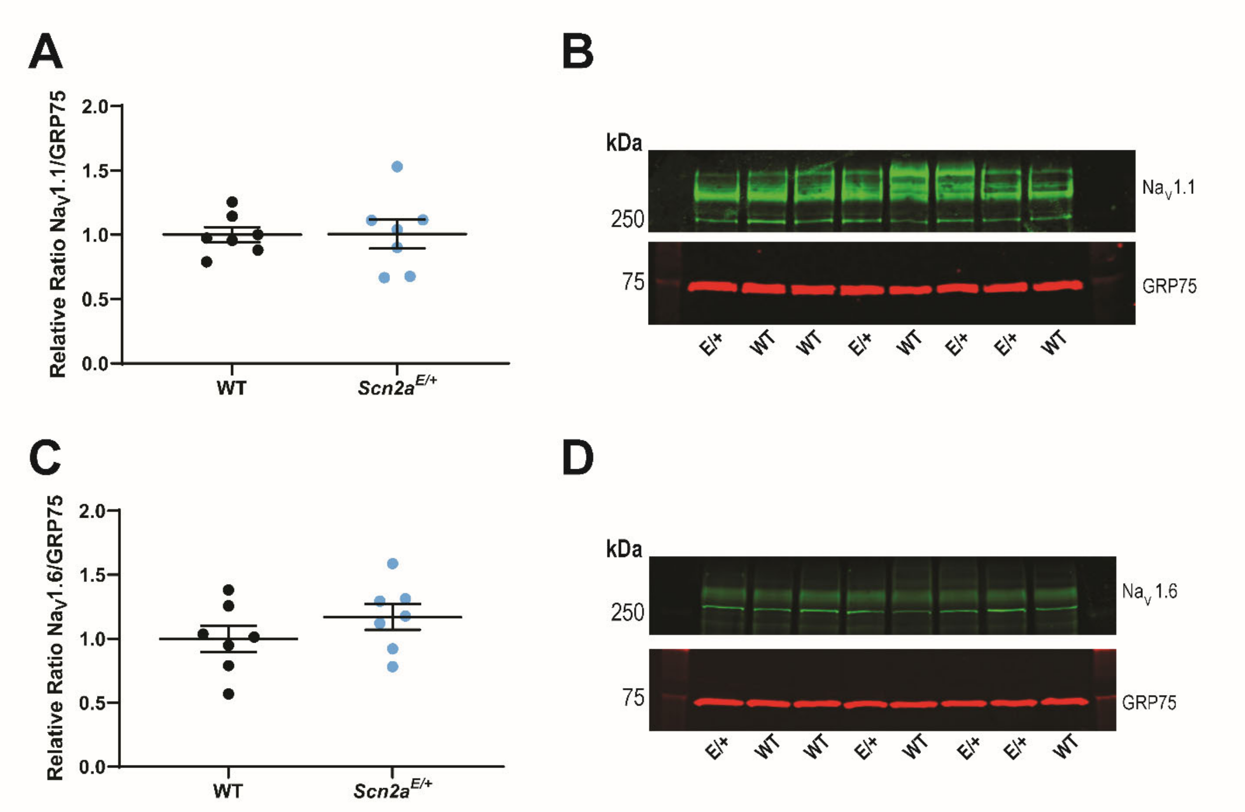

Figure 2.4. Expression of voltage gated-sodium channel paralogs in *Scn2a*$^{E/+}$ mice. (**A**) Relative expression of whole brain Na$_V$1.1 protein in WT and *Scn2a*$^{E/+}$ mice assayed by immunoblotting. Quantification is expressed as a ratio of Na$_V$1.1 immunofluorescence relative to GRP75/Mortalin (normalized to WT average). There was no difference in protein expression between genotypes ($p=0.9624$, Student's t-test; $n=7$ mice per genotype). (**B**) Representative immunoblot. Bands corresponding to Na$_V$1.1 (MW: 260 kDa) are visualized in green (Alexa Fluor 790) while bands corresponding to GRP75 (MW: 75 kDa) are visualized in red (Alexa Fluor 680). (**C**) Relative expression of whole brain Na$_V$1.6 protein in WT and *Scn2a*$^{E/+}$ mice assayed by immunoblotting. Quantification is expressed as a ratio of Na$_V$1.6 immunofluorescence relative to GRP75/Mortalin (normalized to WT average). There was no difference in protein expression between genotypes ($p=0.2565$, Student's t-test; $n=7$ mice per genotype). (**D**) Representative immunoblot. Bands corresponding to Na$_V$1.6 (MW: 260 kDa) are visualized in green (Alexa Fluor 790) while bands corresponding to GRP75 (MW: 75 kDa) are visualized in red (Alexa Fluor 680). For both **A** and **C**, circles represent samples from individual mice, horizontal lines represent mean, and error bars represent SEM.

Scn2a^{K1422E} *channels affect pyramidal cell excitability in the neocortex*

Nav1.2 channels are expressed in excitatory pyramidal cells throughout neocortex[52]. To determine whether K1422E channels are functionally expressed in *Scn2a*$^{E/+}$ mice, we performed a series of experiments in neuronal culture and ex vivo using acute slices. First, we established cortical neuron cultures derived from P0 WT and *Scn2a*$^{E/+}$ mice and assessed sodium currents in pyramidal neurons at DIV 15–17. Whole-cell sodium conductance (G_{max}) in *Scn2a*$^{E/+}$ neurons was 28% lower than WT (WT: 4.13 ± 0.40 pS/pF, $n = 17$; *Scn2a*$^{E/+}$: 2.95 ± 0.38 pS/pF, $n = 18$; mean ± standard error of the mean (SEM); $P = 0.0394$, unpaired *t*-test), consistent with lower current density observed in heterologous expression systems. Furthermore, the reversal potential of measured sodium currents was hyperpolarized by ~8 mV in *Scn2a*$^{E/+}$ cells (WT: 80.9 ± 1.5 mV, $n = 17$; *Scn2a*$^{E/+}$: 72.9 ± 1.7 mV, $n = 18$; $P = 0.0012$; **Figure 2.5A & D**). This suggests that K1422E channels are contributing to this current. To further resolve K1422E channels in this preparation, we reassessed currents in the presence of 500 nM TTX + 100 nM Guangitoxin (GxTx) 1E, as the K1422E mutation has been shown to reduce TTX sensitivity[133]. GxTx 1E was included to reduce the contribution of Kv2 potassium channels to whole-cell current[200]. Under these conditions, *Scn2a*$^{E/+}$ neurons produced an appreciable TTX-resistant current that reversed at more hyperpolarized potentials (WT: 58.2 ± 2.7 mV, $n = 14$; *Scn2a*$^{E/+}$: 40.1 ± 1.9 mV, $n = 18$; $P < 0.0001$; **Figure 2.5B & D**). Importantly, the remaining TTX-sensitive current, which is not contaminated by currents mediated by K1422E-containing channels, were comparable to WT with regard to reversal potential (WT: 78.6 ± 1.7 mV, $n = 17$; *Scn2a*$^{E/+}$: 79.8 ± 2.5 mV, $n = 18$; $P = 0.7027$; **Figure 2.5C & D**). Whole-cell current recordings performed in acutely isolated hippocampal neurons from *Scn2a*$^{E/+}$ mice also showed hyperpolarized reversal potentials for total and TTX-sensitive currents, demonstrating the functional expression of K1422E channels in multiple cell types (**Figure 2.6**).

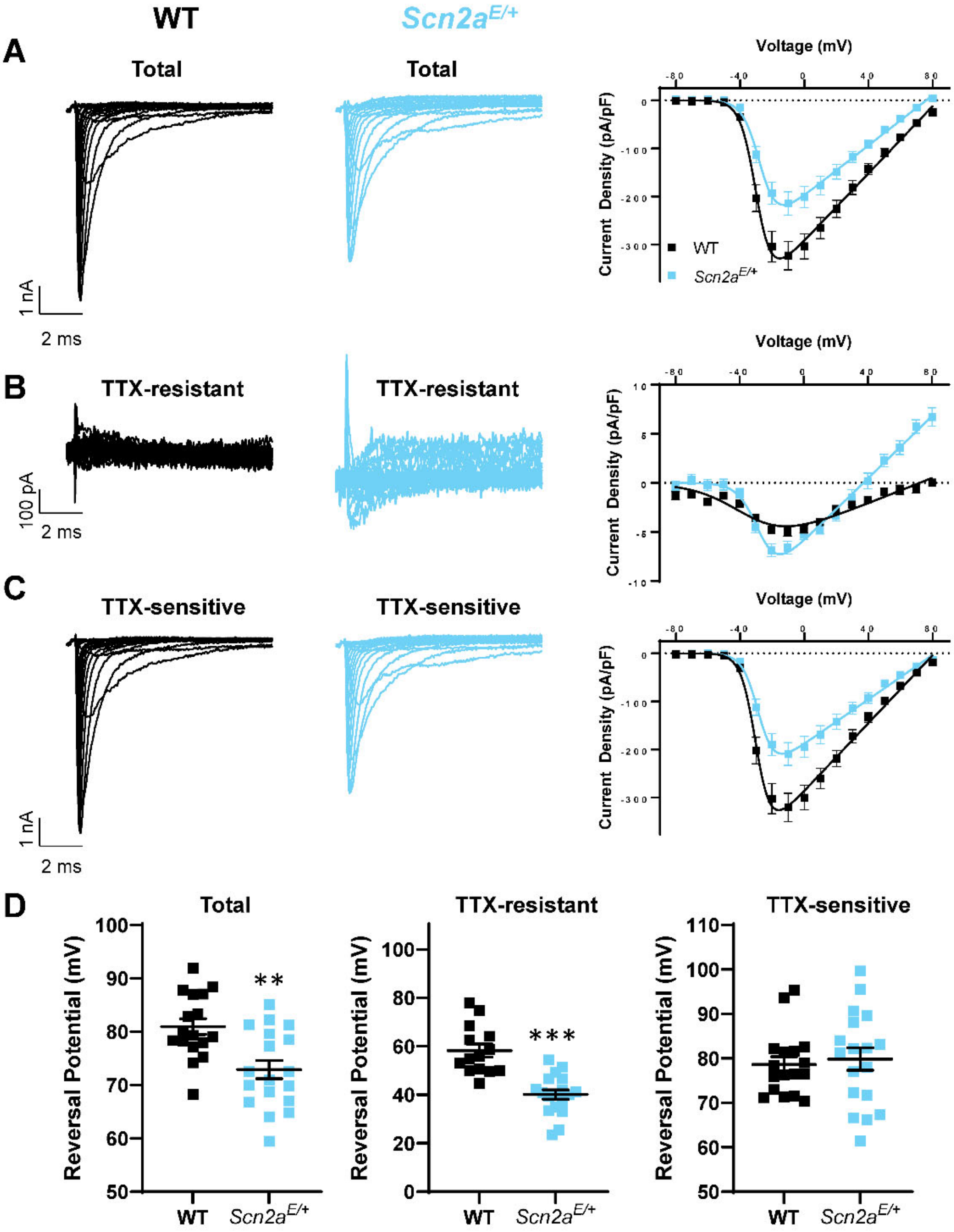

Figure 2.5 Whole-cell sodium currents of cultured cortical pyramidal neurons from WT and *Scn2a*$^{E/+}$ mice. Representative whole-cell sodium currents and current voltage relationships of (**A**) total sodium current, (**B**) TTX-resistant currents, (**C**) TTX-sensitive currents in cultured cortical pyramidal neurons, and (**D**) sodium reversal potential of total sodium current (left, $P = 0.0012$), TTX-resistant current (middle, $P < 0.0001$) and TTX-sensitive currents (right, $P = 0.7027$). All data are plotted as mean ± SEM of $n = 14$–18 cells.

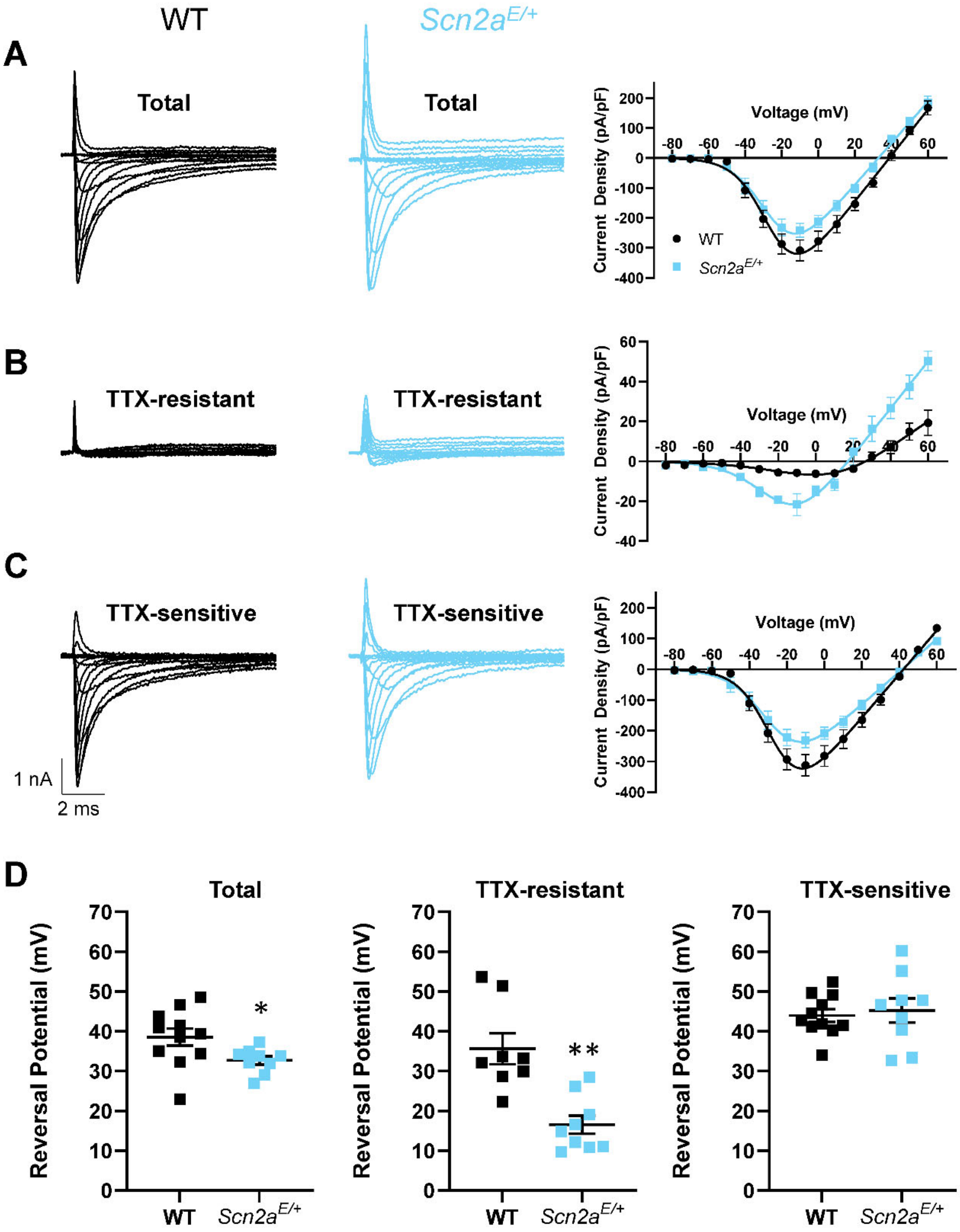

Figure 2.6 Whole-cell sodium currents of acutely isolated hippocampal pyramidal neurons. Representative whole-cell sodium currents and current voltage relationships of (**A**) total sodium current, (**B**) TTX-resistant currents, and (**C**) TTX-sensitive currents from acutely dissociated hippocampal pyramidal neurons from WT and *Scn2a*$^{E/+}$ mice, D) Sodium reversal potential of total sodium current (left, p=0.0364), TTX-resistant current (middle, p=0.0006), and TTX-sensitive currents (right, p=0.6964). All data are plotted as mean ± SEM of n=8-11 cells.

In neocortical pyramidal cells, progressive loss of *Scn2a* alleles, either from constitutive heterozygous knockout, or conditional homozygous knockout, leads to progressive decrements in the speed of the somatic component of an AP[58,125]. Based on the reduced current density observed for K1422E above, we hypothesized that the AP waveform would be similarly affected by this variant. To test this, we made whole-cell current-clamp recordings from layer 5b pyramidal cells in acute slices containing medial prefrontal cortex of $Scn2a^{E/+}$ mice aged P37–45. $Scn2a^{E/+}$ pyramidal cells had slower peak AP speed (WT: 605 ± 18 V/s, $n = 14$; $Scn2a^{E/+}$: 527 ± 21 V/s, $n = 13$; $P = 0.01$, unpaired *t*-test), but were otherwise indistinguishable from cells assayed from littermate controls (**Figure 2.7**). This reduction in AP speed (13%) is smaller than that observed in $Scn2a^{+/-}$ heterozygotes (27%)[125], consistent with a reduction, but not elimination, of current density through channels with the K1422E variant. Furthermore, changes in AP speed were best fit by compartmental model predictions that combined changes in channel permeabilities with a reduction in current density due to calcium antagonism (predicted 16% reduction) (**Figure 2.2**).

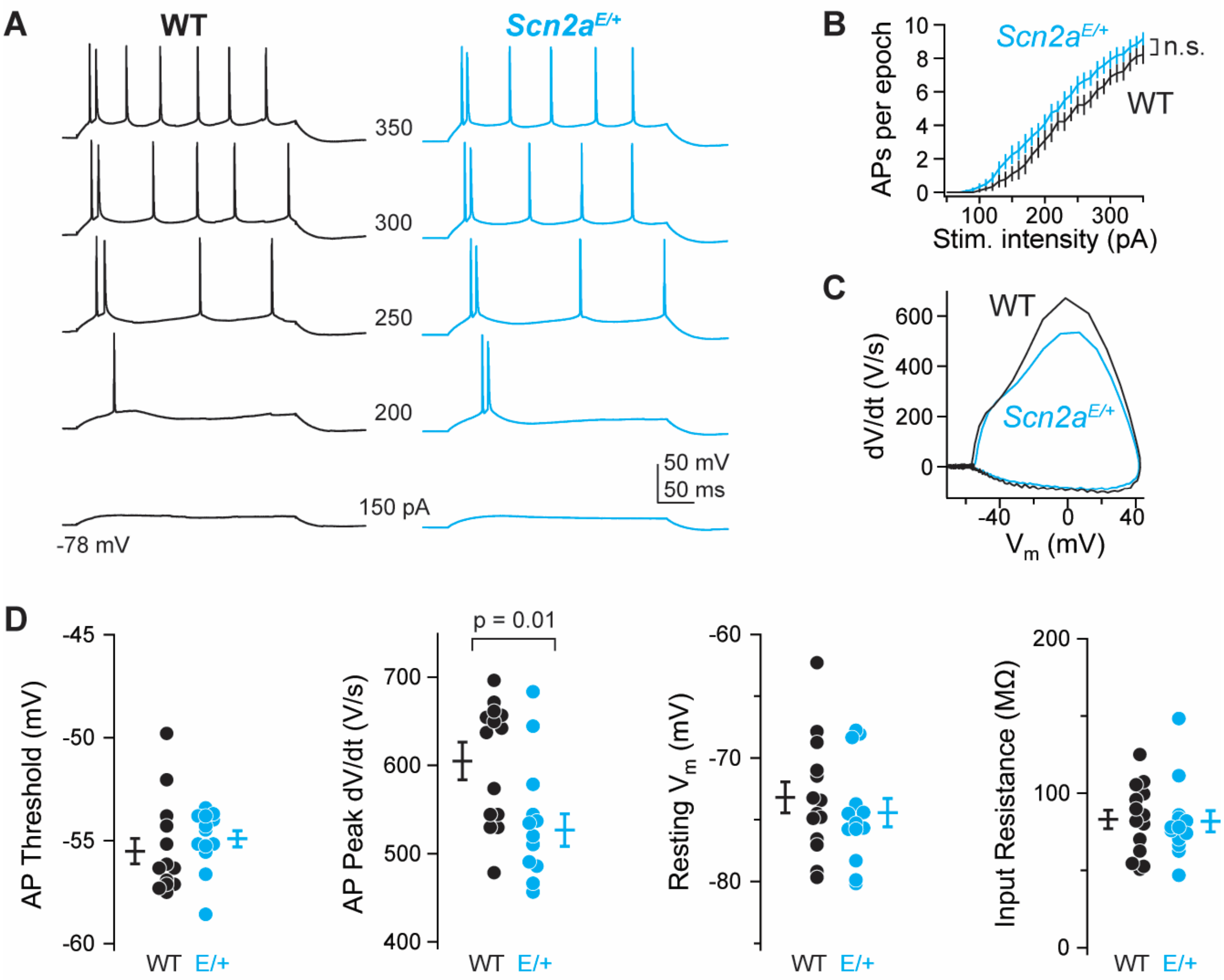

Figure 2.7 *$Scn2a^{E/+}$* prefrontal pyramidal cell AP waveform has LoF characteristics. (**A**) Example whole-cell voltage response to somatic current injection in WT (black) and *$Scn2a^{E/+}$* (K1422E, cyan) neurons. Numbers between examples correspond to current injection amplitude. (**B**) AP number per 300 ms current injection, color coded as in A. Bars are mean ± SEM. *n* = 13 cells each. (**C**) Rheobase AP as dV/dt vs. voltage (phase-plane plot). Note reduction of peak dV/dt for *$Scn2a^{E/+}$* cells compared with WT, indicative of LoF in $Na_V1.2$-mediated somatic depolarization. (**D**) Summaries of AP waveform and intrinsic excitability characteristics. Circles are single cells, bars are mean ± SEM. Peak dV/dt is reduced in *$Scn2a^{E/+}$* cells, unpaired *t*-test. *n* = 14 WT, 13 *$Scn2a^{E/+}$* cells.

These changes in AP waveform further suggest that K1422E-Nav1.2 channels are functional in neocortical pyramidal cells. To test whether calcium influx through Nav1.2 channels can be observed in intact neurons, we imaged AP-evoked calcium transients in the axon initial segment (AIS) with high spatiotemporal precision using 2-photon pointscan imaging. Under normal conditions, calcium influx occurs during AP repolarization in all regions of the axon, including the AIS, and can be separated temporally from sodium influx occurring during AP depolarization[195,201–205]. But in cells expressing K1422E channels, calcium influx may also occur during AP depolarization in regions enriched with Nav1.2 channels. In mature pyramidal neurons, Nav1.2 channels are clustered densely in a region of the AIS proximal to the soma, whereas Nav1.6 channels are enriched in the distal AIS (**Figure 2.8A**)[52]. Therefore, we imaged the proximal and distal initial segment, 5 and 30 μm from the axon hillock, respectively, corresponding to regions enriched or lacking Nav1.2 channels (**Figure 2.8B**). Consistent with a lack of Nav1.2 channels in the distal AIS, there were no differences in the amplitude or timing of AP-evoked calcium transients in the distal AIS. By contrast, calcium transients were larger and occurred earlier, before the peak of the AP, in the proximal AIS of $Scn2a^{E/+}$ cells (Amplitude, WT: 2.8 ± 0.2 $\Delta G/G_{\mathrm{sat}}$, $Scn2a^{E/+}$: 3.8 ± 0.3 $\Delta G/G_{\mathrm{sat}}$, $P = 0.014$; timing relative to AP peak, WT: 0.62 ± 0.15 ms, $n = 12$, $Scn2a^{E/+}$: -0.17 ± 0.13 ms, $n = 10$; $P < 0.001$, unpaired t-test; **Figure 2.8B-D**). Thus, these data indicate that Nav1.2-K1422E channels flux calcium into the cell and that this influx occurs during AP depolarization in the AIS.

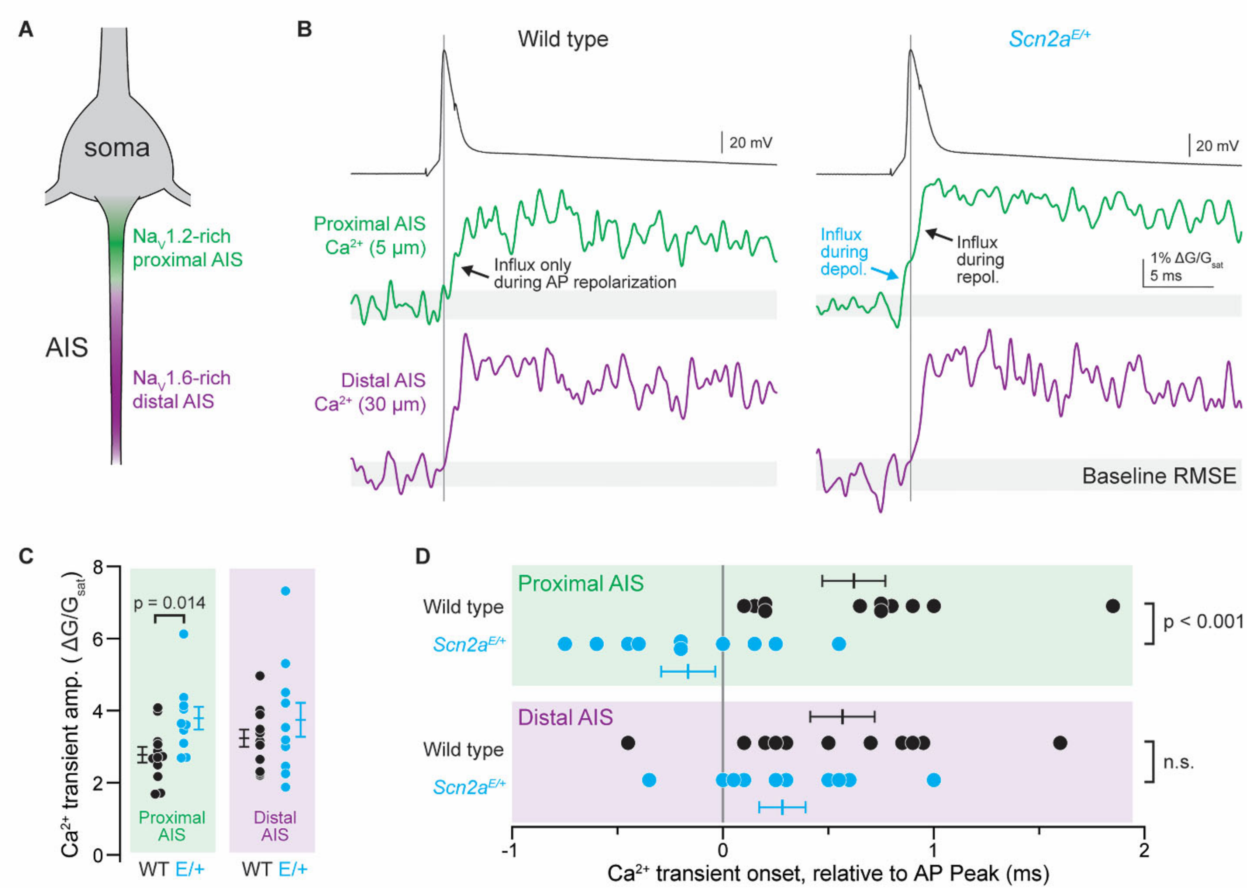

Figure 2.8 AP-evoked Ca^{2+} influx during the rising phase of the AP in the proximal AIS of *Scn2a$^{E/+}$* cells. (**A**) Pyramidal cell initial segments are enriched with Na$_V$1.2 proximal to the soma and Na$_V$1.6 more distal to the soma. Pointscan imaging was performed 5 and 30 µm from the axon hillock, corresponding to Na$_V$1.2 and Na$_V$1.6-enriched regions, respectively. (**B**) Examples of AP-evoked (2 nA, 2 ms stimulus; black, top) calcium transients imaged in pointscan mode in the proximal (green, middle) and distal (violet, bottom) AIS in WT (left) and *Scn2a$^{E/+}$* cells (right). Vertical line is aligned to peak AP voltage. Gray shaded area encompasses imaging signal root-mean-squared error (RMSE) during baseline, before AP. Consistent deviation above this error value defines onset of Ca^{2+} transient. Note Ca^{2+} influx before AP peak in proximal AIS of K1422E condition, only. (**C**) Amplitude of Ca^{2+} transient is higher in proximal AIS of *Scn2a$^{E/+}$* cells, consistent with influx from both local voltage-gated calcium channels and additional influx through K1422E Na$_V$1.2 channels. Circles are single cells and bars are mean ± SEM. *P*-Values from unpaired *t*-tests. (**D**) Ca^{2+} transient onset occurs earlier in the proximal AIS of *Scn2a$^{E/+}$* cells, consistent with Ca^{2+} influx through K1422E Na$_V$1.2 channels. Display as in (C).

Scn2a$^{E/+}$ *mice exhibit abnormalities in EEG and alterations in seizure threshold*

The child with the *SCN2A* p.K1422E variant initially presented with treatment-refractory infantile spasms at 13 months of age and went on to develop other seizure types[85]. Notably, this study used positron emission tomography to assess brain glucose metabolism and did not include (EEG) recordings, which do not always capture seizure events when performed in clinical settings. Therefore, to evaluate *Scn2a*$^{E/+}$ mice for spontaneous seizures and epileptiform events, juvenile (4–6 weeks) mice were implanted with EEG headmounts for video-EEG monitoring which occurred from 5 to 11 weeks of age. *Scn2a*$^{E/+}$ mice exhibited spontaneous seizures that occurred during sleep without any observable behavioral changes (**Figure 2.9A & B**). These seizures occurred rarely (<1 per week) and were not observed in all *Scn2a*$^{E/+}$ mice. Similar events were never observed in WT mice. Furthermore, the seizures were only observed in EEG channel 1, indicating gross localization to the posterior cortical region of the brain. *Scn2a*$^{E/+}$ mice also exhibited interictal epileptiform discharges, including isolated high amplitude spikes with overriding fast activity that had higher power across low and high frequencies up to 170 Hz (**Figure 2.9C & D**). These events occurred at a rate of 2–5 events per 8 h when quantified across a window that included 4 h epochs from the light and dark phases.

Figure 2.9 (caption on next page)

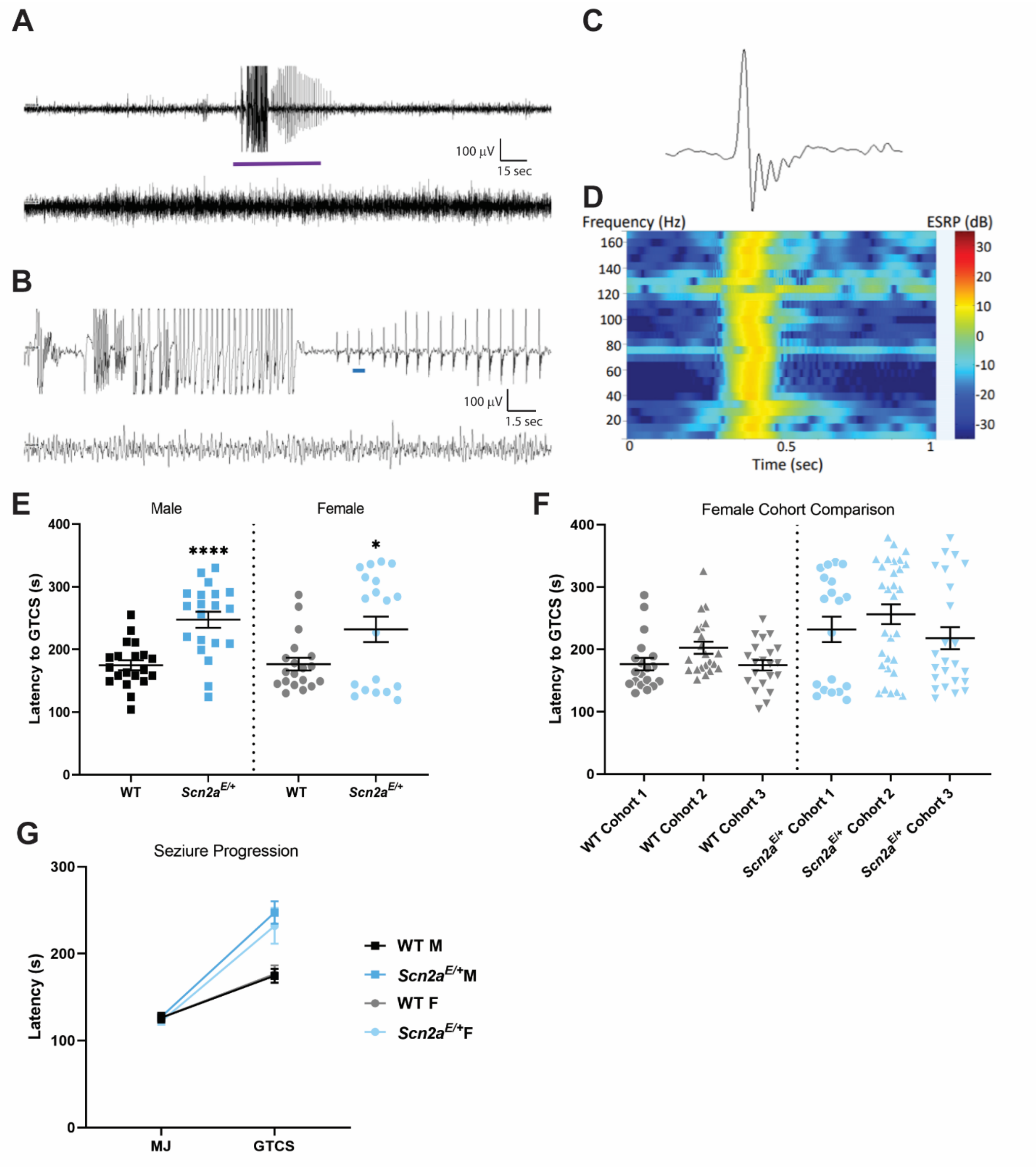

Figure 2.9 EEG abnormalities and altered susceptibility to induced seizures in *Scn2a*$^{E/+}$ mice. Image on previous page. (**A**) Representative 5 min epoch of EEG from *Scn2a*$^{E/+}$ mice. A localized seizure occurred as an abrupt onset of rhythmic 2 Hz sharp waves with overriding fast activity that evolve in amplitude and frequency for ~45 s before abruptly terminating with return to typical sleep background, and (**B**) 30-s epoch corresponding to the purple bar segment from (A). The top line in both (A) and (B) corresponds to channel 1 (right posterior-left posterior) and second line is channel 2 (right anterior-left posterior). (**C**) Example of an isolated high amplitude sharp wave with overriding fast activity corresponding to the blue bar segment in (B). (**D**) Power spectrum for the sharp wave in (C) showing elevated power in decibels across the 1–170 Hz frequency range at the time of discharge. (**E**) Latency to flurothyl-induced GTCS in *Scn2a*$^{E/+}$ mice compared with WT at 6–9 weeks of age. *Scn2a*$^{E/+}$ males had an elevated threshold for flurothyl-induced seizures compared with WT (WT: 175 ± 8 s, *Scn2a*$^{E/+}$: 247 ± 13 s, $^{****}P < 0.0001$; Welch's *t*-test). *Scn2a*$^{E/+}$ females also had an elevated threshold for flurothyl-induced seizures compared with WT (WT: 177 ± 10 s, *Scn2a*$^{E/+}$: 232 ± 20 s, $^{*}P = 0.0282$; Kolmogorov–Smirnov test). Symbols represent samples from individual mice, horizontal lines represent mean and error bars represent SEM. (**F**) Latency to first flurothyl-induced generalized tonic–clonic seizure (GTCS) in WT and *Scn2a*$^{E+}$ female mice across multiple cohorts ($n = 19$–23 per genotype and cohort). Cohorts were evaluated at different times. Data from *Scn2a*$^{E/+}$ females show non-normal distribution in all three cohorts compared with cohort-matched WT controls. (**G**) Average latency to first myoclonic jerk (MJ) and GTCS, with connecting line depicting time of progression between stages. There was no genotype difference in latency to first MJ for both sexes (**Table 2.2**). However, progression between stages was slower for both male and female *Scn2a*$^{E/+}$ mice compared with WT (Males: $P < 0.0001$; Mann–Whitney test; Females: $P = 0.0350$, Kolmogorov–Smirnov test). Symbols represent group mean and error bars represent SEM; $n = 19$–20/sex/genotype Males and females were analyzed separately.

Since these spontaneous seizures in *Scn2a*$^{E/+}$ mice appear to be rare and difficult to observe due to a lack of an obvious behavioral component, we next asked how the *Scn2a*^{K1422E} variant affects seizure susceptibility in an induced-seizure paradigm. We used the volatile chemoconvulsant flurothyl (Bis(2,2,2-trifluoroethyl) ether), a γ-aminobutyric acid A (GABA$_A$) antagonist[206], to induce a stereotyped progression to generalized tonic–clonic seizures (GTCS) in juvenile (6–9 weeks of age) *Scn2a*$^{E/+}$ and WT mice. While latency to first myoclonic jerk (MJ) was not affected by genotype, latency to first GTCS (defined as characteristic limb flexion/extension with loss of posture) was affected by genotype (**Table 2.2**). Both male and female *Scn2a*$^{E/+}$ mice had a higher threshold for flurothyl-induced seizures compared with sex-matched WT littermates ($P < 0.0001$

for males; $P = 0.0282$ for females). Average latency was 247 ± 13 s for *Scn2a*$^{E/+}$ males, 175 ± 8 s for WT males, 257 ± 21 s for *Scn2a*$^{E/+}$ females and 177 ± 10 s for WT females (**Figure 2.9E**). We also noted that the data reflecting latency to first GTCS in *Scn2a*$^{E/+}$ females was non-normally distributed compared with data from WT females. This effect was reproducible in three separate cohorts of *Scn2a*$^{E/+}$ and WT females (**Figure 2.9F**). Time to progress from the first MJ to the first GTCS was also affected by genotype (**Table 2.2**). Both male and female *Scn2a*$^{E/+}$ mice progressed more slowly compared with sex-matched WT controls ($P < 0.0001$ for males and $P = 0.035$ for females). Average progression time was 120 ± 13 s for *Scn2a*$^{E/+}$ males versus 48 ± 8 s for WT males, and 109 ± 19 s for *Scn2a*$^{E/+}$ females versus 52 ± 10 s for WT females (**Figure 2.9G**). The above data suggest that rare spontaneous seizures occur in *Scn2a*$^{E/+}$ mice, but they remain localized rather than generalized. Furthermore, slower progression to flurothyl-induced GTCS indicates resistance to seizure spreading in *Scn2a*$^{E/+}$ mice, consistent with the localized nature of spontaneous seizures observed using EEG.

Lower anxiety-related behavior in Scn2a$^{E/+}$ *mice*

Anxiety-related behavior is frequently assessed in mouse models of ASD-related genes, including *Scn2a*[58,111,112,120]. We used zero maze, light–dark exploration, and open field assays to assess anxiety-related behavior in *Scn2a*$^{E/+}$ and WT mice. These assays take advantage of mouse thigmotaxis and phototaxic aversion to define anxiety-related behavior. More time spent in exposed, well-lit areas compared with dark, enclosed areas indicates lower anxiety-related behavior. In the zero-maze assay, time spent in the open versus closed arms of the maze was significantly higher in both male and female *Scn2a*$^{E/+}$ mice compared with sex-matched WT controls ($P = 0.0023$ for males; $P = 0.0297$ for females, respectively). On average, *Scn2a*$^{E/+}$ males spent nearly twice as long (30.5 ± 4.1%) in the open arms compared with WT males (15.3 ± 2.2%; **Figure 2.10A**). *Scn2a*$^{E/+}$ females also spent more time in the open arms (34.8 ± 4.9%) compared with WT females (22.0 ± 2.0%; **Figure 2.10A**). During the light–dark exploration assay, time spent in the exposed light zone versus the enclosed dark zone was significantly affected by genotype ($P = 0.0367$ for both male and female comparisons). On average, *Scn2a*$^{E/+}$ males spent more time (29.2 ± 3.2%) in the light zone compared with WT males (20.9 ± 2.0%; **Figure 2.10B**). *Scn2a*$^{E/+}$ females also spent more time in the light zone (32.1 ± 3.5%) compared with WT females (21.1 ± 1.7%; **Figure 2.10B**). In the open field assay, time spent in the exposed center zone of the apparatus versus the periphery was significantly affected by genotype when comparing *Scn2a*$^{E/+}$ and WT females ($P = 0.0167$), but not when comparing males ($P = 0.0556$). However, the overall genotype effect recapitulated what was seen in the zero maze and light–dark exploration assays, with *Scn2a*$^{E/+}$ females spending an average of 10.1 ± 1.2% of test time in the center zone and WT females averaging 6.27 ± 0.9% of time (**Figure 2.10C**).

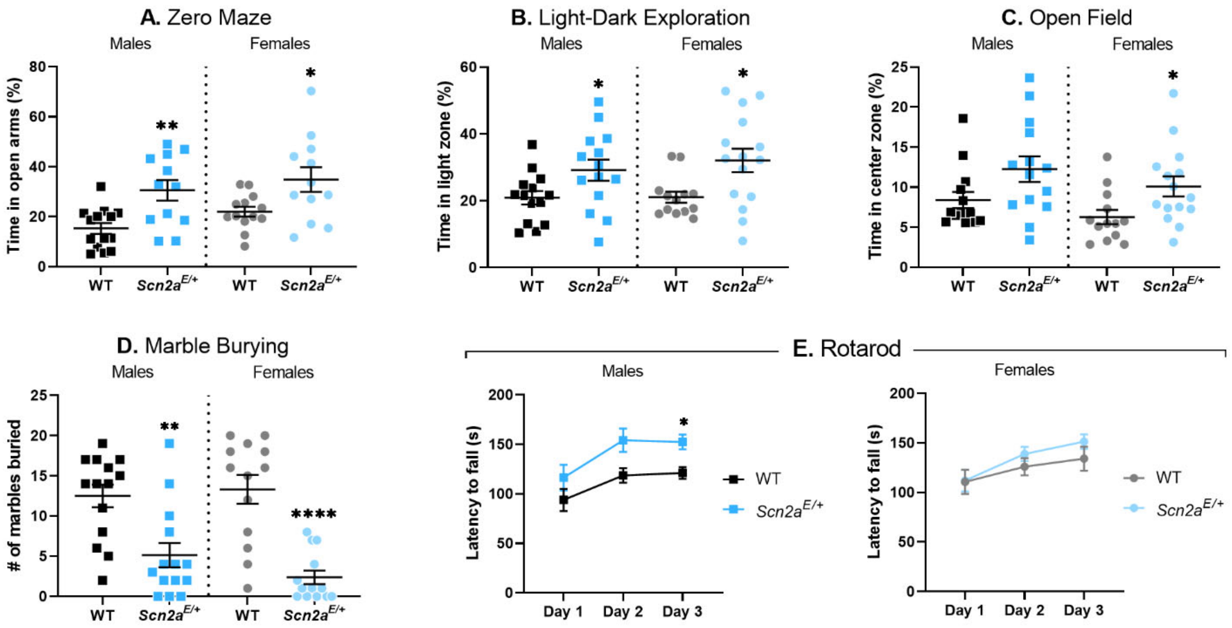

Figure 2.10 Altered anxiety-related behavior and rotarod performance in *Scn2a*$^{E/+}$ mice. (**A**) Percent time spent in the open arms of a zero-maze apparatus in *Scn2a*$^{E/+}$ mice compared with WT at 6 weeks of age. *Scn2a*$^{E/+}$ males spent significantly more time in the open arms compared with WT (WT: 15.3 ± 2.2%, *Scn2a*$^{E/+}$: 30.5 ± 4.1%, $^{**}P = 0.0023$; Student's *t*-test). *Scn2a*$^{E/+}$ females spent significantly more time in the open arms compared with WT (WT: 22.0 ± 2.0%, *Scn2a*$^{E/+}$: 34.8 ± 4.9%, $^{*}P = 0.0297$; Welch's *t*-test). (**B**) Percent time spent in the light zone of a light/dark box in *Scn2a*$^{E/+}$ mice compared with WT at 7 weeks of age. *Scn2a*$^{E/+}$ males spent significantly more time in the light zone compared with WT (WT: 20.9 ± 2.0%, *Scn2a*$^{E/+}$: 29.2 ± 3.2%, $^{*}P = 0.0367$; Student's *t*-test). *Scn2a*$^{E/+}$ females also spent significantly more time in the light zone compared with WT (WT: 21.1 ± 1.7%, *Scn2a*$^{E/+}$: 32.1 ± 3.5%, $^{*}P = 0.0367$; Mann–Whitney test). (**C**) Percent time spent in the center zone of an open field apparatus in *Scn2a*$^{E/+}$ mice compared with WT at 8 weeks of age. There was not a significant difference in the amount of time spent in the center zone between *Scn2a*$^{E/+}$ and WT males ($P = 0.0556$, Mann–Whitney test). However, *Scn2a*$^{E/+}$ females spent significantly more time in the center zone compared with WT (WT: 6.27 ± 0.9%, *Scn2a*$^{E/+}$: 10.1 ± 1.2%, $^{*}P = 0.0167$; Mann–Whitney test). (**D**) Number of marbles buried during a 30-min trial by *Scn2a*$^{E/+}$ mice compared with WT at 6 weeks of age is displayed. *Scn2a*$^{E/+}$ males buried significantly fewer marbles compared with WT (WT: 12 ± 1, *Scn2a*$^{E/+}$: 5 ± 2, $^{**}P = 0.0019$; Mann–Whitney test). *Scn2a*$^{E/+}$ females also buried significantly fewer marbles compared with WT (WT: 13 ± 2, *Scn2a*$^{E/+}$: 2 ± 1, $^{****}P = 0.0001$; Mann–Whitney test). (**E**) Average latency to fall during an accelerating rotarod task measured on three consecutive days in *Scn2a*$^{E/+}$ mice compared with WT at 9 weeks of age. Daily performance for each animal was assessed by averaging across three trials. Two-way repeated measures ANOVA comparing average latency to fall between *Scn2a*$^{E/+}$ and WT males showed significant main effects of test day [$F(1.511, 34.76) = 8.450$, $^{**}P = 0.0022$] and genotype [$F(1,23) = 10.18$, $^{*}P = 0.0041$]. *Scn2a*$^{E/+}$ males took significantly longer to fall compared with WT on day 3 (WT: 121 ± 6 s, *Scn2a*$^{E/+}$: 152 ± 7 s, $P = 0.0106$; Sidak's post-hoc test). Two-way repeated measures ANOVA comparing average latency to fall between *Scn2a*$^{E/+}$ and WT females showed a significant main effect of test day only [$F(1.594,36.65) = 6.646$, $^{**}P = 0.0059$]. For panels (A–D) symbols represent individual mice, horizontal lines represent mean and error bars represent SEM. For panel (E) symbols and error bars represent mean ± SEM. Males and females were analyzed separately, with $n = 12$–14 per genotype for males and $n = 11$–15 per genotype for females.

Data from our initial set of behavioral assays suggested that *Scn2a*$^{E/+}$ mice showed lower anxiety-like behavior compared with WT controls. To further clarify these behavioral abnormalities with regard to compulsivity, we used a marble burying assay. Both *Scn2a*$^{E/+}$ males and females buried significantly fewer marbles compared with WT controls (males, WT: 13 ± 1, *Scn2a*$^{E/+}$: 5 ± 2, $P = 0.0019$; females, WT: 13 ± 2, *Scn2a*$^{E/+}$: 2 ± 1, $P < 0.0001$; **Figure 2.10D**). Early on, it became apparent that some animals were not burying the marbles and a limited number of subsequent trials were video recorded. We observed normal exploratory behavior in recordings where animals did not bury the marbles, suggesting that the observed genotype effect on marble burying was due to lower anxiety-like behavior rather than inactivity.

Enhanced rotarod performance in Scn2a$^{E/+}$ *male mice*

Movement disorders have been reported in some children with *SCN2A*-associated DEE[35] and deficits in motor function could potentially confound results from other behavioral assays. Therefore, we used an accelerating rotarod assay to evaluate motor coordination and balance in *Scn2a*$^{E/+}$ mice compared with WT controls at 9 weeks of age. For each subject, latency to fall was measured for three trials and daily performance was assessed by averaging across trials. Two-way repeated measures analysis of variance (ANOVA) showed significant main effects of test day and genotype when comparing average latency to fall between *Scn2a*$^{E/+}$ males and WT controls (**Table 2.2**). *Scn2a*$^{E/+}$ males spent significantly more time on the rotarod compared with WT males by the third day of testing ($P = 0.0106$). On day three of testing, average latency to fall was 121 ± 6 s for WT males and 152 ± 7 s for *Scn2a*$^{E/+}$ males (**Figure 2.10E**). Two-way repeated measures ANOVA only showed a significant main effect of test day when comparing *Scn2a*$^{E/+}$ and WT females (**Table 2.2**). These data indicate that basic motor function in *Scn2a*$^{E/+}$ remains intact.

Altered social behavior in Scn2a$^{E/+}$ mice

As previously noted, ASD or features of ASD are frequently reported in children with *SCN2A* variants, including SCN2A-p.K1422E[85]. Social behavior deficits are a common feature of ASD[1] and have been extensively studied in animal models of ASD-related gene disruptions[120,121]. We used a three-chamber assay, which takes advantage of innate preferences for novel social interactions, to evaluate social behavior in *Scn2a*$^{E/+}$ mice compared with WT controls at 10 weeks of age. During the sociability phase, time spent sniffing either a novel object (empty wire cup) or an unfamiliar mouse was measured (**Figure 2.11A**). Two-way ANOVA comparing average sniffing time between *Scn2a*$^{E/+}$ males and WT controls during the sociability phase showed a significant main effect of target and a significant interaction between target and genotype (**Table 2.2**). On average, *Scn2a*$^{E/+}$ males spent significantly more time (132.6 ± 8.3 s) sniffing an unfamiliar mouse compared with WT (93.3 ± 12.7 s; **Figure 2.11A**). Two-way ANOVA showed only a significant main effect of target when comparing average sniffing time between *Scn2a*$^{E/+}$ females and WT controls during the sociability phase (**Table 2.2**). These data suggest that preference for social interactions is intact for both male and female *Scn2a*$^{E/+}$ mice, while *Scn2a*$^{E/+}$ males, but not females, display a greater preference for social interactions compared with WT. During the social novelty phase, time spent sniffing either a familiar mouse or an unfamiliar mouse was measured (**Figure 2.11B**). Two-way ANOVA showed significant main effects of target and genotype when comparing average sniffing time between *Scn2a*$^{E/+}$ and WT males during the social novelty phase (**Table 2.2**). On average, *Scn2a*$^{E/+}$ males spent significantly more time (77.1 ± 5.7 s) sniffing an unfamiliar mouse compared with WT males (48.8 ± 8.7 s; **Figure 2.11B**). Two-way ANOVA also showed significant main effects of target and genotype when comparing average sniffing time between *Scn2a*$^{E/+}$ females and WT controls during the social novelty phase (**Table 2.2**). On average, *Scn2a*$^{E/+}$ females spent 61.9 ± 7.7 s sniffing an unfamiliar mouse, while WT females spent 41.6 ± 4.5 s sniffing an unfamiliar mouse (**Figure 2.11B**). These data suggest that preference for social novelty is intact for both male and female *Scn2a*$^{E/+}$ mice, and that *Scn2a*$^{E/+}$ males, but not females, display a greater preference for social novelty compared with WT.

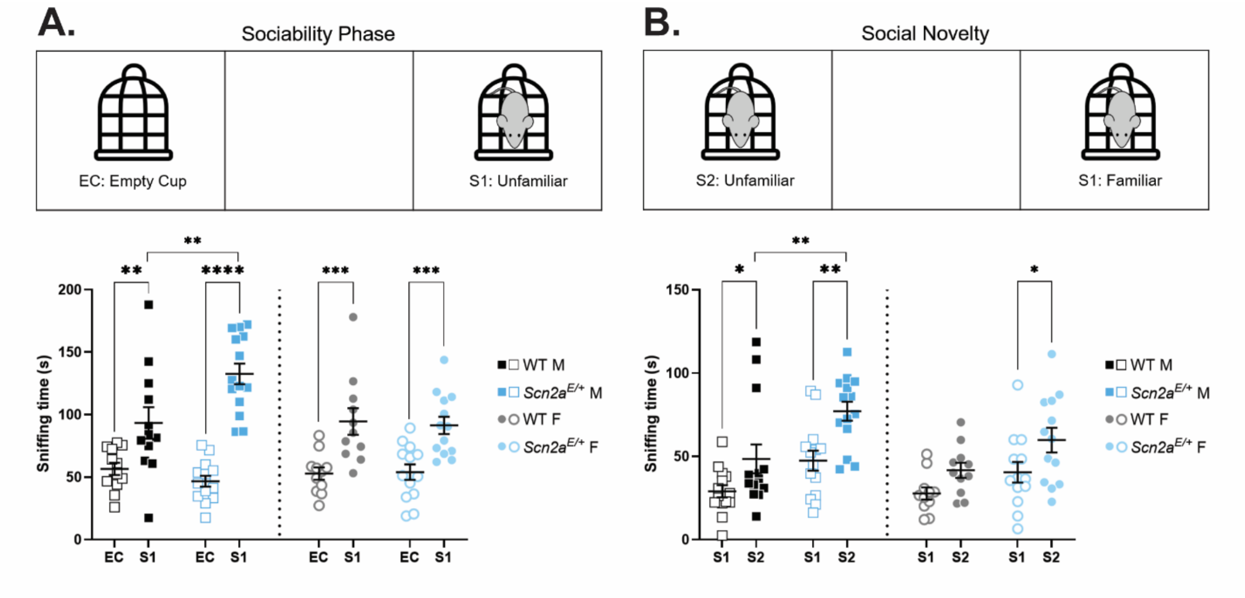

Figure 2.11 Altered social behavior in *Scn2a*$^{E/+}$ mice. (**A**) Sociability phase of three-chamber assay. Amount of time spent sniffing either an empty cup (EC) or unfamiliar mouse (S1) in *Scn2a*$^{E/+}$ mice compared with WT at 10 weeks of age. Two-way ANOVA (using target as a within-subject variable) comparing average sniffing time between *Scn2a*$^{E/+}$ and WT males showed a significant main effect of target [$F(1,24) = 57.28$, $P < 0.0001$] and a significant interaction between target and genotype [$F(1,24) = 9.198$, $P = 0.0057$]. Both *Scn2a*$^{E/+}$ and WT males spent significantly more time sniffing an unfamiliar mouse compared with an empty cup (*Scn2a*$^{E/+}$: $^{****}P < 0.0001$, WT: $^{**}P = 0.0100$; Sidak's post-hoc test). However, *Scn2a*$^{E/+}$ males spent significantly more time sniffing an unfamiliar mouse compared with WT males (WT: 93.3 ± 12.7 s, *Scn2a*$^{E/+}$: 132.6 ± 8.3 s, $^{**}P = 0.0024$; Sidak's post-hoc test). Two-way ANOVA comparing average sniffing time between *Scn2a*$^{E/+}$ and WT females showed a significant main effect of target only [$F(1,22) = 35.17$, $P < 0.0001$]. Both *Scn2a*$^{E/+}$ and WT females spent significantly more time sniffing an unfamiliar mouse compared with an empty cup (*Scn2a*$^{E/+}$: $^{***}P < 0.0007$, WT: $^{***}P < 0.0008$; Sidak's post-hoc test). (**B**) Social novelty phase of three-chamber assay. Amount of time spent sniffing either a familiar mouse (S1) or an unfamiliar mouse (S2) in *Scn2a*$^{E/+}$ mice compared with WT at 10 weeks of age. Two-way ANOVA (using target as a within-subject variable) comparing average sniffing time between *Scn2a*$^{E/+}$ and WT males showed significant main effects of target [$F(1,26) = 19.02$, $P = 0.0002$] and genotype [$F(1,21) = 11.85$, $P = 0.0020$]. Both *Scn2a*$^{E/+}$ and WT males spent significantly more time sniffing an unfamiliar mouse compared with a familiar mouse (*Scn2a*$^{E/+}$: $^{**}P = 0.0019$, WT: $^{*}P = 0.0432$; Sidak's post-hoc test). However, *Scn2a*$^{E/+}$ males spent significantly more time sniffing an unfamiliar mouse compared with WT males (WT: 48.5 ± 8.7 s, *Scn2a*$^{E/+}$: 77.1 ± 5.7.3 s, $^{**}P = 0.0042$; Sidak's post-hoc test). Two-way ANOVA comparing average sniffing time between *Scn2a*$^{E/+}$ and WT females also showed significant main effects of target [$F(1,22) = 9.145$, $P = 0.0062$] and genotype [$F(1,22) = 6.081$, $P = 0.0219$]. However, only *Scn2a*$^{E/+}$ females spent significantly more time sniffing an unfamiliar mouse compared with a familiar mouse (*Scn2a*$^{E/+}$: $^{*}P = 0.0327$, WT: $P = 0.1889$; Sidak's post-hoc test). Symbols represent individual mice, horizontal lines represent mean and error bars represent SEM. Males and females were analyzed separately, with $n = 12–14$ per genotype for males and $n = 11–13$ per genotype for females.

Lower olfactory dishabituation to social odors in Scn2a$^{E/+}$ mice

The three-chamber assay described above measures sniffing time as the variable of interest and could therefore be affected by deficits in olfactory discrimination. We used an olfactory habituation/dishabituation assay to evaluate olfactory discrimination in *Scn2a*$^{E/+}$ mice compared with WT controls at 11 weeks of age. Each odorant (water, almond extract, banana extract, same sex urine, opposite sex urine) was presented for three consecutive trials before proceeding to the next odor in the sequence for a total of 15 trials. Time spent sniffing the odor delivery apparatus was measured for each trial and compared between genotypes. Habituation refers to a decrease in sniffing behavior upon repeated presentation of an odor, while dishabituation refers to an increase in sniffing behavior upon presentation of a novel odor. Qualitatively, olfactory discrimination and preference for social odors appear to be intact for both male and female *Scn2a*$^{E/+}$ mice (**Figure 2.12A**). However, the amount of time *Scn2a*$^{E/+}$ males spent sniffing same sex urine during the first two presentations was over 50% lower than WT males ($P = 0.0005$ and $P = 0.0307$, respectively). During the first presentation, average sniffing time was 42.3 ± 3.3 s for WT males and 18.8 ± 3.4 s for *Scn2a*$^{E/+}$ males, while average sniffing time for the second presentation was 26.3 ± 8.9 s for WT males and 8.9 ± 2.1 s for *Scn2a*$^{E/+}$ males (**Figure 2.12A**). *Scn2a*$^{E/+}$ females also spent significantly less time sniffing same sex urine compared with WT females, but only during the first presentation ($P = 0.0045$). Average sniffing time was 46.3 ± 4.6 s for WT females and 19.9 ± 4.2 s for *Scn2a*$^{E/+}$ females (**Figure 2.12A**).

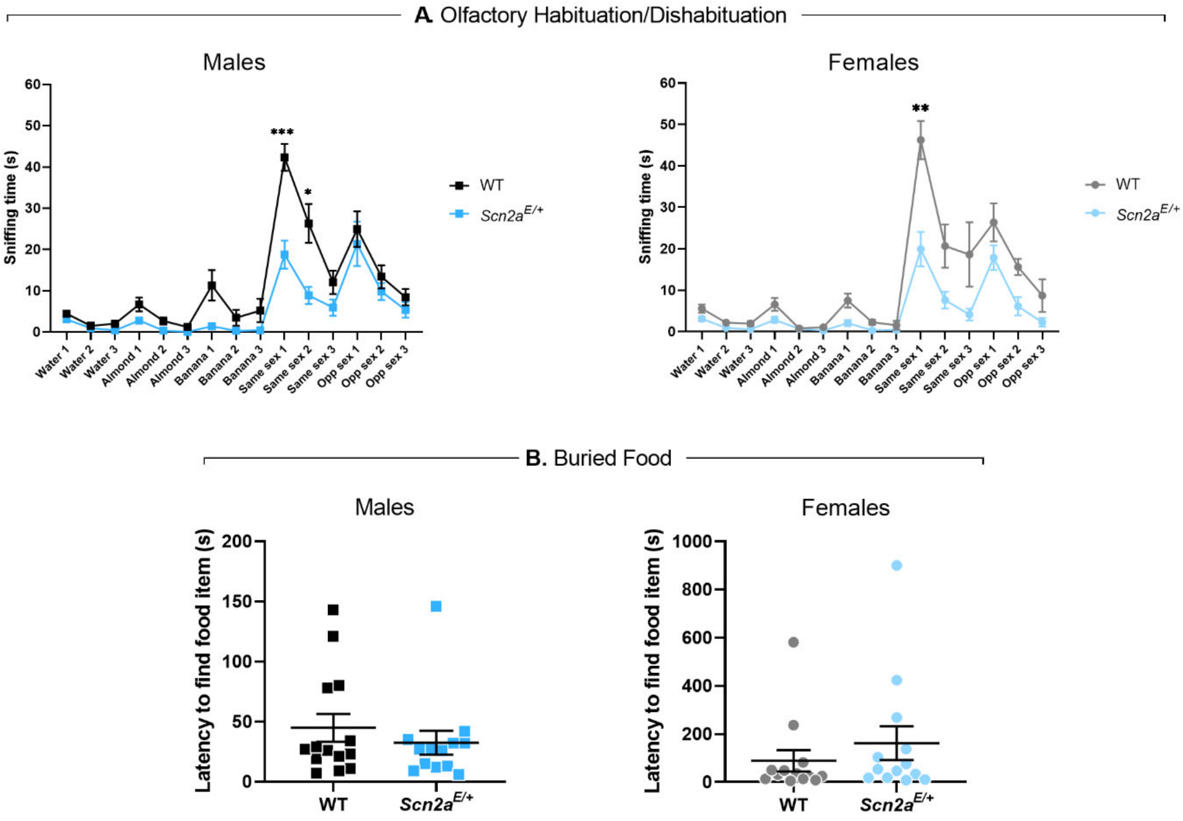

Figure 2.12 Lower olfactory dishabituation to social odors and intact olfactory-guided behavior in *Scn2a*$^{E/+}$ mice. (**A**) Average sniffing times during an odor habituation/dishabituation assay in *Scn2a*$^{E/+}$ mice compared with WT at 11 weeks of age. Overall, olfactory discrimination in *Scn2a*$^{E/+}$ males was not significantly different from WT males. However, *Scn2a*$^{E/+}$ males spent significantly less time sniffing same sex urine during the first two presentations compared with WT males. During the first presentation, average sniffing time was 42.3 ± 3.3 s for WT males and 18.8 ± 3.4 s for *Scn2a*$^{E/+}$ males ($^{***}P = 0.0005$, multiple *t*-tests). During the second presentation, average sniffing time was 26.3 ± 8.9 s for WT males and 8.9 ± 2.1 s for *Scn2a*$^{E/+}$ males ($^{*}P = 0.0307$, multiple *t*-tests). Olfactory discrimination in *Scn2a*$^{E/+}$ females was also not significantly different from WT females. However, *Scn2a*$^{E/+}$ females spent significantly less time sniffing same sex urine during the first presentation compared with WT females (WT: 46.3 ± 4.6 s, *Scn2a*$^{E/+}$: 19.9 ± 4.2 s, $^{**}P = 0.0045$, multiple *t*-tests). Symbols and error bars represent mean ± SEM. Males and females were analyzed separately, with $n = 14$ per genotype for males and $n = 12$–13 per genotype for females. (**B**) Latency to find a buried food item in *Scn2a*$^{E/+}$ mice compared with WT at 8 weeks of age. Latency to find a buried food item was not significantly different between *Scn2a*$^{E/+}$ and WT males (WT: 44.86 ± 11.58 s, *Scn2a*$^{E/+}$: 32.46 ± 9.95 s, $P = 0.7471$; Mann–Whitney test). Latency to find a buried food item was not significantly different between *Scn2a*$^{E/+}$ and WT females (WT: 89.00 ± 44.31 s, *Scn2a*$^{E/+}$: 161.7 ± 70.02, $P = 0.2927$; Mann–Whitney test). Symbols represent measured values from individual mice, horizontal lines represent mean and error bars represent SEM. Males and females were analyzed separately, with $n = 13$–14 per genotype for males and $n = 13$ per genotype for females.

The three-chamber and olfactory habituation/dishabituation assays suggest that olfactory-guided behavior is altered in *Scn2a*$^{E/+}$ mice and that these effects were more pronounced for social odors. In order to exclude the possibility that olfaction was globally affected, we used a buried food task to compare a separate cohort of *Scn2a*$^{E/+}$ mice and WT controls at 9 weeks of age. Task performance was evaluated by measuring the amount of time it took for food-deprived subjects to locate a hidden food stimulus. Both male and female *Scn2a*$^{E/+}$ mice performed as well as sex-matched WT controls (males, WT: 44.86 ± 11.58 s, *Scn2a*$^{E/+}$: 32.46 ± 9.95 s, $P = 0.7471$; females, WT: 89.00 ± 44.31 s, *Scn2a*$^{E/+}$: 161.7 ± 70.02, $P = 0.2927$; **Figure 2.12B**), indicating that olfaction remains intact.

2.4 Discussion

SCN2A variants have been associated with a wide range of NDD that reflect a complex spectrum of phenotypes[35]. Significant attention has been given to the far ends of this phenotypic spectrum, establishing a framework in which *SCN2A* missense variants that result in strong GoF effects are associated with DEE, while PTVs that result in LoF effects are associated with ID/ASD that sometimes present with co-morbid seizures starting later in life[70,71,74,81,82]. More recently, attempts have been made to further refine the genotype–phenotype relationships of *SCN2A*-related disorders[102], an effort that can be supported by animal models of variants with properties that do not fit easily into GoF or LoF categories. Here, we focused on the variant *SCN2A*-p.K1422E, which we and others have shown alters ion channel selectivity in heterologous expression systems[130,132]. We further characterized cellular and behavioral phenotypes associated with this unique variant in a newly generated mouse model (*Scn2a*^{K1422E}). Excitatory neurons in neocortex from *Scn2a*$^{E/+}$ mice displayed lower sodium current density, although the magnitude of the effect was less pronounced than in haploinsufficient models[54,114]. In addition, there was a TTX-insensitive component with altered reversal potential, and aberrant calcium influx that occurs during the rising phase of the AP localized to Nav1.2-rich regions of the AIS, indicating that the variant channel is functionally expressed in these cells. *Scn2a*$^{E/+}$ mice also display neurological/neurobehavioral phenotypes, including infrequent spontaneous seizures, lower anxiety-like behavior, and alterations in olfactory-guided behavior. Although some neurobehavioral phenotypes overlap with those observed in other models of *Scn2a* haploinsufficiency, *Scn2a*$^{E/+}$ also exhibit unique seizure phenotypes that likely reflect complex effects of K1422E on Nav1.2 channel function.

Effects of altered Nav1.2 ion selectivity on neuronal function

Vertebrate voltage-gated sodium channels contain four highly conserved residues (DEKA) that confer selectivity for sodium[35,40]. These channels evolved from a primordial channel with mixed selectivity, where the selectivity filter has a glutamic acid (E) substituted for lysine (K) in the 3rd transmembrane domain[41,42]. Thus, the K1422E variant can be seen as an evolutionary reversion at the selectivity filter[32,33]. Consistent with previous work on rat Nav1.2 channels in *Xenopus* oocytes[130], we show that substitution of glutamic acid for lysine at position 1422 (DEKA to DEEA) in human Nav1.2 confers calcium permeability not evident in WT human Nav1.2 channels (**Figure 2.1B**). Additionally, we are the first to demonstrate this effect in neurons.

Before the existence of sodium channels, cellular depolarization was mediated by calcium-selective channels or nonselective cation channels[32,33]. As such, changes in membrane potential were linked to alterations in intracellular calcium and associated downstream calcium-dependent signaling. Sodium channels are thought to have evolved in part to allow cells to separate changes in voltage from calcium signaling. What effects, then, could arise from recombining these processes in Nav1.2 channels? Within the AIS, we show that calcium influx occurs both before and after the peak of the AP in K1422E-expressing neurons (**Figure 2.8B-D**). This contrasts with typical conditions where sodium and calcium influx are separated on the rising and falling phases of the AP, respectively[195,204]. Consistent with what was predicted from our compartmental neuron model, we show that *Scn2a*$^{E/+}$ pyramidal cells had slower peak AP speed compared with WT (**Figure 2.7C & D**). This is likely associated with reduced current density through the channel, with at least partial contribution from calcium antagonism[130]. This reduction in AP speed (13%) is smaller than that observed in *Scn2a*$^{+/-}$ heterozygotes (27%)[125], consistent with a reduction, but not elimination, of current density through channels with the K1422E variant. It has been shown that progressively severe deficiency of Nav1.2 expression is associated with paradoxical and cell-autonomous hyperexcitability in excitatory neurons from the neocortex and striatum[125,126]. We observed a similar, but ultimately non-significant effect on AP firing rate in *Scn2a*$^{E/+}$ pyramidal cells, suggesting that this is likely not the primary pathophysiological mechanism in this cell type. However, additional calcium influx could have myriad effects on AIS function, as many AIS components are regulated directly by calcium or through calcium/calmodulin interactions[207–210]. Additionally, excess calcium influx could affect cellular processes beyond the AIS as Nav1.2 channels are also expressed in the somatodendritic domain and throughout the axons of unmyelinated neurons[56,65,66,211,212]. During high-frequency activity, intracellular sodium concentrations can exceed 50 mM in some nerve terminals[212]. Excess calcium influx through K1422E channels could therefore affect transmitter release and short-term presynaptic plasticity[213,214]. Nav1.2 channels also influence dendritic excitability in neocortex[58]. Thus, excess calcium may affect dendritic integration/plasticity, depending on the location of these channels relative to synaptic inputs.

Based on modeling of biophysical data here and in previous reports[130], we estimated relative permeabilities of K1422E channels to be Na^+, K^+ and Ca^{2+} to be 1:0.7:0.8. Interestingly, some invertebrates express more primitive Nav1 channels containing the DEKA selectivity filter that nevertheless appear to have some calcium permeability[43]. This suggests that additional aspects of Nav1 evolution, including changes to other residues lining the pore may confer additional ion selectivity/permeability properties[44]. Consistent with this, recurrent *SCN2A* missense variants that affect pore-adjacent arginine residues R379 and R937 eliminate permeation altogether[70]. Future functional studies should therefore include measures of cation permeability in addition to standard kinetic and voltage dependence assays when considering variants affecting the pore domain.

Neurological and neurobehavioral phenotypes associated with the K1422E variant

As previously discussed, some properties of $Scn2a^{E/+}$ neurons are similar to those observed in Nav1.2 knockouts (reduced AP speed), while others are unique (calcium flux). As such, we would expect that $Scn2a^{E/+}$ mice might display some phenotypic overlap with *Scn2a* knockout models, in addition to some phenotypes that are distinct. EEG recording has been used to evaluate neurological phenotypes in $Scn2a^{+/-}$ mice with conflicting results. Ogiwara and colleagues (2018) described spike-and-wave discharges characteristic of absence epilepsy in $Scn2a^{+/-}$ mice, while other groups reported no observable seizures in $Scn2a^{+/-}$ mice[110,113]. However, this may be due to differences in age and/or strain that can affect spike-and-wave discharges and seizure susceptibility[103,163–166,169,171,175,215]. We performed video-EEG recordings in $Scn2a^{E/+}$ mice for a minimum of 96 h per animal, far longer than what has been reported for *Scn2a* knockouts, and observed rare spontaneous seizures with gross posterior cortical localization. To date, spontaneous seizures have not been described in any *Scn2a* knockout models. However, spontaneous seizures have been observed in *Scn2a* GoF models, such as $Scn2a^{A263V}$. This variant was shown to result in an increased persistent sodium current, and is associated with neonatal epilepsy in humans[127]. Frequent spontaneous seizures were reported in mice homozygous for the A263V variant, whereas heterozygotes exhibited infrequent non-convulsive seizures[128,129]. This is reminiscent of the infrequent non-convulsive seizures we observe in heterozygous $Scn2a^{E/+}$ mice, although we do not have viable homozygotes that can be observed for seizures.

In order to further probe seizure susceptibility in $Scn2a^{E/+}$ mice, we induced seizures using flurothyl. Although latency to the first seizure stage of MJ did not differ from WT, $Scn2a^{E/+}$ mice had longer latency to GTCS, suggesting resistance to seizure spread. This is somewhat unexpected given the localized spontaneous seizures observed using EEG. However, paradoxical induced seizure thresholds have been observed in other mouse epilepsy models and may reflect differential expression of Nav1.2 across cell types and across neuronal circuits involved in producing different types of seizures[216–218]. Axonal localization of Nav1.2 has been shown to be dictated by myelination, with expression being restricted to the proximal portion of the AIS in myelinated cells such as cortical projection neurons[55,60,62]. However, in unmyelinated neurons such as the locally projecting mossy fibers of dentate granule cells, Nav1.2 is expressed throughout the axonal compartment[65,66,211]. Interestingly, we also observed a reproducible non-unimodal distribution of GTCS latencies in $Scn2a^{E/+}$ females compared with WT. One possible explanation is a genotype-dependent interaction with fluctuating sex hormones and/or neurosteroids, which have previously been linked to altered seizure susceptibility in rodents[219–224].

Behavioral abnormalities reported in *Scn2a*$^{+/-}$ mice vary across research groups and may reflect differences in methodological practices (e.g. age or background strain), as well as inherent variability of behavioral data[118,119]. We observed lower anxiety-like behavior in *Scn2a*$^{E/+}$ mice across three exploration assays (zero maze, light–dark exploration, and open field) and an active marble burying task. Similar reductions in anxiety-like behavior and marble burying have been reported in *Scn2a*$^{+/-}$ mice by some groups, although the opposite effect has also been reported[58,111,112,117]. *Scn2a*$^{E/+}$ mice also displayed hyper-social behavior in a three-chamber assay, while inconsistent effects on social behavior have been reported in *Scn2a*$^{+/-}$ mice[112,114–116]. Although ASD is typically associated with social behavior deficits[121], hyper-social behaviors such as inappropriate social approach and enhanced direct social interaction have been reported in ASD-associated genetic mouse models including *Scn2a*[114,116,122,123]. This highlights the heterogeneity of ASD-associated phenotypes and the complexity of modeling human social behavior in animals. In particular, mouse social behavior is guided by olfaction and olfactory function must be considered when interpreting assay results. Direct assessment of olfaction in *Scn2a*$^{E/+}$ mice revealed intact discrimination for both social and non-social odors, but lower dishabituation to same-sex social odors compared with WT. This apparent contradiction with the hyper-social behavior observed in the three-chamber assay, which evaluates interactions with a target mouse rather than an odor-soaked cotton-swab, suggests that altered social behavior in *Scn2a*^{K1422E} mice occurs downstream of olfactory perception.

Bridging the gap: limitations, challenges and future directions

Here we present the *Scn2a*^{K1422E} mouse model, in which we demonstrate altered ion permeation through Nav1.2 in neurons for the first time. We also present a comprehensive characterization of neurological/neurobehavioral phenotypes in *Scn2a*$^{E/+}$ mice. A limitation of the current study is our ability to link changes in the intrinsic properties of neurons to changes in network excitability/connectivity, as well as to the observed neurobehavioral phenotypes. This makes it difficult to place the K1422E variant within the existing spectrum of *SCN2A*-associated NDD.

Functional annotation of *SCN2A* variants often reveals effects that span multiple aspects of channel function (e.g. voltage dependence, kinetics). These effects can be considered GoF or LoF with regard to individual channels, but the effect of a given variant of the intrinsic properties of neurons represents a complex summation of channel-level effects[35,71,82]. For example, the DEE-associated variants *SCN2A*-p.L1342P and p.S1336Y were both shown to have mixed effects on channel function, but were considered to be overall GoF with regard to neuronal excitability[82,83,101]. However, these variants have different effects on channel function than those we observed for K1422E. When considering where the K1422E variant may fall within the spectrum of *SCN2A*-related disorders, comparison to other pore-adjacent variants reveals additional complexities. The variant *SCN2A*-p.Q383E is associated with variably severe epilepsy phenotypes, and although it has yet to undergo thorough functional characterization, it is predicted to alter cation permeability similar to K1422E[91]. Other pore adjacent variants such as *SCN2A*-p.R379, p.R937 and p.T1420M are associated with ASD/ID phenotypes and result in partial or complete disruption of channel conductance[70]. Although more direct comparisons are warranted, the similarities in neurobehavioral phenotypes between the *Scn2a*^{K1422E} mouse model and heterozygous knockouts seem to suggest that the K1422E variant represents a functional hypomorph. However, unlike the heterozygous knockouts, *Scn2a*^{K1422E} mice have a seizure phenotype that may reflect the complex effects on ion permeation that are also present. The generation of additional mouse models for the variants discussed above would allow for more informative comparisons to the K1422E variant. Additional complicating factors in linking channel function to circuit/system-level phenotypes are developmentally regulated splicing that affect the properties of Nav1.2 and changes in subcellular distribution during myelination that affect the contribution of Nav1.2 to neuronal excitability[55,60–62,68,69]. Thus, future studies aimed at understanding the pathophysiological mechanisms of the K1422E variant will need to account for cell-type specific and developmentally regulated changes in the expression of Nav1.2. It should be noted that recurrent and inherited variants in *SCN2A* show wide phenotypic heterogeneity, even among individuals with the same variant. One such example is the variant Q383E, discussed above, which has been associated with phenotypes including self-limited seizures and Ohtahara syndrome within the same family[91]. This suggests that disease-modifying factors such as genetic background may also contribute to phenotype expressivity. We and others have shown that different genetic backgrounds across mouse strains can influence disease phenotypes, including seizure susceptibility[162,103,163–170]. Future studies will be aimed at investigating the role of modifying factors on phenotypic complexity in *Scn2a*^{K1422E} and may yield additional insights into the pathophysiological mechanisms of this complex variant.

Chapter 3. Evaluating the Interplay between Estrous Cyclicity and Induced Seizure Susceptibility in *Scn2a*^{K1422E} Mice

3.1 Introduction

It has been widely documented that women with epilepsy often show a cyclical pattern of altered seizure susceptibility during specific phases of the menstrual cycle[155–157]. This pattern of "catamenial epilepsy" is a neuroendocrine condition that affects between 25-75% of women with epilepsy[158]. Additionally, menstrual disorders are more common in women with epilepsy than in the general population[225]. The association between seizure susceptibility and the menstrual cycle can be attributed to fluctuations in hormones and corresponding changes in neurosteroid levels[147,148,156,159].

Rodent models have been used extensively to examine the relationship between the estrous (menstrual) cycle, steroid hormones, and seizure susceptibility. Many studies have used acute models of seizure induction such as chemoconvulsants like flurothyl which was described in the previous chapter[168,170,219,220,226–228]. Another approach to modeling catamenial epilepsy involves using hippocampal kindling in conjunction with exogenous administration of progesterone or gonadotropin followed by a withdrawal period to mimic the hormonal milieu associated with catamenial seizure exacerbation[148,221,223,229]. Still other studies have looked at endogenous fluctuations in seizure susceptibility across the estrous cycle in rodent models of chronic epilepsy such as systemic injection of kainic acid (KA), the intrahippocampal KA model of temporal lobe epilepsy, and the WAG/Rij rat model of absence epilepsy[224,230–232]. These studies reveal complex, sometimes contradictory effects of ovarian hormones and neurosteroids on seizure susceptibility.

In general, estradiol is normally proconvulsant and progesterone (along with its neurosteroid derivative allopregnalone) are anticonvulsive[147,148,160].

To date, the effects of the estrous cycle on seizure susceptibility have not been evaluated in the context of an epilepsy-associated genetic variant. In the previous chapter, we demonstrated that both male and female *Scn2a*$^{E/+}$ mice have a higher threshold for flurothyl-induced seizures compared to WT (**Figure 2.9E**). Within that initial data set, we also noted that the distribution of latencies to GTCS in *Scn2a*$^{E/+}$ females was non-normal, while latencies were normally distributed for all other groups (**Figure 2.9E**). This effect was subsequently replicated in two additional cohorts of *Scn2a*$^{E/+}$ and WT females (**Figure 2.9F**). Those data are replotted to highlight the distribution of each group in **Figure 3.1**. Woolley and colleagues showed previously that neither estradiol nor progesterone affect susceptibility to flurothyl-induced seizures in ovariectomized WT rats[219]. However, it is possible that the K1422E variant may affect sensitivity to ovarian hormones. The nuclear estrogen receptor alpha is a transcription factor that is activated by endogenous estrogens (e.g. estradiol) and has been shown to target *Scn2a* in sexually dimorphic brain regions[233]. Based on these findings, we hypothesize that the estrous cycle affects susceptibility to flurothyl-induced seizures in *Scn2a*$^{E/+}$ female mice.

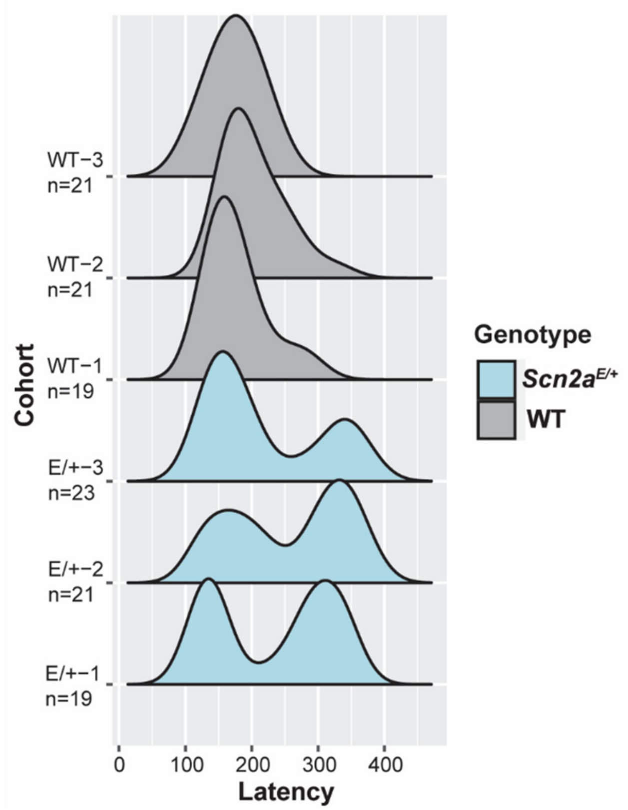

Figure 3.1 Non-normal distribution of latencies to flurothyl-induced GTCS in *Scn2a*$^{E/+}$ female mice.. Latency to first GTCS in WT and *Scn2a*$^{E+}$ female mice across multiple cohorts (data replotted from **Figure 2.9F**). Cohorts were evaluated at different times. Distribution of data from *Scn2a*$^{E/+}$ female is qualitatively abnormal in all three cohorts compared with cohort-matched WT controls

To test this hypothesis, we sought to answer two essential questions. First, we wanted to know if circulating sex hormones (i.e., the estrous cycle) are necessary to observe the non-normal distribution of flurothyl seizure thresholds in *Scn2a*$^{E/+}$ mice. Second, we wanted to know if flurothyl seizure thresholds are associated with a particular stage of the estrous cycle. Here, we examined flurothyl seizure thresholds in *Scn2a*$^{E/+}$ female mice that underwent ovariectomy or sham surgery and subsequent estrous cycle monitoring. We found that ovariectomy did not have an effect on the non-unimodal distribution of flurothyl seizure thresholds observed in *Scn2a*$^{E/+}$ mice. Additionally, flurothyl seizure thresholds were not associated with estrous cycle stage in mice that underwent sham surgery. However, we did find evidence of disrupted estrous cyclicity in non-surgerized *Scn2a*$^{E/+}$ mice. These data suggest that the estrous cycle does not significantly affect susceptibility to flurothyl-induced seizures in *Scn2a*$^{E/+}$ mice.

3.2 Materials and Methods

Mice

Female heterozygous *Scn2a*$^{E/+}$ and WT mice for experiments were obtained from the line *Scn2a*^{em1Kea} (MGI:6390565), which is maintained as an isogenic strain on C57BL/6J. Mice were maintained in a specific pathogen free (SPF) barrier facility with a 14 h light/10 h dark cycle and access to food and water ad libitum. All animal care and experimental procedures were approved by the Northwestern University Animal Care and Use Committees in accordance with the National Institutes of Health Guide for the Care and Use of Laboratory Animals. Principles outlined in the ARRIVE (Animal Research: Reporting of *in vivo* Experiments) guideline were considered when planning experiments[191].

Surgeries

Bilateral ovariectomy (OVX) or sham surgery was performed on female WT and *Scn2a*$^{E/+}$ mice at 5-6 weeks of age. All subjects were weighed prior to the start of surgery. For both surgeries, subjects were deeply anesthetized with a cocktail of ketamine and xylazine (100 mg/kg and 10 mg/kg, respectively) administered by intraperitoneal (IP) injection. Depth of anesthesia was evaluated by loss of response to reflex stimulation (toe pinch). For pre-operative analgesia, 20mg/kg meloxicam was administered by subcutaneous (SC) injection near the neck scruff. Next, ophthalmic ointment (Puralube; Dechra Veterinary Products, Overlan Park, KS, USA) was applied to both eyes using a sterile cotton swab in order to prevent ocular damage and drying. Then, the surgical site (dorsal surface, below ribs) was shaved using hair clippers and subjects were placed in a stereotaxic frame with a heating pad. Sterilization of the surgical site was accomplished with 3x alternating scrubs of 4% chlorohexidine gluconate solution (Hibiclens; Molnlycke Health Care LLC, Norcross, GA, USA) and 70% ethanol using sterile cotton swabs. Local anesthesia for the primary incision site was achieved by SC infiltration using 20 μL of 0.2% lidocaine. Following local anesthesia, a primary midline incision (1-2 cm) was made in the skin between the ribs and pelvis. Forceps and surgical scissors were used to cut fascia and separate skin from the body wall lateral to the spine in either direction. Next, an incision (0.5 cm) was made in the body wall between the musculature and ovarian fat pad. Forceps were used to exteriorize the ovarian fat pad via the body wall incision and the uterine horn and ovary were identified. For OVX, hemostatic forceps were used to induce a crush injury in the uterine horn below the ovary and the ovary was subsequently removed. The remainder of the ovarian fat pad and uterine horn was then re-internalized through the body wall incision. For sham surgeries, no crush injury was induced and the intact ovarian fat pad was re-internalized following identification of the ovary. For both surgeries, the body wall incision was repaired using 5-0 polydioxanone absorbable monofilament sutures (AD Surgical, Sunnyvale, CA, USA). The process from body wall incision to repair was then repeated on the opposite side. The primary midline incision was repaired using 4-0 polyamide 6 non-absorbable monofilament sutures (Ethicon LLC, San Lorenzo, Puerto Rico, USA). For post-operative analgesia, 1 mg/kg sustained release buprenorphine was administered by SC injection above the tail. To reverse the effects of anesthesia, 1 mg/kg atipamezole hydrochloride plus sterile saline was administered by SC injection near the tail. The amount of saline injected was calculated based on 20 mL/kg maximum SC injection volume (including all other SC injections). All surgically treated subjects were housed individually during recovery and estrous cycle monitoring.

Estrous cycle monitoring

Estrous cycle monitoring was performed using a vaginal cytology protocol as previously described[234]. Cycle monitoring was conducted from 0700 to 0800 daily. A 1x phosphate buffered saline (PBS) solution was prepared by diluting 5mL sterile 10x PBS (ThermoFisher) in 45 mL deionized water. Using a 20-200 μL pipette, 40 μL of 1x PBS solution was aspirated into a 200 μL pipette tip. To obtain a vaginal smear sample, the pipette tip was inserted approximately 0.2 cm into the vaginal canal and the solution was gently pipetted 1-3 times before being aspirated. Samples were then deposited on individual microscope slides (Cat. No. 22-178-277; Thermo Fisher) and covered with a microscope slide cover slip (Cat. No. 12-548-5MP; Thermo Fisher;). Vaginal cytology was assessed using a compound binocular light microscope with 4x and 10x magnification objectives (Olympus CX33 Biological Microscope) and representative images of each sample at 10x magnification were captured using an Apple iPhone 13 Pro (Camera app; 3x zoom) held up to the microscope eye piece. Estrous cycle stage was determined by evaluating the proportion of relevant cell types in a given sample as previously described[235–237]. The four stages of the mouse estrous cycle are defined as follows with representative images shown in **Figure 3.2**: proestrus (nucleated epithelial cells), estrus (cornified epithelial cells), metestrus (approximately 50% cornified epithelial cells and leukocytes) and diestrus (high density leukocytes). An additional stage, “unclear” was used to designate samples that contained a large amount of cellular debris, making stage determination difficult.

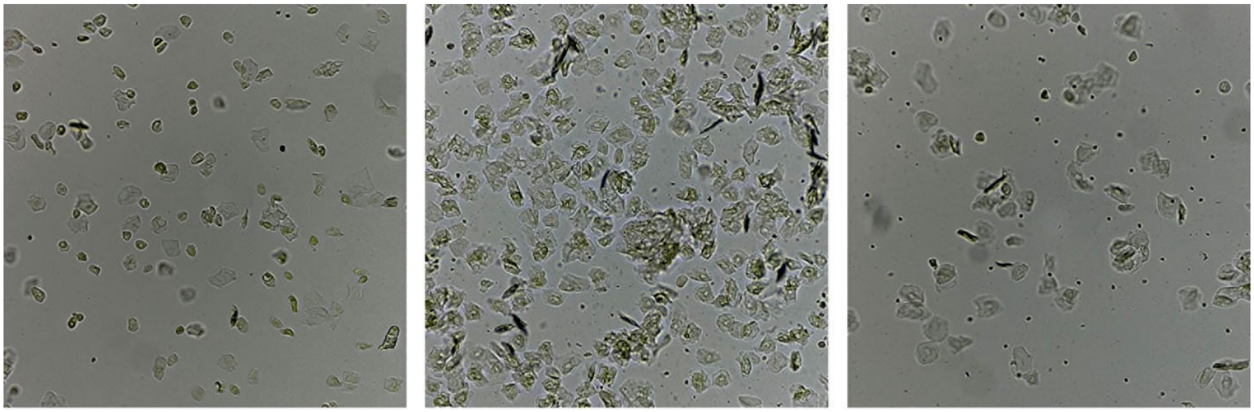

Proestrus Estrus Metestrus

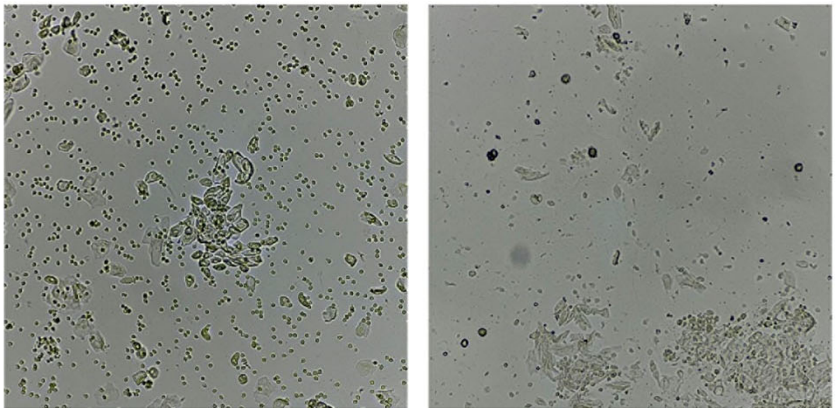

Diestrus Unclear

Figure 3.2 Estrous cycle monitoring in *Scn2a*$^{E/+}$ female mice. Representative images of unstained vaginal smear samples corresponding to different estrous cycle stages based on proportion of relevant cell types. Proestrus (nucleated epithelial cells), estrus (cornified epithelial cells), metestrus (approximately 50% cornified epithelial cells and leukocytes), diestrus (high density leukocytes), and unclear (cellular debris; difficult to score). Samples were visualized using light microscopy at 10x magnification. Images were captured using an Apple iPhone 13 Pro camera app at 3x zoom.

Cycle monitoring was performed in two cohorts of female WT and *Scn2a*$^{E/+}$ mice beginning at 5-8 weeks of age. The first cohort consisted of mice that underwent either OVX or sham surgery (n = 19–20 per genotype and treatment, blinded to treatment). Subjects were allowed 7-14 days to recover from surgery before daily estrous cycle monitoring was performed leading up to, and on the day of, flurothyl seizure induction (**Figure 3.3A**). Estrous cycle monitoring data was used to make blinded calls of surgical condition based on estrous cyclicity (i.e., cycle regularity). A subject was defined as having an irregular cycle if cycle length (average time to progress from one stage of estrus to the next) exceeded 7 days or if the subject spent more than 50% of time in any given stage[224,238]. A subject was blind called as having undergone OVX if it had an irregular cycle with a majority of samples determined to be "unclear" (**Figure 3.2**)[239]. A single subject was excluded from analyses due to being blind called as receiving a sham surgery despite actually receiving OVX. The second cohort consisted of consisted of non-surgerized mice ($n = 20–21$ per genotype). Daily estrous cycle monitoring was performed leading up to, and on the day of flurothyl seizure induction. Estrous cycle monitoring data was used to evaluate estrous cyclicity using the criteria defined above.

Flurothyl seizure induction

Flurothyl seizure induction was performed as described in **Chapter 2**. Seizure susceptibility was assessed in five cohorts of female WT and *Scn2a*$^{E/+}$ mice at 6-10 weeks of age. Latency to first GTCS was recorded. The mice from the first three cohorts ($n = 19–23$ per genotype and cohort) were evaluated previously as part of the initial characterization of *Scn2a*^{K1422E} mice as described in Echevarria-Cooper et al. (2022)[184] and in **Chapter 2** (**Figure 2.9F)**. Data from these three cohorts are replotted separately in **Figure 3.1** then collapsed across cohorts and presented as "WT Naïve" ($n = 61$) and "E/+ Naïve" ($n = 62$) in **Figure 3.3B.** Mice from these cohorts did not undergo estrous cycle monitoring. The fourth cohort consisted of mice that underwent either OVX or sham surgery ($n = 19–20$ per genotype and treatment). The fifth cohort consisted of unsurgerized mice ($n = 20–21$ per genotype). Mice from the fourth and fifth cohorts underwent estrous cycle monitoring prior to, and on the day of flurothyl seizure induction as described above.

Statistical analysis

Table 3.1 summarizes statistical tests used for all comparisons along with computed values. Distributions of latencies to flurothyl-induced GTCS were evaluated for unimodality/non-unimodality using the R packages 'diptest' and 'multimode' (RStudio 4.2.0) [240–242]. All other comparisons were performed as indicated below using GraphPad Prism (v 9.4.1).

Table 3.1 Statistical comparisons

Figure	Comparison	Test	Value	Post Hoc
3.3	WT Sham GTCS Distribution	Hartigan's Dip Test	p=0.4102	n/a
		Excess Mass Test	p=0.208	n/a
	WT OVX GTCS Distribution	Hartigan's Dip Test	p=0.8703	n/a
		Excess Mass Test	p=0.624	n/a
	WT Naïve GTCS Distribution	Hartigan's Dip Test	p=0.9935	n/a
		Excess Mass Test	p=0.986	n/a
	Scn2a$^{E/+}$ Sham GTCS Distribution	Hartigan's Dip Test	p=0.4102	n/a
		Excess Mass Test	p=0.188	n/a
	Scn2a$^{E/+}$ OVX GTCS Distribution	Hartigan's Dip Test	p=0.0479	n/a
		Excess Mass Test	p=0.02	n/a
	Scn2a$^{E/+}$ Naïve GTCS Distribution	Hartigan's Dip Test	p=0.0006	n/a
		Excess Mass Test	p<0.0001	n/a
3.4	Sham – Estrous Cycle Stage vs GTCS (**A**)	Two-way ANOVA	F(1,31)=1.552, p=0.2221 (Main Effect: Estrous Cycle Stage) F(1,31)=9.791, p=0.0038 (Main Effect: Genotype)	Sidak's
	Sham Estrous Cycle Regularity (**B**)	Fisher's Exact test	p=0.2003	n/a
3.5	Untreated – Estrous Cycle Stage vs GTCS (**A**)	Two-way ANOVA	F(1,32)=0.7885, p=0.3812 (Main Effect: Estrous Cycle Stage) F(1,32)=18.47, p=0.0002 (Main Effect: Genotype)	Sidak's
	Untreated Estrous Cycle Regularity (**B**)	Fisher's Exact test	p=0.0109	n/a

3.3 Results

Ovariectomy does not abolish non-unimodal distribution of flurothyl seizure thresholds in Scn2a$^{E/+}$ mice

To evaluate whether the estrous cycle is associated with flurothyl seizure thresholds in *Scn2a*$^{E/+}$ mice, we performed ovariectomy (OVX) or sham surgery. A schematic of the experimental design is shown in **Figure 3.3A**. After a recovery period of 7-14 days, we performed daily monitoring of the estrous cycle. Flurothyl was used to induce GTCS in WT and *Scn2a*$^{E/+}$ mice 17-24 days after surgery (7-9 weeks of age). Specifically, we wanted to compare the distribution of latencies to GTCS in surgically treated mice against historical data from untreated mice (**Figures 2.9F & 3.1**). In order to statistically evaluate distributions for unimodality/non-unimodality, we used Hartigan's *dip* test and the multimode test proposed by Ameijeiras-Alonso and colleagues[243,244]. Both of these analytical methods involve hypothesis testing in which unimodality represents the null hypothesis and a p-value of less than or equal to 0.05 is required to reject the null hypothesis. P-values for all groups are shown in **Table 3.1**. The historical data from untreated (naïve) *Scn2a*$^{E/+}$ females had a non-unimodal distribution, while historical data from naïve WT females had a unimodal distribution (**Figure 3.3B**). Surgically treated (OVX and sham) WT females also had unimodal distributions of latencies to GTCS similar to naïve controls (**Figure 3.3B**). Somewhat unexpectedly, OVX did not affect the distribution of latencies to GTCS in *Scn2a*$^{E/+}$ females (**Figure 3.3B**). The above data suggest that estrous cyclicity does not significantly contribute to flurothyl seizure thresholds in WT or *Scn2a*$^{E/+}$ mice. Interestingly, *Scn2a*$^{E/+}$ females that underwent sham surgery had a distribution that did not reach statistical significance for non-unimodality but is still qualitatively abnormal compared to WT controls (**Figure 3.3B**).

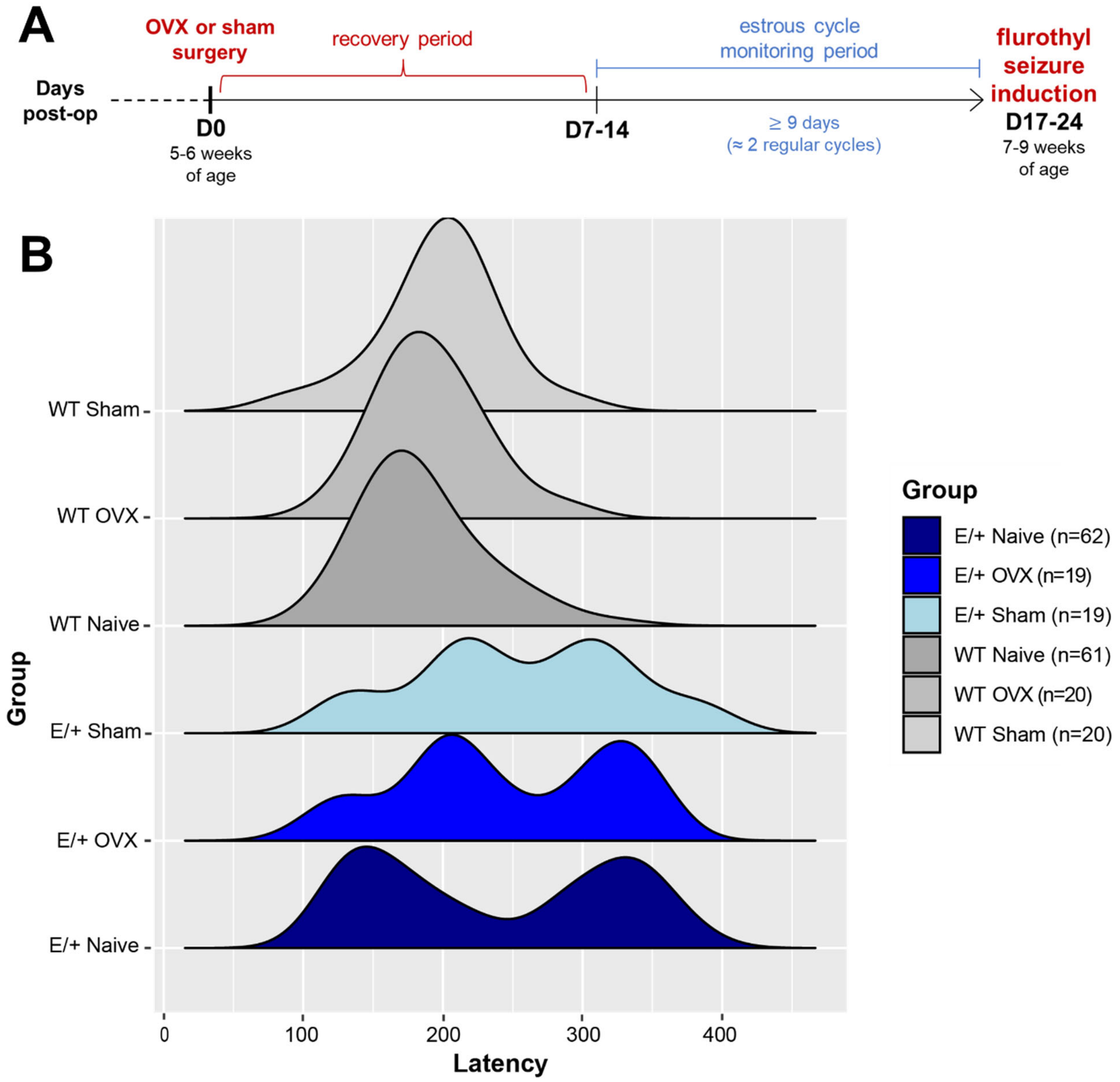

Figure 3.3 Ovariectomy does not abolish non-unimodal distribution of flurothyl-induced GTCS in *Scn2a*$^{E/+}$ female mice. (**A**) Schematic of experimental design for time points of surgery, estrous cycle monitoring and flurothyl seizure induction. Ovariectomy is abbreviated as OVX. (**B**) Latency to first GTCS in WT and *Scn2a*$^{E/+}$ female mice under different surgical conditions. Data from **Figure 3.1** were collapsed across cohorts and are presented as WT Naïve and E/+ Naïve. Distributions of latencies to GTCS were evaluated for unimodality/non-unimodality using hypothesis testing (**Table 3.1**) Data from naïve *Scn2a*$^{E/+}$ females had a non-unimodal distribution while naïve WT females had a unimodal distribution. WT females that underwent either OVX or sham surgery also had unimodal distributions. *Scn2a*$^{E/+}$ females that underwent OVX had a non-unimodal distribution similar to naïve controls. *Scn2a*$^{E/+}$ females that underwent sham surgery had a distribution that did not reach statistical significance for non-unimodality but is still qualitatively abnormal compared to WT controls.

Flurothyl seizure threshold is not associated with estrous cycle stage in Scn2a$^{E/+}$ mice

Estrous cycle monitoring in surgically treated mice served a dual purpose. First, it allowed us to evaluate the success of OVX versus sham surgeries. Blind calls of surgical condition based on estrous cycle monitoring were 100% accurate, with the exception of a single subject which was excluded. Second, it allowed us to evaluate whether flurothyl seizure threshold is associated with a particular stage of the estrous cycle in *Scn2a*$^{E/+}$ mice that underwent sham surgery. We grouped subjects based on the estrous cycle stage determined on the day of flurothyl seizure induction. For the purposes of analysis, we compared stages that are estradiol-dominant (proestrus and estrus) with diestrus (progesterone-dominant)[224,245]. Two-way ANOVA comparing average latency to GTCS in sham surgery *Scn2a*$^{E/+}$ females and WT controls showed only a significant main effect of genotype, but no significant effect of estrus cycle stage or genotype-by-stage interaction (**Table 3.1**) Although the genotype effect appears to be driven by the pro/estrus groups such that *Scn2a*$^{E/+}$ females had a higher threshold for GTCS (271.0 ± 67.0 s) compared to WT (201.3 ± 45.2 s; **Figure 3.4A**), the WT diestrus group was underrepresented (n = 4). The observed genotype effect is also in agreement with our previous findings on flurothyl seizure threshold in *Scn2a*$^{E/+}$ mice (**Figure 2.9F**) This data, along with lack of observable effects in the OVX condition, provides convergent evidence that estrous cyclicity does not significantly affect flurothyl seizure thresholds in *Scn2a*$^{E/+}$ mice

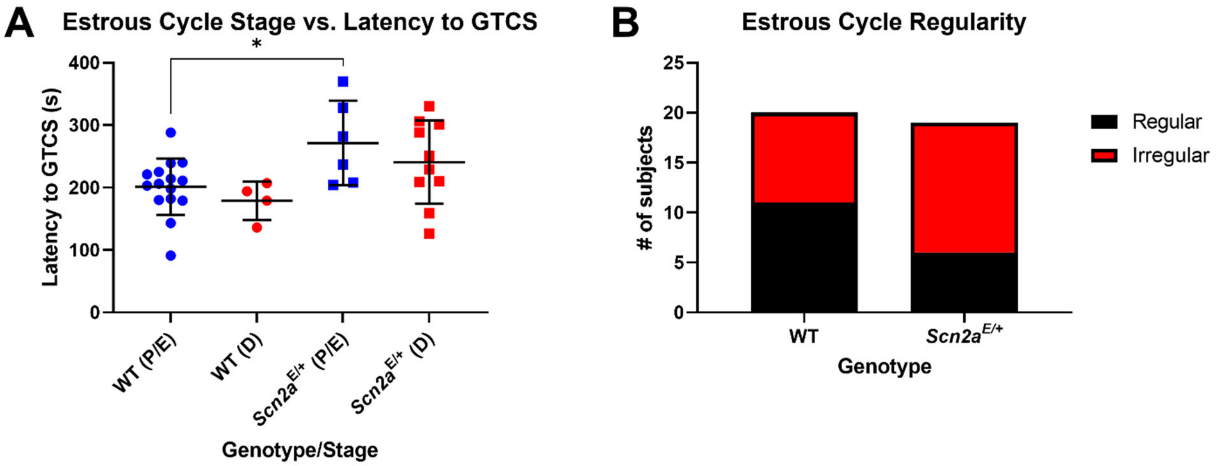

Figure 3.4 Latency to flurothyl-induced GTCS is not associated with estrous cycle stage in sham ovariectomized *Scn2a*$^{E/+}$ female mice. (**A**) Latency to first flurothyl-induced GTCS in sham ovariectomized WT and *Scn2a*$^{E/+}$ female mice during pro/estrus (abbreviated P/E) or diestrus (abbreviated D). Two-way ANOVA showed only a significant main effect of genotype [*F*(1,31)=9.791, *P*=0.0038]. Post hoc-analysis showed that *Scn2a*$^{E/+}$ females in pro/estrus had an elevated threshold for GTCS compared to stage-matched WT controls (WT: 201.3 ± 45.2 s, *Scn2a*$^{E/+}$: 271.0 ± 67.0 s, $^{*}P$=0.0268; Sidak's post-hoc test). Symbols represent individual mice, horizontal lines represent mean, and error bars represent SD; *n* = 4-15/stage/genotype. (**B**) Number of sham ovariectomized WT and *Scn2a*$^{E/+}$ female mice (*n* = 19-20 per genotype) with regular vs irregular estrous cycles (WT: 45.00% irregular, *Scn2a*$^{E/+}$:68.42% irregular). Proportion of mice with irregular cyclicity was not significantly different between genotypes (*P*=0.2003, Fisher's Exact test). Irregular cyclicity was defined as having a cycle length (average time to progress from one stage of estrus to the next) that exceeded 7 days as spending more than 50% of the monitoring period in any given stage.

Disrupted estrous cyclicity in Scn2a$^{E/+}$ *mice*

As part of our estrous cycle monitoring in surgically treated mice, we evaluated overall cycle regularity. A subject was defined as having an irregular cycle if cycle length exceeded 7 days or if the subject spent more than 50% of time in any given stage[224,238]. We noted that a proportion of both WT and *Scn2a*$^{E/+}$ sham ovariectomized mice had irregular cyclicity (WT: 45.00%, *Scn2a*$^{E/+}$: 68.42%), likely as a result of surgical intervention (**Figure 3.4B**). In order to exclude the confounding factor of surgical trauma, we wanted to evaluate whether flurothyl seizure threshold is associated with a particular stage of the estrous cycle in an additional cohort of untreated mice. Similar to what was seen in sham surgery mice (**Figure 3.4A**), two-way ANOVA comparing average latency to GTCS in untreated *Scn2a*$^{E/+}$ females and WT controls showed only a significant main effect of genotype but no significant effect of estrus cycle stage or genotype-by-stage interaction (**Table 3.1**). Again, this effect appears to be driven by the pro/estrus groups such that *Scn2a*$^{E/+}$ females had a higher threshold for GTCS (290.0 ± 67.0 s) compared to WT (185.5 ± 30.6 s; **Figure 3.5A**). Interestingly, while the proportion of sham surgery mice with irregular cyclicity was not significantly different between genotypes (**Figure 3.4B**), the proportion of untreated *Scn2a*$^{E/+}$ females with irregular cyclicity was significantly greater than WT (WT: 19.05%, *Scn2a*$^{E/+}$: 60.00% irregular; *P*=0.0109, Fisher's exact test; **Figure 3.5B**). This suggests that disrupted estrous cyclicity may be causally associated with the K1422E variant.

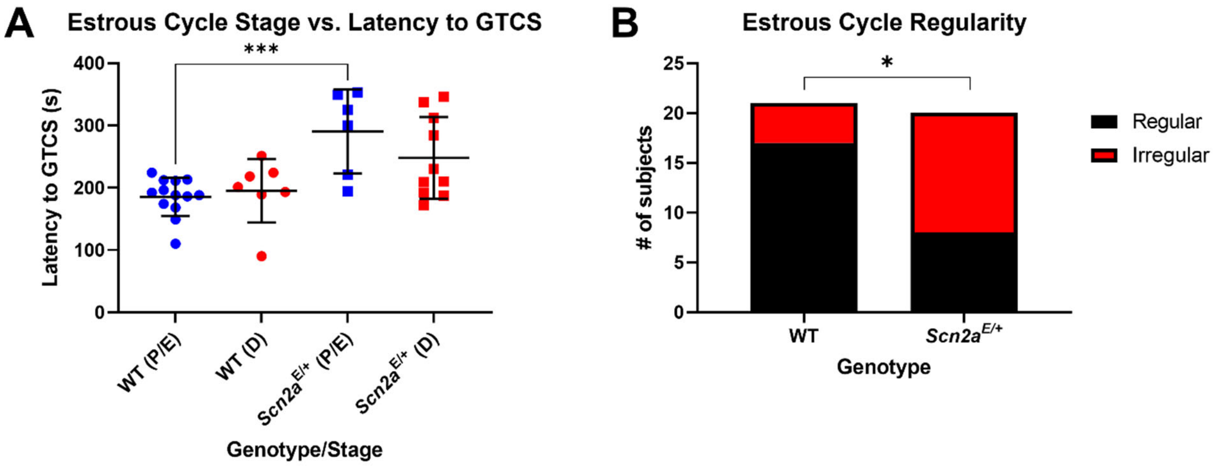

Figure 3.5 Disrupted estrous cyclicity in untreated *Scn2a*$^{E/+}$ female mice. (**A**) Latency to first flurothyl-induced GTCS in untreated WT and *Scn2a*$^{E/+}$ female mice during pro/estrus (abbreviated P/E) or diestrus (abbreviated D). Two-way ANOVA showed only a significant main effect of genotype [$F(1,32)=18.47$, $P=0.0002$]. Post hoc-analysis showed that *Scn2a*$^{E/+}$ females in pro/estrus had an elevated threshold for GTCS compared to stage-matched WT controls (WT: 185.5 ± 30.6 s, *Scn2a*$^{E/+}$: 290.0 ± 67.0 s, $^{***}P=0.0006$; Sidak's post-hoc test). Symbols represent individual mice, horizontal lines represent mean, and error bars represent SD; n = 6-13/stage/genotype. (**B**) Number of sham untreated WT and *Scn2a*$^{E/+}$ female mice (n = 20-21 per genotype) with regular vs irregular estrous cycles (WT: 19.05% irregular, *Scn2a*$^{E/+}$:60.00% irregular). Proportion of *Scn2a*$^{E/+}$ female mice with irregular cyclicity was significantly greater compared to WT ($^{*}P=0.0109$, Fisher's Exact test). Irregular cyclicity was defined as having a cycle length (average time to progress from one stage of estrus to the next) that exceeded 7 days as spending more than 50% of the monitoring period in any given stage.

3.4 Discussion

Epilepsy represents a diverse group of conditions for which differences between males and females can vary across different types of seizures[143,147–149]. The neurobiological basis for sex differences in seizure susceptibility is likewise varied and the subject of ongoing research[147,148]. One area that has received significant attention involves the reciprocal relationship between sex hormones and seizure susceptibility. In women with catamenial epilepsy, cyclical patterns of altered seizure susceptibility have been associated with the menstrual cycle and corresponding fluctuations in ovarian hormones and neurosteroids[147,148,155,156,159,225]. Correspondingly, epilepsy is associated with an increased risk for reproductive endocrine diorders[147,159,225]. Rodent models have been used to look at the effect of both exogenous and endogenous hormones in the context of acute seizure induction and chronic epilepsy[147,148]. Here, we focused on susceptibility to flurothyl-induced seizures in our *Scn2a* mouse model of the epilepsy-associated variant K1422E.We hypothesized that the estrous cycle affects susceptibility to flurothyl-induced seizures in *Scn2a*$^{E/+}$ female mice. We showed that historical data of flurothyl seizure thresholds in *Scn2a*$^{E/+}$ female mice have a statistically significant non-unimodal distribution. We further evaluated susceptibility to flurothyl-induced seizures in the context of ovariectomy or sham surgery. Ovariectomy did not abolish the non-unimodal distribution of flurothyl seizure susceptibility in *Scn2a*$^{E/+}$ female mice. Additionally, flurothyl seizure thresholds were not associated with estrous cycle stage in mice that underwent sham surgery. However, we did find evidence of disrupted estrous cyclicity in untreated *Scn2a*$^{E/+}$ mice. These data suggest that variation in *Scn2a*$^{E/+}$ flurothyl seizure threshold is not significantly influenced by the estrous cycle and, by extension, fluctuations in ovarian hormones.

Limitations and alternative explanations

Many studies evaluating the influence of ovarian hormones on seizure susceptibility use ovariectomized rodents treated with a variety of hormone replacement regimens that can make it difficult to compare results across different studies[220]. In this study we asked the relatively simple question of whether circulating sex hormones are *necessary* to observe the reproducible, non-unimodal distribution of flurothyl seizure threshold seen in *Scn2a*$^{E/+}$ female mice. We reasoned that if circulating sex hormones were affecting flurothyl-seizure threshold, then removing said hormones via ovariectomy would collapse the non-unimodal distribution observed in *Scn2a*$^{E/+}$ females such that it would appear more similar to the distributions observed in WT females or

Scn2a$^{E/+}$ males. Contrary to our hypothesis, *Scn2a*$^{E/+}$ females that underwent OVX had a non-unimodal distribution similar to naïve controls (**Figure 3.3B**). This suggests that estrous cyclicity does not significantly contribute to flurothyl seizure thresholds in *Scn2a*$^{E/+}$ mice. We also included a sham surgery group in our study to control for possible confounding effects of surgical trauma versus the effect of removing circulating hormones. We reasoned that sham treated mice would recapitulate the distribution of flurothyl seizures thresholds observed in historical data from naïve mice. Interestingly, *Scn2a*$^{E/+}$ females that underwent sham surgery had a distribution that did not reach statistical significance for non-unimodality (**Figure 3.3B**). The fact that we saw an effect in our surgical control group (sham) but not in our primary treatment group (OVX) is difficult to interpret. One possible explanation is that our experimental groups ($n = 19$–20 per genotype and treatment) were underpowered compared to historical data ($n = 61$–62 per genotype). Another possible explanation is that disrupted cyclicity in the sham surgery groups diminished the resolving power of our statistical comparisons

One overall limitation of the ovariectomy approach is that while it addresses the necessity of circulating sex hormones for the genotype specific effect on flurothyl seizure threshold, it does not clarify the influence of specific hormones at endogenous levels. Thus, we used estrous cycle monitoring to evaluate whether flurothyl seizure threshold is associated with a particular stage of the estrous cycle in mice that underwent sham surgery. We grouped subjects based on the estrous cycle stage determined on the day of flurothyl seizure induction. The reason for this approach was to maximize the number of subjects undergoing seizure induction on the same day under identical conditions. However, this resulted in unequal and likely underpowered group numbers corresponding to different stages. An alternative approach to filling out group numbers would be to do seizure induction when subjects reach particular estrous cycle stages. This limitation in mind, we found that genotype, but not estrous cycle stage had a significant effect on latency to flurothyl-induced GTCS (**Table 3.1 & Figure 3.3A**). This genotype effect recapitulates our previous findings on flurothyl seizure threshold in *Scn2a*$^{E/+}$ mice (**Figure 2.9F**). From our estrous cycle monitoring data, we also noted that a non-zero proportion of both WT and *Scn2a*$^{E/+}$ sham surgery mice had irregular estrous cycles (**Figure 3.3B**). This observation, along with the unexpected distribution of flurothyl seizure thresholds in *Scn2a*$^{E/+}$ sham surgery mice mentioned previously, suggests a potentially confounding effect of surgical intervention. To address this potential limitation, we repeated estrous cycle monitoring and flurothyl seizure induction in an additional cohort of untreated mice and found only an effect of genotype similar what was seen in sham surgery mice (**Figure 3.4A**). However, unlike in the sham surgery condition, the proportion of untreated *Scn2a*$^{E/+}$ females with irregular cyclicity was significantly greater than WT (**Figure 3.4B**). This disruption of the estrous cycle is similar to what has been observed in other rodent models of epilepsy[230,238,246,247].

Together, the above results provide evidence to refute our stated hypothesis that the estrous cycle influences flurothyl seizure thresholds in *Scn2a*$^{E/+}$ female mice. Though suggestive, this does not fully rule out the influence of sex hormones per se. Our ovariectomy approach removed the influence of sex hormones produced by the ovaries, but sex hormones have also been shown to be synthesized locally in the brain and can be converted to other neurosteroids[148,248,249]. Furthermore, sex hormones can act via genomic and non-genomic mechanisms in the brain, and the timescale of these mechanisms may not have been adequately captured by our approach[250–253]. Other neurobiological mechanisms apart from the acute influence of sex hormones have been proposed to address sex differences in seizure susceptibility[147]. In the case of flurothyl seizure threshold in *Scn2a*$^{E/+}$ mice, any proposed mechanism would have to account for why the distribution of seizure thresholds in uniquely non-unimodal in *Scn2a*$^{E/+}$ females. One possibility is that variation in one or more modifier genes confers sex-specific protection to females such that there is an increased threshold for phenotypic penetrance of the K1422E variant. This is similar to a hypothesis that has been proposed to explain the "female protective effect" in ASD[144,151–153]. Another possibility is that female mice are differentially exposed to androgens *in utero* based on their intrauterine position relative to male siblings[254]. Androgen exposure in *in utero* is known to mediate early brain development and could influence seizure susceptibility in differentially exposed females[147,154]. Although the question of flurothyl-induced seizure susceptibility remains unanswered, the current study revealed disruption of the estrous cycle in untreated *Scn2a*$^{E/+}$ mice. To our knowledge, this is the first demonstration of disrupted estrous cyclicity in a mouse model of an epilepsy-associated genetic variant, particularly *SCN2A*-related NDD. This work serves as a reminder of the importance of investigating sex-differences to the field of genetic epilepsies and NDD and to the broader field of neuroscience.

Chapter 4. Strain-Dependent Effects on Neurobehavioral and Seizure Phenotypes in *Scn2a*^{K1422E} Mice

4.1 Introduction

A growing body of literature has been dedicated to cataloging disease-causing *SCN2A* variants based on their association with distinct biophysical defects in channel function. Missense variants resulting in a GoF have been associated with DEE phenotypes while missense variants and nonsense variants resulting in a LoF have been associated with ASD/ID[70,71,74,81,82]. Although the biophysical properties of mutant channels likely contribute to phenotype expressivity, recurrent and inherited variants in *SCN2A* show wide phenotypic heterogeneity, even among individuals with the same variant[70,71,91]. This suggests that other factors interact with *SCN2A* variants to influence neuropathological phenotypes. It is becoming increasingly evident that background genetic variation (i.e., modifiers) can affect the phenotypic properties of presumed "monogenic" disorders, but this can be difficult to study in the context of rare diseases with small patient populations [21,22,24–28].

Inbred populations (strains) of research animals are a double-edged sword when it comes to modeling disease. On the one hand, the isogenic nature of these animals makes them attractive for use as biological replicates in transgenic experiments[161]. One the other hand, the genetic background of particular strains may interact with the variant gene of interest in a way that compromises analysis of disease-related phenotypes[162]. However, these properties can be leveraged to study the effect of genetic modifiers in animal models of disease. Accordingly, different genetic backgrounds across rodent strains have been shown to influence disease-related phenotypes, including seizure susceptibility[103,162–170]. For example, it has been demonstrated that genetic background dramatically influences the epilepsy phenotype described in the *Scn2a*^{Q54} mouse model. *Scn2a*^{Q54} mice on a C57BL/6J background (abbreviated as B6 going forward) displayed adult-onset seizures and a mild survival deficit (>75% survival at 6 months) compared to WT mice on the same background. Meanwhile, *Scn2a*^{Q54} mice on a mixed [B6 × SJL] F1 background displayed juvenile-onset seizures and a more severe survival deficit (25% survival at 6 months) compared to mutant animals on a pure B6 background[103,163]. Studies on the effect of genetic background on seizure susceptibility can serve as the basis for identification of epilepsy modifier loci and genes using both classical genetic mapping strategies and a candidate gene approach[163,169,176–183]. This, in turn, can enhance our understanding of disease mechanisms and support the development of targeted therapeutic strategies.

In **Chapter 2**, we showed that *Scn2a*$^{E/+}$ mice on the B6 background exhibit NDD-related phenotypes, including alterations in anxiety-like behavior and seizure susceptibility. Given the demonstrated effects of genetic background in other epilepsy models like *Scn2a*^{Q54}, we wanted to know if background strain affects phenotype severity in the *Scn2a*^{K1422E} mouse model. To address this question, we crossed *Scn2a*$^{E/+}$ males on the B6 background to inbred DBA/2J (D2) females to generate F1 [D2×B6] hybrid offspring (abbreviated as F1D2 going forward). It has been shown previously that the D2 strain exhibits a high rate of spontaneous spike-wave discharges associated with behavioral arrest and increased susceptibility to induced seizures[171–175]. We evaluated anxiety-like behavior and seizure susceptibility in WT and *Scn2a*$^{E/+}$ mice on the F1D2 background compared to mice on the B6 background. Convergent evidence from neurobehavioral assays demonstrates reduced anxiety-like behavior in *Scn2a*$^{E/+}$ mice compared to WT and further suggests that this effect is more pronounced on the B6 background compared to the F1D2 background. F1D2.*Scn2a*$^{E/+}$ mice also exhibited rare spontaneous seizures similar to those seen previously in B6.*Scn2a*$^{E/+}$ mice (**Figure 2.9A & B**). Following administration of the chemoconvulsant kainic acid (KA), *Scn2a*$^{E/+}$ mice showed reduced susceptibility to seizure generalization but increased risk of lethality, with variation based on strain and sex. These data suggest that background strain does affect phenotype severity in the *Scn2a*^{K1422E} mouse model.

4.2 Materials and Methods

Mice

The line *Scn2a*^{em1Kea} (MGI:6390565), is maintained as an isogenic strain on C57BL/6J (abbreviated as B6). Male and female mice obtained from this line for experiments will be referred to as B6.*Scn2a*$^{E/+}$ and B6.WT going forward. B6. *Scn2a*$^{E/+}$ males were crossed to inbred DBA/2J females (abbreviated as D2; Jackson Labs, #000671, Bar Harbor, ME) to generate F1 [D2×B6] hybrid offspring. Male and female mice obtained from this cross for experiments will be referred to as F1D2.*Scn2a*$^{E/+}$ and F1D2.WT going forward. All animal care and experimental procedures were approved by the Northwestern University Animal Care and Use Committees in accordance with the National Institutes of Health Guide for the Care and Use of Laboratory Animals. Principles outlined in the ARRIVE (Animal Research: Reporting of *in vivo* Experiments) guideline were considered when planning experiments[191].

Neurobehavioral assays

B6 and F1D2 WT and *Scn2a*$^{E/+}$ mice of both sexes were tested at 8-12 weeks of age. Male and female mice were tested on separate days. For all experiments, mice were acclimated in the behavior suite with white noise for 1 h prior to behavioral testing. At the end of each procedure, mice were placed into their home cage with their original littermates. Behavioral testing was performed by experimenters blinded to genotype. The same cohort of mice was evaluated first in the zero maze and then in the open field, with a two-day interval between assays. For all measures male and females were considered separately. Statistical comparisons between groups were made using ordinary two-way ANOVA with Sidak's post-hoc comparisons (**Table 4.1**)

Zero maze

Mice were evaluated for anxiety-related behavior in an elevated zero maze. The maze consists of an annular platform (diameter 46 cm; elevation 50 cm) that is divided into equally sized quadrants, alternating between open and enclosed (wall height 17 cm). This configuration lacks the ambiguous center region associated with the elevated plus maze[197]. Individual mice were placed near an enclosed arm of the maze and allowed to freely explore for 5 min. Limelight software (Actimetrics, Wilmette, IL, USA) was used to video record each trial. Ethovison XT software (Noldus, Leesberg, VA, USA) was used to track the position of the mouse, and calculate distance traveled, mean velocity and time spent in closed or open arms ($n = 6$–14 per strain, genotype, and sex). Trials where mice exited the maze were excluded from analysis. Exclusions by group were as follows: B6.*Scn2a*$^{E/+}$ males – 7, B6.*Scn2a*$^{E/+}$ females – 5, F1D2.*Scn2a*$^{E/+}$ males – 2, all other groups – 0.

Open field

Mice were evaluated for baseline activity and anxiety-related behavior in an open field. Individual mice were placed in the center of an open field arena (46 × 46 cm) and allowed to freely explore for 30 min. Limelight software was used to video record each trial. Ethovison XT software was used to track the position of the mouse, and calculate total distance traveled, mean velocity and time spent in the periphery (9 cm from wall) and center (28 × 28 cm) ($n = 9$–15 per strain, genotype, and sex).

Video-EEG monitoring

Male and female F1D2.WT and F1D2.*Scn2a*$^{E/+}$ mice were implanted with prefabricated 3-channel EEG headmounts (Pinnacle Technology, Lawrence, KS, USA) at 4 weeks of age. Briefly, mice were anesthetized with ketamine/xylazine and place in a stereotaxic frame. Headmounts with four stainless steel screws that serve as cortical surface electrodes were affixed to the skull with glass ionomer cement. Anterior screw electrodes were 0.5–1 mm anterior to bregma and 1 mm lateral from the midline. Posterior screws were 4.5–5 mm posterior to bregma and 1 mm lateral from the midline. EEG1 represents recordings from right posterior to left posterior (interelectrode distance ≈ 2 mm). EEG2 represents recordings from right anterior to left posterior (interelectrode distance ≈ 5 mm). The left anterior screw served as the ground connection. Following at least 48 h of recovery, tethered EEG and video data were continuously collected from freely moving mice with Sirenia acquisition software (Pinnacle Technology) using a sampling rate of 400 Hz as previously described[196]. Between 168-240 h of EEG data were acquired from each subject (F1D2.WT: $n = 9$ mice, 4-5 weeks of age; F1D2.*Scn2a*$^{E/+}$: $n = 14$ mice, 4–7 weeks of age)]. Raw data was notch filtered with a 1 Hz window around 60 and 120 Hz prior to analysis. Video-EEG records were manually reviewed with Sirenia software, MATLAB (MathWorks, Natick, MA, USA) and EEGLAB (Swartz Center for Computational Neuroscience, CA, USA) by three independent reviewers blinded to genotype. Spontaneous seizures were defined as isolated events with an amplitude of ≥3 times baseline, duration of ≥10 s and that show evolution in power and amplitude. Data from five subjects with high baseline artifact or faulty connections were excluded from analysis.

Kainic Acid seizure induction

Susceptibility to seizures induced by the chemoconvulsant kainic acid (abbreviated as KA, Cat #0222, Tocris Bioscience, Minneapolis, MN) was assessed in B6 and F1D2 WT and *Scn2a*$^{E/+}$ mice of both sexes at 5-6 weeks of age. KA dissolved in saline to a working concentration of 2.5 mg/mL was administered by IP injection (25 mg/kg). Mice were placed in clean cages and video recorded (side view) for 2 hours. Videos were scored offline by two reviewers blinded to genotype using a modified Racine scale[255] (1- behavioral arrest; 2- forelimb and/or Straub tail, facial automatisms; 3- automatisms, including repetitive scratching, circling, forelimb clonus without falling; 4- forelimb clonus with rearing and/or falling, barrel roll; 5- repetition of stage 4; 6- generalized tonic-clonic seizure, wild running and/or jumping; 7- death). Latency to the first occurrence of each stage and the highest seizure stage reached within 5-minute bins were recorded ($n = 12$-21 per strain, genotype, and sex). Statistical comparisons of latency to stage 3, stage 6, and stage 7 were made by log-rank Mantel-Cox time to event analysis. Relevant pairwise comparisons between groups are indicated in **Table 4.1** (GraphPad Prism).

Table 4.1 Statistical comparisons

Figure	Comparison	Test	Value	Post Hoc
3.1	Male Zero Maze (**A**)	Two-way ANOVA	F(1,37)=47.46, p<0.0001 (Main Effect: Strain F(1,37)=9.877, p=0.0033 (Main Effect: Genotype)	Sidak's
	Female Zero Maze (**A**)	Two-way ANOVA	F(1,40)=23.26, p<0.0001 (Strain × Genotype) F(1,40)=242.4, p<0.0001 (Main Effect: Strain) F(1,40)=74.02, p<0.0001 (Main Effect: Genotype)	Sidak's
	Male Open Field (**B**)	Two-way ANOVA	F(1,45)=13.52, p=0.0006 (Strain × Genotype) F(1,45)=7.189, p=0.0102 (Main Effect: Strain)	Sidak's
	Female Open Field (**B**)	Two-way ANOVA	F(1,43)=19.61, p<0.0001 (Main Effect: Strain)	Sidak's
3.4	KA stage 3 – B6 E/+ SEX (**A**)	Log-rank Mantel-Cox test	p=0.0073	n/a
	KA stage 3 – F1D2 Male GENOTYPE (**A**)	Log-rank Mantel-Cox test	p=0.0240	n/a
	KA stage 6 – B6 E/+ SEX (**B**)	Log-rank Mantel-Cox test	p=0.0107	n/a
	KA stage 6 – B6 Male GENOTYPE (**B**)	Log-rank Mantel-Cox test	p=0.0003	n/a
	KA stage 6 – F1D2 Male GENOTYPE (**B**)	Log-rank Mantel-Cox test	p<0.0001	n/a
	KA stage 6 – F1D2 Female GENOTYPE (**B**)	Log-rank Mantel-Cox test	p<0.0001	n/a
	KA stage 6 – E/+ Female STRAIN (**B**)	Log-rank Mantel-Cox test	p=0.0008	n/a
	KA stage 7 (lethality) – B6 E/+ SEX (**C**)	Log-rank Mantel-Cox test	p=0.0077	n/a
	KA stage 7 (lethality) – B6 Male GENOTYPE(**C**)	Log-rank Mantel-Cox test	p=0.0467	n/a
	KA stage 7 (lethality) – WT Male STRAIN (**C**)	Log-rank Mantel-Cox test	p=0.0001	n/a
	KA stage 7 (lethality) – WT Female STRAIN (**C**)	Log-rank Mantel-Cox test	p=0.0002	n/a
	KA stage 7 (lethality) – E/+ Female STRAIN (**C**)	Log-rank Mantel-Cox test	p=0.0006	n/a

4.3 Results

Strain-dependent effects on anxiety-related behavior in Scn2a$^{E/+}$ mice.

To evaluate whether background strain affects phenotype severity in the *Scn2a*^{K1422E} mouse model, we crossed B6.*Scn2a*$^{E/+}$ males to inbred D2 females to produce F1D2 hybrid offspring. We used the zero maze and open field assays described in **Chapter 2** to assess anxiety-related behavior in adult *Scn2a*$^{E/+}$ and WT mice on the B6 and F1D2 backgrounds. In the zero maze assay, time spent in the open versus closed arms of the maze was measured (**Figure 4.1A**). Two-way ANOVA comparing males showed significant main effects of strain and genotype, but no significant strain-by-genotype interaction (**Table 4.1**). Both WT and *Scn2a*$^{E/+}$ males on the B6 background spent significantly more time in the open arms compared to males on the F1D2 background (**Figure 4.1A**). The genotype effect appears to be driven by the F1D2 group such that F1D2.*Scn2a*$^{E/+}$ males spent significantly more time (12.3 ± 10.67%) in the open arms compared to F1D2.WT males (0.7 ± 1.0%, **Figure 4.1A**). Two-way ANOVA comparing females also showed significant main effects of strain and genotype, and a significant strain-by-genotype interaction (**Table 4.1**). Both WT and *Scn2a*$^{E/+}$ females on the B6 background spent significantly more time in the open arms compared to females on the F1D2 background (**Figure 4.1A**). Also, B6 and F1D2.*Scn2a*$^{E/+}$ females spent significantly more time in the open arms compared to WT females. However, the difference between WT and *Scn2a*$^{E/+}$ females on the B6 background (23.8%) was larger than the difference between WT and *Scn2a*$^{E/+}$ females on the F1D2 background (6.7%, **Figure 4.1A**). The observed genotype effect seen in both males and females is also in agreement with our previous findings on anxiety-related behavior in B6.*Scn2a*$^{E/+}$mice (**Figure 2.10**).

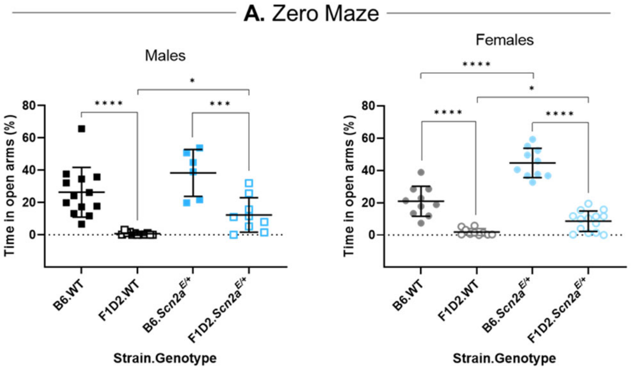

A. Zero Maze

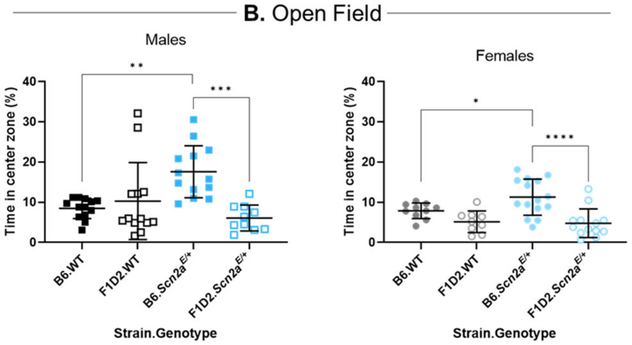

B. Open Field

Figure 4.1 Strain-dependent effects on anxiety-related behavior in *Scn2a*$^{E/+}$ mice. (**A**) Percent time spent in the open arms of a zero maze apparatus in B6 and F1D2 *Scn2a*$^{E/+}$ mice compared to WT. Males and females were analyzed separately (*n* = 6-13/strain/genotype for males, *n* = 10–14/strain/genotype for females). Two-way ANOVA comparing males showed significant main effects of strain [*F*(1,37)=47.46, *P*<0.0001] and genotype [*F*(1,37)=9.877, *P*=0.0033]. Both *Scn2a*$^{E/+}$ and WT males on the B6 background spent more time in the open arms compared to mice on the F1D2 background (*Scn2a*$^{E/+}$: ****P*=0.0002, WT: *****P*<0.0001; Sidak's post-hoc test). However, only F1D2.*Scn2a*$^{E/+}$ males spent significantly more time in the open arms compared to WT mice (F1D2.WT: 0.7 ± 1.0%, F1D2.*Scn2a*$^{E/+}$: 12.3 ± 10.7%, **P*=0.0483; Sidak's post hoc-test). Two-way ANOVA comparing females showed significant main effects of strain [*F*(1,40)=242.4, *P*<0.0001] and genotype [*F*(1,40)=74.02, *P*<0.0001] and a significant interaction [*F*(1,40)=23.26, *P*<0.0001]. Both *Scn2a*$^{E/+}$ and WT females on the B6 background spent more time in the open arms compared to mice on the F1D2 background (*Scn2a*$^{E/+}$: *****P*<0.0001, WT: *****P*<0.0001; Sidak's post-hoc test). B6 and F1D2.*Scn2a*$^{E/+}$ females also spent more time in the open arms compared to WT mice (B6: *****P*<0.0001, F1D2: **P*=0.0163; Sidak's post-hoc test). (**B**) Percent time spent in the center zone of an open field in B6 and F1D2.*Scn2a*$^{E/+}$ mice compared to WT. Males and females were analyzed separately (*n* =10-13/strain/genotype for males, *n* = 9–15/strain/genotype for females). Two-way ANOVA comparing males showed a significant main effect of strain [*F*(1,45)=7.189, *P*=0.0102] and a significant interaction between strain and genotype [*F*(1,45)=13.52, *P*=0.0006]. Only *Scn2a*$^{E/+}$ males on the B6 background spent significantly more time in the center zone compared to mice on the F1D2 background (F1D2.*Scn2a*$^{E/+}$: 6.1 ± 3.2%, B6.*Scn2a*$^{E/+}$: 17.6 ± 6.5%, ****P*=0.0002; Sidak's post-hoc test). B6.*Scn2a*$^{E/+}$ males also spent significantly more time in the center zone compared to WT mice (B6.WT: 8.5 ± 2.5%, B6.*Scn2a*$^{E/+}$: 17.6 ± 6.5%, ***P*=0.0012; Sidak's post-hoc test). Two-way ANOVA comparing females showed only a significant main effect of strain [*F*(1,39)=14.14, *P*<0.0006]. Only *Scn2a*$^{E/+}$ females on the B6 background spent significantly more time in the center zone compared to mice on the F1D2 background (F1D2.*Scn2a*$^{E/+}$: 4.77 ± 3.56%, B6.*Scn2a*$^{E/+}$: 11.27 ± 4.47%, *****P*<0.0001; Sidak's post-hoc test). B6.*Scn2a*$^{E/+}$ females also spent significantly more time in the center zone compared to WT mice (B6.WT: 7.9 ± 1.9%, B6.*Scn2a*$^{E/+}$: 11.3 ± 4.5%, **P*=0.044; Sidak's post-hoc test) For **A & B**, symbols represent individual mice; lines and error bars represent mean ± SD.

In the open field assay, time spent in the exposed center zone of the apparatus versus the periphery was measured (**Figure 4.1B**). Two-way ANOVA comparing males showed a significant main effect of strain (but not genotype) and a significant strain-by-genotype interaction (**Table 4.1**). The strain effect appears to be driven by the *Scn2a*$^{E/+}$ group such that *Scn2a*$^{E/+}$ males on the B6 background spent significantly more time (17.6 ± 6.5%) in the center zone compared to *Scn2a*$^{E/+}$ males on the F1D2 background (6.1 ± 3.3%, **Figure 4.1B**). Furthermore, the interaction appears to be driven by the B6 group such that B6 *Scn2a*$^{E/+}$ males spent significantly more time (17.6 ± 6.5%) in the center zone compared to B6.WT males (8.5 ± 2.5%, **Figure 4.1B**). Two-way ANOVA comparing females showed a significant main effect of strain but no significant effect of genotype or strain-by-genotype interaction (**Table 4.1**). The strain effect appears to be driven by the *Scn2a*$^{E/+}$ group such that *Scn2a*$^{E/+}$ females on the B6 background spent significantly more time (11.3 ± 4.5%) in the center zone compared to *Scn2a*$^{E/+}$ females on the F1D2 background (4.8 ± 3.6%, **Figure 4.1B**). Similar to males, B6 *Scn2a*$^{E/+}$ females spent significantly more time (11.3 ± 4.5%) in the center zone compared to B6.WT females (7.9 ± 1.9%, **Figure 4.1B**). The data from these two neurobehavioral assays are generally in agreement with our previous findings that the K1422E variant is associated with lower anxiety-related behavior in mice (**Figure 2.10**). In addition, main effects of strain and strain-by-genotype interactions show that the effect of the K1422E variant is more pronounced on the B6 background, thus providing evidence that background strain affects phenotype severity in the *Scn2a*^{K1422E} mouse model.

F1D2.Scn2a$^{E/+}$ *mice exhibit rare spontaneous seizures.*

In **Chapter 2**, we demonstrated that B6.*Scn2a*$^{E/+}$ mice exhibit EEG abnormalities, including spontaneous seizures (**Figure 2.9A & B**). These spontaneous seizures were rare and difficult to observe due to a lack of an obvious behavioral component. Therefore, we wanted to know whether background strain affects spontaneous seizures in *Scn2a*$^{E/+}$ mice. Previous studies have shown that the D2 strain exhibits a high rate of spontaneous spike-wave discharges associated with behavioral arrest and increased susceptibility to induced seizures[171–175]. To evaluate F1D2.*Scn2a*$^{E/+}$ mice for spontaneous seizures, juvenile (4 weeks) mice were implanted with EEG headmounts for video-EEG monitoring which occurred from 4-7 weeks of age. F1D2.*Scn2a*$^{E/+}$ mice exhibited spontaneous seizures during wake and sleep (**Figure 4.2**) The seizure shown in **Figure 4.2** coincided with wild running and abrupt behavioral arrest, whereas seizures in B6.*Scn2a*$^{E/+}$ mice occurred only during sleep without a behavioral component. Similar to mice on the B6 background, spontaneous seizures were observed in a minority of F1D2.*Scn2a*$^{E/+}$ mice. However, similar events were never observed in F1D2.WT mice. The infrequent nature of spontaneous seizures in F1D2.*Scn2a*$^{E/+}$ mice precludes a formal analysis of strain-dependence with regard to this particular phenotype. At least qualitatively, it can be said that spontaneous seizures are not more frequent in F1D2.*Scn2a*$^{E/+}$ mice compared to B6 *Scn2a*$^{E/+}$ mice. However, data from these two strains provide convergent evidence that the K1422E variant is associated with rare spontaneous seizures in mice.

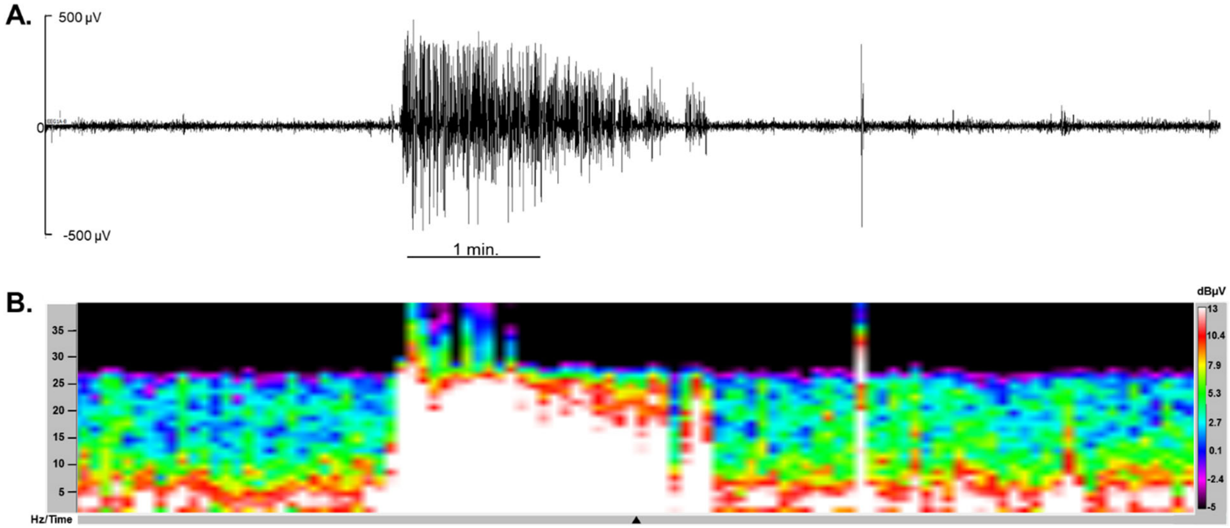

Figure 4.2 Spontaneous seizures in F1D2.*Scn2a*$^{E/+}$ mice. (**A**) Representative 9 min epoch of EEG from F1D2.*Scn2a*$^{E/+}$ mice. Signal corresponds to channel 1 (right posterior-left posterior). A localized seizure occurred as an abrupt onset of activity that evolves in amplitude and frequency for ~2 min before abruptly terminating with return to typical active background. Seizure activity coincided with wild running and abrupt behavioral arrest. (**B**) Spectral density array corresponding to the seizure in (A) showing elevated power (white; dBµV) across the 1-25 Hz frequency range at the time of discharge.

Susceptibility to KA-induced seizures varies by sex and strain in Scn2a$^{E/+}$ *mice.*

In the preceding data chapters, we demonstrated that B6.*Scn2a*$^{E/+}$ mice have a higher threshold for flurothyl-induced seizures compared to WT (**Figures 2.9E, 3.4A, 3.5B)**. We wanted to know if similar effects could be observed using a different method of seizure induction. We also wanted to know whether background strain affects susceptibility to induced seizures in *Scn2a*$^{E/+}$ mice. Previous studies have shown that D2 and commercially available B6D2F1/J mice (analogous to our F1D2 mice obtained by breeding) show greater susceptibility to KA-induced seizures compared to B6 mice[172,173,256]. Therefore, we evaluated susceptibility to KA-induced seizures in *Scn2a*$^{E/+}$ and WT mice on the B6 and F1D2 backgrounds at 5-6 weeks of age. Seizure severity following KA administration was assessed over a 2 hour period using a modified Racine scale[255] and the highest stage reached within 5 minute bins was recorded (**Figure 4.3**).

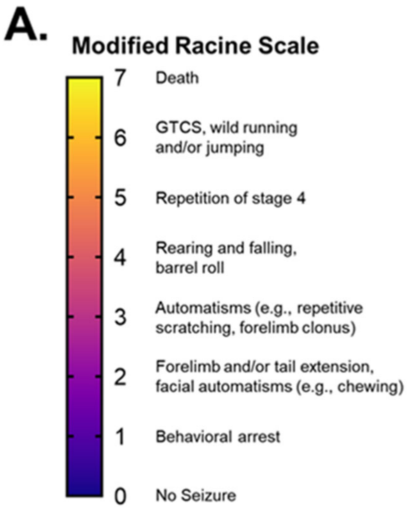

Figure 4.3 Kainic acid seizure induction in B6 and F1D2.*Scn2a*$^{E/+}$ mice. (**A**) Modified Racine scale for scoring seizure severity in mice following KA administration. (**B**) Heat maps depicting individual level seizure severity for mice on the B6 background organized by genotype and sex ($n = 12$-19 per group). Highest seizure stage reached per 5 min time bin was recorded and represented as in (A). Y axis represents individual mice and X axis represents 5 min time bins. A white square with an 'X' indicates a 5 min time bin where the subject was obscured during video recording and seizure severity could not be determined. (**C**) Heat maps depicting individual level seizure severity for mice on the F1D2 background organized by genotype and sex ($n = 12$-21 per group). Highest seizure stage reached per 5 min time bin was recorded and represented as in (A). Y axis represents individual mice and X axis represents 5 min time bins.

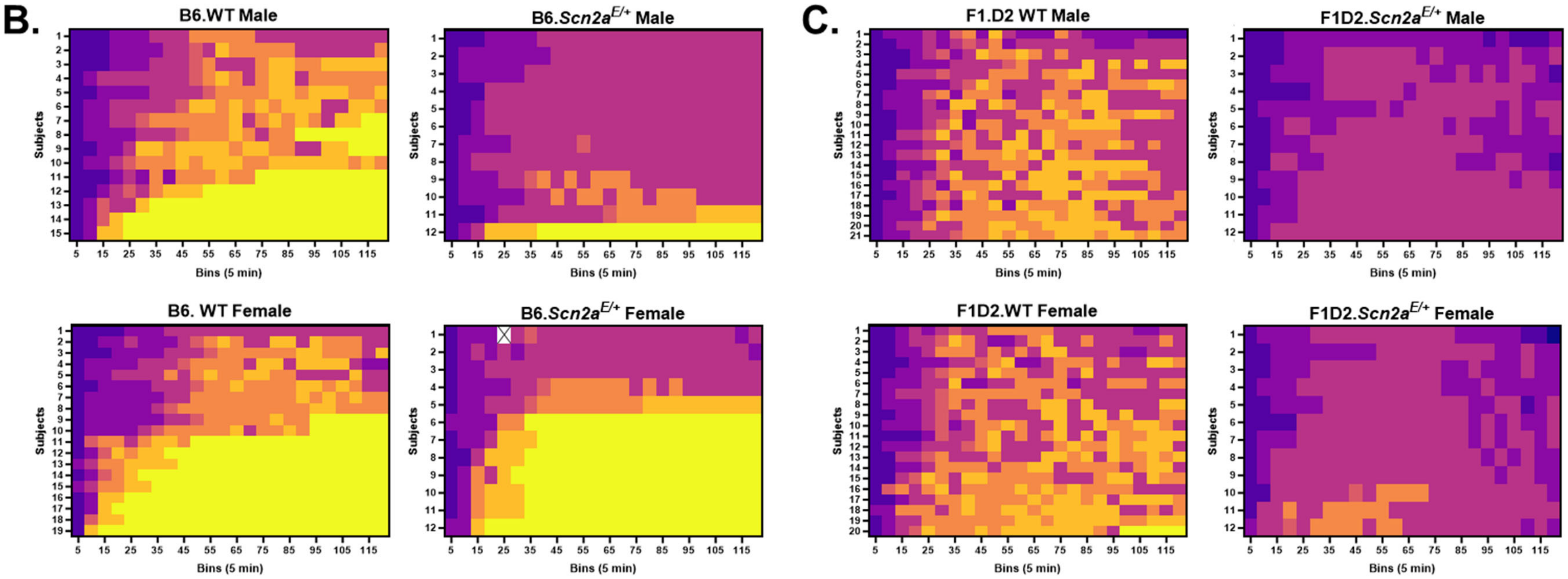

The heatmaps shown in **Figure 4.3 B & C** provide a visual summary of seizure severity following KA administration for all subjects organized by genotype, strain, and sex. For the purposes of quantitative analysis, we also measured latency to first occurrence of each Racine stage and made pairwise comparisons between groups using by log-rank Mantel-Cox time to event analysis (**Table 4.1 & Figure 4.4**). Stages 1-3 of the modified Racine scale represent increasingly severe focal seizure events (**Figure 4.3A**). Most subjects reached stage 3 with no significant differences in latency between groups (**Figure 4.4A**). However, only 91.67% of F1D2.*Scn2a*$^{E/+}$ males reached stage 3 with a median time to event of 25.08 min compared to 100% of F1D2.WT males with a median time to event of 20.95 min (**Figure 4.4A**). This suggests that the K1422E variant is associated with lower KA-seizure susceptibility in F1D2 male mice. We also noted that although 100% of B6.*Scn2a*$^{E/+}$ males and females reached stage 3, median time to event was longer for males (22.80 min) compared to females (15.04 min; **Table 4.1**). This suggests a potential sex difference in KA-seizure susceptibility that is both genotype and strain dependent. Stages 4-6 of the modified Racine scale represent increasingly severe generalized seizure events (**Figure 4.3A**) Significantly fewer B6 and F1D2.*Scn2a*$^{\mathrm{E/+}}$ males reached stage 6 compared to strain-matched WT controls. 16.67% of B6.*Scn2a*$^{E/+}$ males and 0% of F1D2.*Scn2a*$^{\mathrm{E/+}}$ males reached stage 6, while 93.33% of B6.WT males and 95.24% of F1D2.WT males reached stage 6 (**Figure 4.4B**). In addition, significantly fewer F1D2.*Scn2a*$^{\mathrm{E/+}}$ females (0%) reached stage 6 compared to F1D2.WT females (90%; **Figure 4.4B**). These data provide further evidence to suggest that the K1422E variant is associated with lower KA-seizure susceptibility. We also noted that significantly fewer B6.*Scn2a*$^{E/+}$ males (16.67%) reached stage 6 compared to B6.*Scn2a*$^{E/+}$ females (66.67%; **Table 4.1**). Similar to what was observed for latency to stage 3, this suggests a potential sex difference in KA-seizure susceptibility that is both genotype and strain dependent. Stage 7 of the modified

Racine scale represents death **(Figure 4.3A)**. Most subjects on the F1D2 background did not die following KA administration, with no significant differences based on genotype or sex (**Figure 4.3C**). Significantly fewer B6.*Scn2a*$^{E/+}$ males (16.67%) died following KA administration compared to B6.WT males (53.33%; **Figure 4.4C**). In addition, significantly fewer F1D2.WT males (0%) died following KA administration compared to B6.WT males (53.33%; **Figure 4.4C**). As previously noted, a majority of B6.*Scn2a*$^{E/+}$ males do not reach stage 6 (i.e. do not have a GTCS), and therefore would not be expected to die as a result of KA-induced status epilepticus. If we consider group lethality as percentage of subjects that reach stage 6, then 100% of B6.*Scn2a*$^{E/+}$ males died following KA administration compared to 57.14% of B6.WT males (data not shown). For females, significantly fewer F1D2.WT and *Scn2a*$^{E/+}$ mice died following KA administration compared to genotype-matched B6 controls. 5% of F1D2.WT females and 0% of F1D2.*Scn2a*$^{E/+}$ females died, while 57.89% of B6.WT females and 66.67% of B6.*Scn2a*$^{E/+}$ females died (**Figure 4.4C**). However, if we consider group lethality as percentage of subjects that reach stage 6, then 100% of B6.*Scn2a*$^{E/+}$ females died following KA administration compared to 61.11% of B6.WT females (data not shown). Furthermore, we noted that significantly fewer B6.*Scn2a*$^{E/+}$ males die compared to B6.*Scn2a*$^{E/+}$ females when lethality is considered as a percentage of all subjects (**Table 4.1**). However, this effect is not observed if we consider group lethality as percentage of subjects that reach stage 6, as B6.*Scn2a*$^{E/+}$ males and females both exhibit 100% lethality. These data provide evidence to suggest that the K1422E variant is potentially associated with increased risk of death following KA-induced GTCS in mice on the B6 background. Across the three stages analyzed, the results demonstrate that genotype, sex, and strain interact to influence KA seizure susceptibility.

Figure 4.4 (caption on next page)

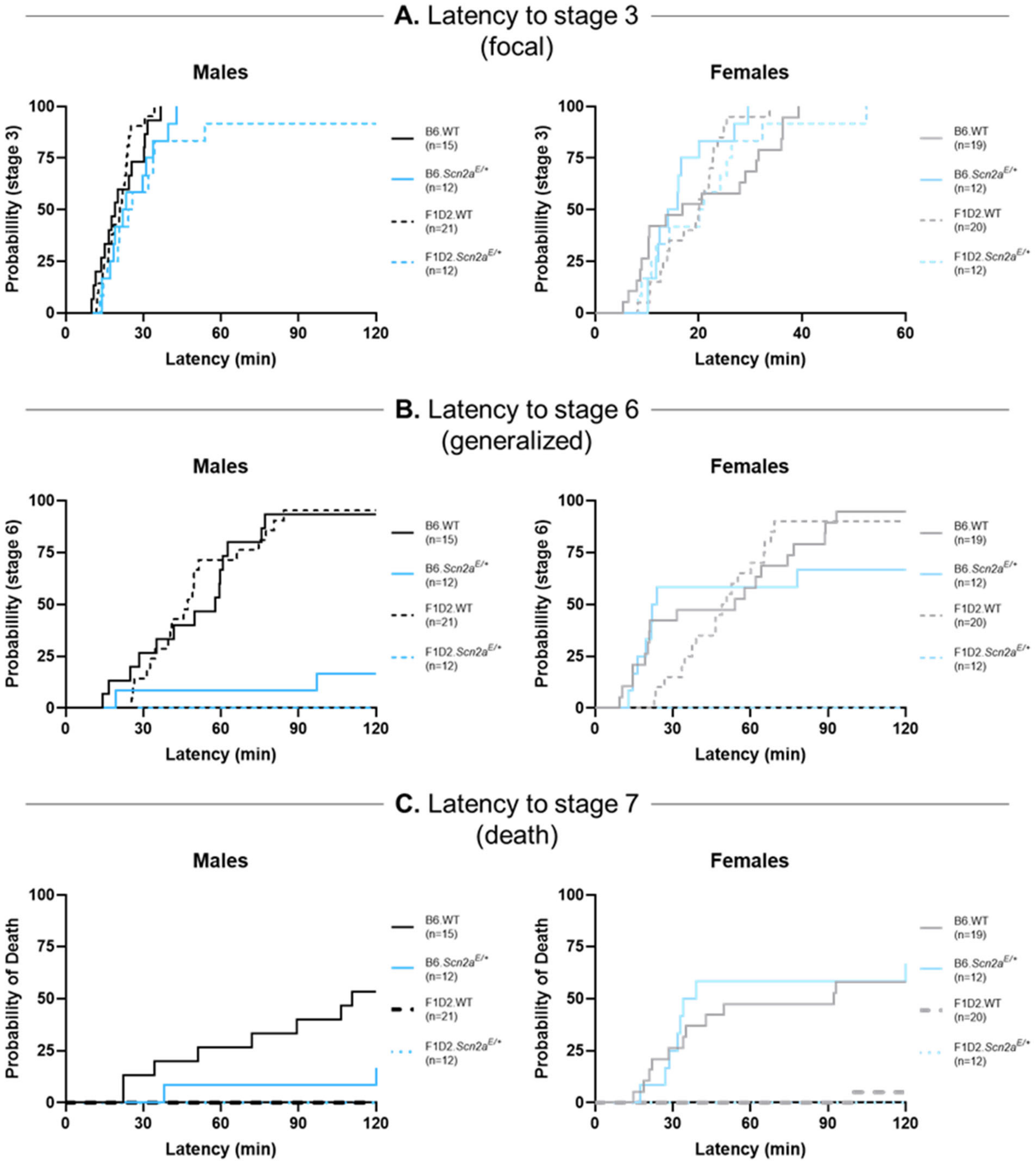

Figure 4.4 Strain-dependent effects on susceptibility to kainic acid-induced seizures in *Scn2a*$^{E/+}$ mice. Image on previous page. (**A**) Latency to first occurrence of modified Racine stage 3 (focal automatisms) in B6 and F1D2 *Scn2a*$^{E/+}$ mice compared to WT. Colored lines represent percentage of subjects that reached stage 3 over time. Most subjects reached stage 3 with no significant differences in latency between genotypes or strains. However, 91.67% of F1D2.*Scn2a*$^{E/+}$ males (median time: 25.08 min) reached stage 3 compared to 100% of F1D2.WT males (median time: 20.95 min, *P*=0.0240; Log-rank Mantel-Cox test). Males and females are displayed separately but were still compared. 100% of B6.*Scn2a*$^{E/+}$ males and females reached stage 3. However, the median time to stage 3 was longer for B6.*Scn2a*$^{E/+}$ males (B6.*Scn2a*$^{E/+}$ females: 15.04 min, B6.*Scn2a*$^{E/+}$ males: 22.80 min, *P*=0.0073; Log-rank Mantel-Cox test). (**B**) Latency to first occurrence of modified Racine stage 6 (GTCS) in B6 and F1D2.*Scn2a*$^{E/+}$ mice compared to WT. Colored lines represent percentage of subjects that reached stage 6 over time. Fewer B6 and F1D2.*Scn2a*$^{E/+}$ males reached stage 6 compared to WT males (B6: *P*<0.0001, F1D2: *P*<0.0001; Log-rank Mantel-Cox test). For females, fewer F1D2.*Scn2a*$^{E/+}$ mice reached stage 6 compared to WT (F1D2.WT: 90%, F1D2.*Scn2a*$^{E/+}$: 0%, *P*<0.0001; Log-rank Mantel-Cox test). Also, fewer *Scn2a*$^{E/+}$ females on the F1D2 background reached stage 6 compared to *Scn2a*$^{E/+}$ females on the B6 background. (B6.*Scn2a*$^{E/+}$: 66.67%, F1D2.*Scn2a*$^{E/+}$: 0%, *P*=0.0008; Log-rank Mantel-Cox test). Males and females are displayed separately but were still compared. 16.67% of B6.*Scn2a*$^{E/+}$ males reached stage 6 compared to 66.67% of B6.*Scn2a*$^{E/+}$ females (*P*=0.0008; Log-rank Mantel-Cox test). (**C**) Latency to modified Racine stage 7 (death) in B6 and F1D2 *Scn2a*$^{E/+}$ mice compared to WT. Colored lines represent percent mortality over time. B6.*Scn2a*$^{E/+}$ males had lower mortality compared to WT males (B6.WT: 53.33%, B6.*Scn2a*$^{E/+}$: 16.67%, *P*=0.0467; Log-rank Mantel-Cox test). Also, WT males on the F1D2 background had lower mortality compared to WT males on the B6 background (B6.WT: 53.33%, F1D2.WT: 0%, *P*=0.0467; Log-rank Mantel-Cox test). For females, both *Scn2a*$^{E/+}$ and WT mice on the F1D2 background had lower mortality compared to the B6 background (*Scn2a*$^{E/+}$: *P*=0.0006, WT: *P*=0.0002; Log-rank Mantel-Cox test). Males and females are displayed separately but were still compared. 16.67% of B6.*Scn2a*$^{E/+}$ males reached stage 6 compared to 66.67% of B6.*Scn2a*$^{E/+}$ females (*P*=0.0077; Log-rank Mantel-Cox test).

4.4 Discussion

Recurrent and inherited variants in *SCN2A* show wide phenotypic heterogeneity among individuals[70,71,91]. This suggests that factors beyond the primary pathogenic mechanism of a given variant may contribute to the presence of/variation in a particular phenotype. These factors might include genetic, epigenetic, and environmental modifiers. The effects of genetic modifiers on rare driver mutations are difficult to study in the context of rare diseases with small patient populations[26]. However, it is possible to leverage stable genetic differences between inbred populations of research animals in order to systematically study the effect of genetic background in animal models of disease. As such, different genetic backgrounds across rodent strains have been shown to influence disease-related phenotypes, including seizure susceptibility[103,162–170]. Here, we evaluated whether background strain affects phenotype severity in our *Scn2a*^{K1422E} mouse model by comparing WT and *Scn2a*$^{E/+}$mice on the F1D2 background to mice on the pure B6 background. Convergent evidence from neurobehavioral assays demonstrates reduced anxiety-like behavior in *Scn2a*$^{E/+}$ mice compared to WT and further suggests that this effect is more pronounced on the B6 background compared to the F1D2 background. F1D2.*Scn2a*$^{E/+}$ mice also exhibited rare spontaneous seizures, although not at a higher rate than B6.*Scn2a*$^{E/+}$ mice. Following administration of the chemoconvulsant kainic acid (KA), *Scn2a*$^{E/+}$ mice showed reduced susceptibility to seizure generalization but increased risk of lethality, with variation based on strain and sex. These data suggest that background strain does affect phenotype severity in the *Scn2a*^{K1422E} mouse model.

Limitations and alternative explanations

Many of the phenotypes we observed during our initial characterization of B6.*Scn2a*$^{E/+}$ mice, such as lower anxiety-like behavior and lower susceptibility to induced seizures, were statistically significant and reproducible **(Chapters 2 & 3)**. However, spontaneous seizures were rare and difficult to observe in B6.*Scn2a*$^{E/+}$ mice (**Figure 2.9A & B**). In order to evaluate the effect of genetic background on phenotypes associated with the K1422E variant, we considered alternative mouse strains with endogenous differences in these phenotypes when compared to B6. Relative to B6, D2 mice show higher anxiety-like behavior and higher seizure susceptability[162,171–175]. Despite these endogenous differences between these two strains, it can be difficult to predict how their respective genetic backgrounds might interact with the pathogenic mechanisms of the K1422E variant to influence disease-related phenotypes. It is similarly difficult to predict how an F1 hybrid background, which is heterozygous for B6 and D2 alleles at all autosomal loci, might interact with the K1422E variant. Thus, our approach to investigating whether background strain affects phenotype severity in the *Scn2a*^{K1422E} mouse model is largely exploratory in nature. We showed previously that B6.*Scn2a*$^{E/+}$mice exhibit lower anxiety-like behavior across multiple exploration assays (**Figure 2.10A-C**). Despite using two of the same assays in the current study (zero maze and open field), the results from this cohort of B6.WT and B6.*Scn2a*$^{E/+}$ mice cannot be directly compared to the previous cohort due to differences in age, experimenters, and time between assays. That in mind, the K1422E variant was associated with lower anxiety-like behavior in the current study, similar to what was shown in **Chapter 2**. In addition, the B6 background was associated with lower anxiety like behavior relative to F1D2. Furthermore, strain by genotype interactions observed in both assays suggest that lower anxiety-like behavior associated with the K1422E variant is more pronounced on the B6 background (**Figure 4.1**). One limitation of these experiments is that some groups are underpowered relative to others ($n = 6$ vs 15). Therefore, these results should be considered preliminary evidence that background strain affects anxiety-like behavior in *Scn2a*$^{E/+}$ mice.

In **Chapter 2** we described rare spontaneous seizures without an observable behavioral component in B6.*Scn2a*$^{E/+}$ mice. Here, we describe similar seizures in a preliminary cohort of F1D2.*Scn2a*$^{E/+}$ mice (**Figure 4.2**). However, some seizures in F1D2 mice were associated with wild running and behavioral arrest, raising the possibility that seizures are more severe in F1D2 mice compared to B6. Unfortunately, this phenotype shows low penetrance across both strains with only some individuals exhibiting seizures at a rate that precludes quantitative analysis. One possible alternative would be to use kindling to promote more frequent spontaneous seizures in *Scn2a*$^{E/+}$ mice[206,257–259]. However, kindled seizures may be etiologically distinct from spontaneous seizures. Furthermore, converging evidence of resistance to chemically-induced seizures in *Scn2a*$^{E/+}$ mice suggests that kindling may be technically challenging to achieve. At minimum, the observation of spontaneous seizures in F1D2.*Scn2a*$^{E/+}$ mice validates our previous findings in B6 mice. The infrequent nature of spontaneous seizures in B6.*Scn2a*$^{E/+}$mice motivated our investigation of susceptibility to acute, chemically-induced seizures. In **Chapters 2 & 3**, multiple cohorts of B6.*Scn2a*$^{E/+}$ mice were shown to exhibit lower susceptibility to flurothyl-induced GTCS. When considering how to approach the question of background strain and seizure susceptibility in the *Scn2a*^{K1422E} mouse model, we elected to use an alternative seizure induction paradigm (KA). This would allow us to address whether seizure resistance was inducer-specific, in addition to exploring the effects of background strain. We used a modified Racine scale to score seizure severity following KA administration (**Figure 4.3**)[255]. The scale was modified to best reflect the discrete stages of increasingly severe seizures that we observed under our experimental conditions. That said, minor differences in scale can make it difficult to compare findings from different groups[173,256]. It should also be noted that previous studies have shown that pure D2 strain and F1D2 hybrids are more susceptible to KA-induced seizures compared to the B6 strain[172,173,256]. While we did not include pure D2 mice for comparison, the B6 and F1D2.WT mice included in our study did not recapitulate this effect (**Figure 4.4**). However, this could be due to methodological differences across studies including method of KA administration. In addition, the F1D2 hybrids used in previous studies generally result from crossing B6 females to D2 males, whereas we used the reciprocal cross in line with our practice of propagating the K1422E variant via the paternal genome. Although the F1 offspring from these reciprocal crosses are all functionally heterozygous for B6 and D2 alleles at all autosomal loci, the Y chromosomes differ. It is also well documented that parent-of-origin effects such as genomic imprinting can lead to phenotypic differences between reciprocal F1 offspring[260–264].

These barriers to external comparison aside, the current study revealed minimal differences between groups in susceptibility to focal seizure events (Racine stage 3; **Figure 4.4A**) However, *Scn2a*$^{E/+}$ mice showed an overall resistance to seizure generalization (Racine stage 6) compared to WT. (**Figure 4.4B**). This finding is interesting for a few reasons. First, it reminiscent of the resistance to flurothyl seizure generalization we have described in B6.*Scn2a*$^{E/+}$ mice, suggesting that this effect is not flurothyl-specific. Next, the resistance to KA seizure generalization associated with the K1422E variant seems to be highly influenced by strain. Nearly 100% of WT mice reached stage 6, regardless of sex or strain compared to 16.67% of B6.*Scn2a*$^{E/+}$ males and 66.67% of B6.*Scn2a*$^{E/+}$ females. Meanwhile, 0% of F1D2.*Scn2a*$^{E/+}$ mice reached stage 6 (**Figure 4.4B**). This provides strong evidence for the effect of background strain on seizure susceptibility in *Scn2a*$^{E/+}$ mice. We also noted that B6.*Scn2a*$^{E/+}$ males showed greater resistance to both stage 3 and stage 6 seizures compared to B6 *Scn2a*$^{E/+}$ females (the difference in stage 3 was driven by latency rather than occurrence). Importantly, this sex-difference is only observable in *Scn2a*$^{E/+}$ mice on the B6 background. One explanation to account for this effect is that modifiers on the B6 background are having a sex-specific effect on phenotype severity associated with the K1422E variant. Another possibility is that this sex-difference is not specific to B6 and is instead being masked in highly resistant F1D2.*Scn2a*$^{E/+}$ mice. Resistance to seizure generalization associated with the K1422E variant becomes even more compelling when juxtaposed with lethality following KA administration. The data displayed in **Figure 4.4C** reflect lethality across all subjects included in the study. Interpreted as is, these data suggest that B6.WT males and females as well as B6.*Scn2a*$^{E/+}$ females are uniquely susceptible to lethality following KA administration. However, the interpretation changes if lethality is considered as percentage of subjects that die after reaching stage 6. This consideration of lethality is validated by the fact that death in this context is a consequence of a precipitating seizure and no lethality occurred without reaching stage 6 (**Figure 4.3B**). In this case, 100% of B6.*Scn2a*$^{E/+}$ mice died. Considering lethality in this way also presents limitations, namely with regard to group size. Given that so few B6.*Scn2a*$^{E/+}$ mice reached stage 6, those groups are underpowered relative to others. Similarly, it is not possible to assess the effect of background strain on lethality in this way because no F1D2.*Scn2a*$^{E/+}$mice reached stage 6. Thus, we have at least preliminary evidence that the K1422E variant is associated with resistance to seizure generalization but higher risk of death following a convulsive seizure. This further suggests that seizure generalization and lethality are separable phenotypes, which is the subject of a growing body of research[173,256,265–267]. Future studies will be aimed at dissecting the mechanisms these seemingly differential effects in the context of the K1422E variant.

Together these data suggest that background strain does affect phenotype severity in the *Scn2a*^{K1422E} mouse model. In some cases, the data presented are underpowered and so future studies will be aimed at replicating these results using fully powered cohorts. These studies would likely exclude further EEG video monitoring given the infrequent nature of spontaneous seizures across backgrounds. Studies on the effect of genetic background on seizure susceptibility have successfully identified genetic modifiers associated with transgenic models of high risk genes like *Scn2a* and with the endogenously susceptible D2 strain[163,169,176–183]. Future studies aimed at identifying modifier loci and genes responsible for the background effects observed here in the

Scn2a^{K1422E} mouse may yield similar results. However, the unique properties of the K1422E variant raise the possibility that unique modifiers may also be identified. Identification of shared modifiers will help expand our understanding of *Scn2a* in health and disease, while the identification of unique modifiers may provide clues regarding the pathological mechanisms of the K1422E variant.

Chapter 5. Final Discussion

5.1 Chapter Summaries

SCN2A variants have been associated with a wide range of NDD that reflect a complex spectrum of phenotypes[35]. Significant attention has been given to the extremes of this phenotypic spectrum, establishing a framework in which *SCN2A* missense variants that result in strong GoF effects are associated with DEE, while PTVs that result in LoF effects are associated with ID/ASD that sometimes present with co-morbid seizures starting later in life[70,71,74,81,82]. Continued efforts to establish genotype-phenotype correlations for *SCN2A*-related disorders can be supported by properly validated animal models of recurrent and mixed-effect variants. The work presented in this dissertation focused on the variant *SCN2A* p.K1422E, which has been shown previously to alter Nav1.2 ion selectivity in heterologous expression systems[130,132]. In **Chapter 2**, I described how we assessed K1422E channel function in heterologous expression systems. Consistent with previous work on rat Nav1.2 channels in *Xenopus* oocytes[130], we showed that substitution of glutamic acid for lysine at position 1422 (DEKA to DEEA) in human Nav1.2 confers calcium permeability not evident in WT human Nav1.2 channels (**Figure 2.1**). We used that data to develop a channel model and compartmental neuronal model to provide testable predictions for how K1422E affects neuronal function. Our modeling predicted lower peak AP speed associated with the K1422E variant (**Figure 2.2**). To further investigate this, we generated a novel mouse model (*Scn2a*^{K1422E}; **Figure 2.3 & 2.4**) and examined effects on cellular excitability using electrophysiological and imaging techniques. Excitatory neurons in neocortex exhibited features indicative of functional K1422E-containing Nav1.2 channels, including lower current density with a TTX-insensitive component (**Figure 2.5 & 2.6**) and aberrant calcium influx occurring during the Nav-mediated rising phase of the AP (**Figure 2.7**). Importantly, we are the first to demonstrate this effect in neurons. Analysis of behaving animals revealed a mix of neurological/neurobehavioral phenotypes, including infrequent spontaneous seizures (**Figure 2.9A-D**), altered susceptibility to chemically induced seizures (**Figure 2.9E-G**), reduced anxiety-like behavior (**Figure 2.10**), and alterations in olfactory-guided social behavior (**Figure 2.11 & 2.12**). Thus, these data suggest that altering Nav1.2 ion selectivity results in cellular and behavioral phenotypes that partially mirror those observed in other models of *Scn2a* dysfunction, in addition to features that are entirely unique to K1422E.

During our initial characterization of the *Scn2a*^{K1422E} mouse model (**Chapter 2**), we noted that the distribution of flurothyl seizure thresholds for *Scn2a*$^{E/+}$ females was non-normal compared to all other groups. This effect was subsequently replicated in two additional cohorts of *Scn2a*$^{E/+}$ and WT females. It has been widely documented that women with epilepsy often show a cyclical pattern of altered seizure susceptibility during specific phases of the menstrual cycle which can be attributed to fluctuations in hormones and corresponding changes in neurosteroid levels [147,148,155–157,159]. Studies using rodent models of epilepsy reveal complex, sometimes contradictory effects of ovarian hormones and neurosteroids on seizure susceptibility. In general, estradiol is proconvulsive and progesterone (along with its neurosteroid derivative allopregnalone) is anticonvulsive[147,148,160]. Based on these findings, we hypothesized that the estrous cycle affects susceptibility to flurothyl-induced seizures in *Scn2a*$^{E/+}$ female mice. In **Chapter 3**, we showed that historical data of flurothyl seizure thresholds in *Scn2a*$^{E/+}$ female mice have a statistically significant non-unimodal distribution (**Figure 3.1**). To test our stated hypothesis, we evaluated susceptibility to flurothyl-induced seizures in the context of ovariectomy, sham surgery, and no surgical treatment. We also performed estrous cycle monitoring (**Figure 3.2**) to evaluate surgery success and to evaluate whether flurothyl seizure threshold was associated with a particular stage of the estrous cycle in mice that underwent sham surgery or were untreated. Ovariectomy did not abolish the non-unimodal distribution of flurothyl seizure susceptibility in *Scn2a*$^{E/+}$ female mice (**Figure 3.3**). Additionally, flurothyl seizure thresholds were not associated with estrous cycle stage in mice that underwent sham surgery or were untreated (**Figure 3.4 and 3.5A**). These data suggest that variation in *Scn2a*$^{E/+}$ flurothyl seizure threshold is not significantly influenced by the estrous cycle and, by extension, fluctuations in ovarian hormones. However, we did find evidence of disrupted estrous cyclicity in untreated *Scn2a*$^{E/+}$ mice (**Figure 3.5B**), similar to what has been observed in other rodent models of epilepsy[230,238,246,247]. To our knowledge, this is the first demonstration of disrupted estrous cyclicity in a mouse model of an epilepsy-associated genetic variant, particularly *SCN2A*-related NDD.

In **Chapter 2**, we showed that *Scn2a*$^{E/+}$ mice on the B6 background exhibit NDD-related phenotypes, including alterations in anxiety-like behavior and seizure susceptibility. Evaluating the effects of a pathogenic variant in a single strain with limited genetic heterogeneity means that fewer animals are required for adequate statistical power. However, these strains are not representative of genetically heterogenous human populations. It is becoming increasingly evident that background genetic variation can affect the phenotypic properties of presumed "monogenic" disorders, including *SCN2A*-related NDD[21,22,24–28]. Accordingly, different genetic backgrounds across rodent strains have been shown to influence disease-related phenotypes, including seizure susceptibility[103,162–170]. Given the demonstrated effects of genetic background in other epilepsy models like *Scn2a*^{Q54}, we wanted to know if background strain affects phenotype severity in the *Scn2a*^{K1422E} mouse model. In **Chapter 4**, I described how we addressed this question by crossing *Scn2a*$^{E/+}$ males on the B6 background to inbred D2 females to generate F1 [D2×B6] hybrid offspring. We evaluated anxiety-like behavior and seizure susceptibility in WT and *Scn2a*$^{E/+}$ mice on the F1D2 background compared to mice on the B6 background. Convergent evidence from neurobehavioral assays demonstrated lower anxiety-like behavior in *Scn2a*$^{E/+}$ mice compared to WT and further suggested that this effect is more pronounced on the B6 background compared to the F1D2 background (**Figure 4.1**). F1D2.*Scn2a*$^{E/+}$ mice also exhibited rare spontaneous seizures (**Figure 4.2**) similar to those seen previously in B6.*Scn2a*$^{E/+}$ mice. Following administration of the chemoconvulsant kainic acid (KA), *Scn2a*$^{E/+}$ mice were less susceptible to seizure generalization but had elevated lethality risk, with variation based on strain and sex (**Figure 4.3 & 4.4**). These data suggest that background strain does affect phenotype severity in the *Scn2a*^{K1422E} mouse model.

5.2 Concluding Remarks and Future Directions

Potential pathogenic mechanisms of the K1422E variant

In **Chapter 1**, I referred to the unspoken promise of molecular genetics wherein a thorough understanding of genotype-phenotype relationships will enable more accurate prediction-based treatment decisions that yield better clinical outcomes. Even in the case of a truly monogenic NDD, dissecting the functional properties of a disease-causing variant is no small task. The effects of a given variant must be considered across multiple levels of phenotypic scale. In the case of *SCN2A*-related NDD, variants often have effects that span multiple aspects of channel function (e.g., voltage-dependence, kinetics). Changes in channel function affect the intrinsic properties of neurons, which in turn can affect the formation of neuronal circuits and overall functional connectivity of the brain. At the highest levels of phenotypic scale are neurological and neurobehavioral phenotypes associated with a given variant, which represent a complex summation of effects at smaller scales. Animal models can be useful platforms for multi-level functional annotation of disease-associated variants. To that end, we developed the *Scn2a*^{K1422E} mouse model and demonstrated altered ion permeation through Nav1.2 in neurons for the first time. We also presented a comprehensive characterization of neurological/neurobehavioral phenotypes in *Scn2a*$^{E/+}$ mice. This initial characterization is limited in terms of linking changes in the intrinsic properties of neurons to changes in network excitability/connectivity, as well as to the observed neurobehavioral phenotypes. Instead, this work serves as a starting point for future studies and establishes the *Scn2a*^{K1422E} mouse model as a sharable resource*. Additional complicating factors in linking channel function to circuit/system-level phenotypes are developmentally regulated splicing that affect the properties of Nav1.2 and changes in subcellular distribution during myelination that affect the contribution of Nav1.2 to neuronal excitability[55,60–62,68,69]. Thus, future studies aimed at understanding the pathophysiological mechanisms of the K1422E variant will need to account for cell-type specific and developmentally regulated changes in the expression of Nav1.2 by looking at various cell types across different age ranges. These limitations in mind, we can speculate about potential pathogenic mechanisms of the K1422E variant by considering our findings alongside previous research on *SCN2A* dysfunction.

Mechanisms of *SCN2A* variant pathogenicity may be cell autonomous, operating on relatively short timescales; and may also involve larger scale changes in neuronal circuits that affect the trajectory of neurodevelopment. Additionally, pathogenic mechanisms may differ across cell types based on differences in channel expression and subcellular localization. In **Chapter 2**, we

*Available via the Mutant Mouse Resource & Research Centers (Stock #MMRRC:069700-UCD) identified two major channel level effects associated with the K1422E variant: reduced current density with at least partial contribution from calcium antagonism[130], and excess calcium influx. We further showed that *Scn2a*$^{E/+}$ pyramidal cells had slower peak AP speed compared with WT that is likely associated with reduced current density through the channel. This reduction in AP speed (13%) is smaller than that observed in *Scn2a*$^{+/-}$ heterozygotes (27%)[125], consistent with a reduction, but not elimination, of current density through channels with the K1422E variant. It has been shown that progressively severe deficiency of Nav1.2 expression is associated with paradoxical and cell-autonomous hyperexcitability in excitatory neurons from the neocortex and striatum[125,126]. We observed a similar, but ultimately non-significant effect on AP firing rate in *Scn2a*$^{E/+}$ pyramidal cells, suggesting that this is likely not the primary pathophysiological mechanism in this cell type. However, additional calcium influx could have myriad effects on AIS function, as many AIS components are regulated directly by calcium or through calcium/calmodulin interactions[207–210]. Additionally, excess calcium influx could affect cellular processes beyond the AIS as Nav1.2 channels are also expressed in the somatodendritic domain and throughout the axons of unmyelinated neurons[56,65,66,211,212]. Future studies of the K1422E variant will benefit from techniques used to interrogate subtle dynamic calcium signaling events such as calcium sparks.

Genetic risk for multiple NDDs is conferred by variation in overlapping sets of genes including *SCN2A*, suggesting some shared molecular pathway features that may account for symptom/comorbidity overlap[2,10]. Functional annotation of overlapping risk genes implicates disruption of synaptic networks as a potential mechanism of NDD pathophysiology[5,7,10,27,268,269]. Spratt and colleagues reported that loss of Nav1.2 reduced action potential backpropagation in glutamatergic pyramidal cells, resulting in impaired synaptic plasticity and strength[58]. They also reported that dendritic spines in mature (>P23) Nav1.2 haploinsufficient neurons displayed features of morphological immaturity. Specifically, *Scn2a*$^{+/-}$ spines were longer and had smaller heads relative to total spine volume when compared to wild-type spines. Reduced current density and/or excess calcium associated with the K1422E variant may affect dendritic integration which could be probed using methods similar to those used by Spratt and colleagues[58]. As previously mentioned, Nav1.2 is expressed throughout the axonal compartment in unmyelinated neurons [65,66,211]. Furthermore, intracellular sodium concentrations can exceed 50 mM in some nerve terminals during high frequency activity[212]. Excess calcium influx through K1422E channels could therefore affect transmitter release and short-term presynaptic plasticity[213,214].

Just as we demonstrated mixed effects on channel function as a result of the K1422E variant, *Scn2a*$^{E/+}$mice displayed a mix of neurological and neurobehavioral phenotypes. This raises the possibility that different phenotypes may reflect different effects on channel function as well as differences in channel expression and subcellular localization across cell types. Given the reduced penetrance of spontaneous seizures in *Scn2a*$^{E/+}$ mice, it is difficult to speculate about potential pathogenic mechanisms which likely involve extragenic modifying factors. As previously discussed, we did not find strong evidence of cell autonomous changes in the excitability of neocortical pyramidal cells from *Scn2a*$^{E/+}$ mice. It is possible that spontaneous seizures arise from a different cell type/circuit such as the hippocampus. Probing spontaneous seizures using multi-channel EEG or depth recordings may support future localization efforts. In order to further investigate seizure susceptibility in *Scn2a*$^{E/+}$ mice, we induced seizures using flurothyl and KA. In both cases, *Scn2a*$^{E/+}$ mice did not differ from WT in terms of susceptibility to focal seizure events (MJ for flurothyl, Racine stage 3 for KA). However, *Scn2a*$^{E/+}$ mice were less susceptible to generalized seizure events (GTCS for flurothyl, Racine stage 6 for KA) compared to WT, suggesting resistance to seizure spread. This is somewhat unexpected given the localized spontaneous seizures observed using EEG. However, paradoxical induced seizure thresholds have been observed in other mouse epilepsy models and may reflect differential expression of Nav1.2 across cell types and across neuronal circuits involved in producing different types of seizures[216–218]. Given the role of Nav1.2 in AP backpropagation[52,55,60], one possibility is that reduced current density and/or excess calcium associated with K1422E variant expressed in the somatodendritic compartment disrupts spreading depolarization and subsequent seizure generalization. As previously discussed, seizure generalization and lethality can be considered separate phenotypes[173,256,265–267]. In **Chapter 4**, we showed preliminary evidence that the K1422E variant is associated with higher risk of death following KA administration. It is estimated that 13% of patients with *SCN2A*-related epilepsy die as a result of sudden unexpected death in epilepsy (SUDEP)[270]. The mechanisms that underlie SUDEP are unclear and likely involve multiple factors but one hypothesis proposes that spreading depolarization in the brainstem mediates cardiorespiratory arrest that leads to death[54,271,272]. Interestingly, *Scn2a* has been shown to be highly expressed in the mouse brainstem[54,113]. In addition, Mishra et al. (2017) showed that heterozygous knockout of *Scn2a* is a protective modifier of lethality in SUDEP-prone *Kcna1* (voltage-gated potassium channel gene) knockout mice[113]. Moreover, homozygous knockout of *Scn2a* is associated with perinatal lethality due to respiratory depression[54]. We noted similar lethality in mice homozygous for the K1422E variant. Together these results suggest that *Scn2a* may be important for brainstem mediated control of respiration. This prospect is made even more interesting considering that partial LoF in the gene *Cacna1a* is also a protective modifier of lethality in SUDEP-prone *Kcna1* knockout mice[273]. *Cacna1a* encodes the pore forming alpha subunit of P/Q-type calcium channels that mediate neurotransmitter release at terminals and is also associated with epilepsy[274,275]. Furthermore, GoF mutations in the ryanodine receptor-2 gene that result in "leaky" channels have been linked to SUDEP and have been shown to mediate spreading depolarization in brainstem autonomic microcircuits[276]. Ryanodine receptor-2 is a channel that increases cytoplasmic calcium levels via release from intracellular storage organelles[277]. Based on these findings, it is possible that excess calcium influx through K1422E channels expressed in the nerve terminal could also mediate spreading depolarization in the brainstem following a severe seizure, leading to cardiorespiratory arrest and death. This suggests a potential mechanism for the higher risk of death associated with the K1422E variant following KA administration. It should be noted that lethality following acute administration of KA is not a direct model of SUDEP by definition. However, such models are useful for investigating factors that influence cardiorespiratory arrest following seizure activity that may generalize to mechanisms of SUDEP[278,279].

On the utility of modifying factors

A central theme of this dissertation is that disease phenotypes associated with rare driver mutations can show variability based on modifying factors. The rise of the inbred animal population as a pillar of biomedical research was largely based on the assumption that reduced genetic variability corresponds to reduced phenotypic variability. Interestingly, a number of studies (not all of them recent) cast doubt on this assumption; inbred mouse strains do not show lower trait variability compared to genetically heterogenous "outbred" stocks[280–282]. The advancements made using inbred research animals stand in opposition to mounting evidence that factors outside of genetics influence trait variability and that limiting genetic heterogeneity may actually limit the generalizability of research findings[118,254,283]. This has fueled calls to embrace heterogeneity as way of phenocopying trait variability seen in diverse human populations by using more genetically diverse strains (e.g., collaborative cross mice) and developing naturalized mouse models[284–286].

The importance of considering sex as a biological variable with implications for trait variability in health and disease cannot be overstated. Historically, biological sex has been neglected as a variable in both human and non-human research, with a strong bias towards male subjects[136,137]. The rationale for this bias echoes the rationale for using inbred populations of animals: hormonal fluctuations introduce variability into research populations that can confound results[136]. A number of studies have provided evidence contrary to this general sentiment, showing that female rodents are not more variable than males across neurobehavioral phenotypes[139,287,288]. This represents an important argument against the exclusion of female subjects but should not misinterpreted as a suggestion that sex-specific variables or effects can be ignored. Sex differences are present at multiple levels of organization in the central nervous system and have been reported in a number of NDD[137–139,143–148]. Furthermore, the conceptualization of sex as a variable distinguishing the binary categories of male and female should be considered a limited proxy for more complex variables including gene expression profiles and hormonal fluctuations[289]. Rocks and colleagues nicely illustrated this point in the context of the estrous cycle by re-analyzing their previously published neurobehavioral data with or without estrous cycle information[139]. They showed that while female data was not more variable than male data, female variability was not predictive of whether or not a given outcome was affected by estrous cycle stage[139]. Data presented in this dissertation reinforces this general finding. In **Chapter 2,** we noted that the distribution of flurothyl seizure thresholds for *Scn2a*$^{E/+}$ females was non-normal compared to all other group. However, we showed in **Chapter 3** that this effect was likely not associated with the estrous cycle. Despite these negative results, estrous cycle monitoring unexpectedly yielded preliminary evidence of disrupted cyclicity in *Scn2a*$^{E/+}$ female mice. While it will undoubtedly require more effort, embracing the complexity of sex differences will enhance the resolution of neuroscience studies in support of more inclusive biomedical research.

Many of the phenotypes we observed during our initial characterization of B6.*Scn2a*$^{E/+}$ mice, such as lower anxiety-like behavior and lower susceptibility to induced seizures, were statistically significant and reproducible **(Chapters 2 & 3)**. However, spontaneous seizures were rare and difficult to observe in B6.*Scn2a*$^{E/+}$ mice (**Figure 2.9A & B**). Our rationale for pursuing strain-dependence of phenotypes in the *Scn2a*^{K1422E} model was two-fold. First, we wanted to explore the possibility that crossing to a different background strain would unmask a more robust spontaneous seizure phenotype that would enhance the translatability of the model. Second, analysis of strain-dependence can serve as the basis for future studies to identify modifier loci and genes, which in turn can provide clues about potential pathways underlying the pathogenic mechanisms of the K1422E variant. We evaluated strain-dependence in the context of a pure B6 background and an F1D2 hybrid background. While certainly more informative than a single genetic background, the trait disruptions shown in the context of these two backgrounds should not be considered essential vis-à-vis the K1422E variant. A study conducted by Tabbaa & Knoll et al. exemplifies the degree to which genetic background diversity can influence phenotype severity associated with haploinsufficiency in a high confidence ASD risk gene (*Cdh8*)[290]. In contrast to our study which used two unrelated inbred strains, the study by Tabbaa & Knoll et al. used panels of genetically diverse recombinant inbred strains from the collaborative cross and C57BL/6J × DBA/2J (B×D) collections[290]. Recombinant inbred strains are derived from crosses of two or more genetically distinct inbred strains (8 in the case of collaborative cross lines)[284,291,292]. As a result of meiotic crossover events and subsequent inbreeding, each recombinant inbred strain in a given collection is isogenic for a unique pattern of haplotypes inherited from parental strains[284,291,292]. Tabbaa & Knoll et al. crossed heterozygous *Cdh8* knockout females on the B6 background to WT males from 27 collaborative cross lines, 5 B×D lines, and the pure B6 line to generate an F1 population and assessed neurobehavioral phenotypes in over 1,000 mice using five different assays[290]. They showed that population-level effects on phenotypic penetrance associated with *Cdh8* haploinsufficiency varied across measured traits[290]. More importantly, they showed that strain and sex modify penetrance of *Cdh8* haploinsufficiency, with individual strains showing complex profiles of susceptibility and resistance to different traits[290]. While obviously labor- and resource-intensive, this strategy represents the gold standard for a systematic examination of phenotypic heterogeneity associated with a pathogenic variant in the context of genetic diversity. Applying a similar strategy to the $Scn2a^{K1422E}$ model would enable identification of highly penetrant, population level trait disruptions that could provide clues about the primary pathogenic mechanism of the K1422E variant. In addition, examining strain level effects could reveal genetic backgrounds with unique susceptibility profiles that would be relevant for future studies on specific traits such as seizure susceptibility. The reductionist approach to biomedical research where variation is limited to better resolve the effects of experimental manipulations has certainly paid dividends with regard to our understanding of molecular pathways and disease mechanisms in specific contexts, but this may come at the expense of realism. Improvements in analytical tools and resources for modeling heterogeneity will allow us to embrace the complexity of biological systems and enhance research translatability.

External validity: mice versus humans

No discussion of a human disease variant mouse model could be considered complete without a formal acknowledgment of the mouse in the room: namely that mice are not people. The *SCN2A*-p.K1422E variant is associated with infantile spasms and features of ASD in humans[85]. As such, the generation of *Scn2a*^{K1422E} mice was at least partially motivated by the need for a model that displays clinically relevant phenotypes and could be used to interrogate mechanisms of disease as well as to screen potential therapeutic interventions. As previously discussed, spontaneous seizures showed low penetrance in juvenile *Scn2a*$^{E/+}$ mice. Given the developmentally-regulated changes in splice isoforms and subcellar expression patterns that affect the contributions of Nav1.2 to neuronal excitability, it's possible that seizures show higher penetrance in younger mice and spontaneously remit[55,60–62,68,69]. However, we did not find any preliminary evidence of observable seizures in *Scn2a*$^{E/+}$ mice pre-weaning (data not shown), although this was not confirmed by EEG due to technical limitations related to tethered EEG recordings in pre-weanling mice. Another possibility is that the penetrance of spontaneous seizures is affected by genetic background, which has been suggested from other mouse epilepsy models[103,162–175]. A more thorough examination of phenotypic heterogeneity using diverse genetic reference panels could reveal a strain with susceptibility to spontaneous seizures. Discussion of how genetic background can affect phenotypic penetrance within the same species logically raises the possibility that phenotypic penetrance might differ between mice and humans. While there are a number of similarities between mice and humans with regard to cortical structure, connectivity, and development, there are also important differences[293–299]. The general laminar organization of the neocortex is conserved between mice and humans, likely reflecting conserved mechanisms of cortical development where neurons migrate from ventricular progenitor zones into the developing cortical layers according to birthdate[293,294]. However, primates have a prolonged period of neurogenesis and different distributions of neural progenitor cell types that are thought to underlie greater cortical thickness, gyrification (cortical folding), and laminar proportionality in humans compared to mice[293,294]. Single-cell/nucleus RNA-sequencing analysis comparing cell types in human and mouse cortex suggests that cellular architecture is well-conserved, enabling matching of homologous cell types[295]. Subsequent analysis of homologous cell types revealed differences in proportions, laminar distribution, gene expression, and morphology[295]. Comparison of the human and mouse cortical connectomes demonstrates conservation of total synaptic input and inhibitory-to-excitatory input balance in pyramidal cells, whereas human have an expanded interneuron-to-interneuron network that is virtually absent in mice[296]. Finally, human cortical pyramidal neurons show different input-output properties compared to rodents, including higher synaptic thresholds for dendritic spike generation and novel calcium-mediated dendritic action potentials in layer II/III cells[297–299]. Though speculative, the relatively high expression of Nav1.2 in neocortical pyramidal cells, coupled with its presumed involvement in AP backpropagation and dendritic excitability, lends credence to the idea that fundamental differences between mice and humans could lead to differences in phenotypic penetrance associated with *SCN2A* variants[52,55,58,60,65,66]. If proven true, this may have implications for other mouse models of *SCN2A* variants. Alternatively, this may reflect the unique properties of the K1422E variant with regard to ion selectivity. This discussion suggests that care must be taken when generalizing research findings generated using model systems. As much as this applies for effects and the level of channels and neurons, it is especially relevant for neurological and neurobehavioral phenotypes such as those associated with ASD. Ultimately, there is no such thing as a perfect model and understanding the limits of translatability is essential for model development and usage. It may be that the primary utility of the *Scn2a*$^{E/+}$ mouse model is to support basic science inquiries into the consequences of altered ion selectivity. The findings presented here can support parallel investigations using other platforms including patient-derived pluripotent stem cells, organoids, and other animal model systems. Finally, this dissertation serves as a case study highlighting the importance of considering modifying factors of disease phenotypes that present as complex traits.

References

1. American Psychiatric Association. *Diagnostic and Statistical Manual of Mental Disorders*. (American Psychiatric Association, 2013). doi:10.1176/appi.books.9780890425596.
2. Morris-Rosendahl, D. J. & Crocq, M.-A. Neurodevelopmental disorders—the history and future of a diagnostic concept. *Dialogues Clin. Neurosci.* **22**, 65–72 (2020).
3. Rauch, A. *et al.* Range of genetic mutations associated with severe non-syndromic sporadic intellectual disability: an exome sequencing study. *The Lancet* **380**, 1674–1682 (2012).
4. Ku, C. S. *et al.* A new paradigm emerges from the study of de novo mutations in the context of neurodevelopmental disease. *Mol. Psychiatry* **18**, 141–153 (2013).
5. Fromer, M. *et al.* De novo mutations in schizophrenia implicate synaptic networks. *Nature* **506**, 179–184 (2014).
6. Hoischen, A., Krumm, N. & Eichler, E. E. Prioritization of neurodevelopmental disease genes by discovery of new mutations. *Nat. Neurosci.* **17**, 764–772 (2014).
7. Iossifov, I. *et al.* The contribution of de novo coding mutations to autism spectrum disorder. *Nature* **515**, 216–221 (2014).
8. Fitzgerald, T. W. *et al.* Large-scale discovery of novel genetic causes of developmental disorders. *Nature* **519**, 223–228 (2015).
9. Carroll, L. S. *et al.* Mutation screening of SCN2A in schizophrenia and identification of a novel loss-of-function mutation. *Psychiatr. Genet.* **26**, 60–65 (2016).
10. Li, J. *et al.* Genes with de novo mutations are shared by four neuropsychiatric disorders discovered from NPdenovo database. *Mol. Psychiatry* **21**, 290–297 (2016).
11. Bowling, K. M. *et al.* Genomic diagnosis for children with intellectual disability and/or developmental delay. *Genome Med.* **9**, 43 (2017).

12. Niemi, M. E. K. *et al.* Common genetic variants contribute to risk of rare severe neurodevelopmental disorders. *Nature* **562**, 268–271 (2018).

13. Owen, M. J. & O'Donovan, M. C. Schizophrenia and the neurodevelopmental continuum:evidence from genomics. *World Psychiatry* **16**, 227–235 (2017).

14. Boyle, C. A. *et al.* Trends in the prevalence of developmental disabilities in US children, 1997-2008. *Pediatrics* **127**, 1034–1042 (2011).

15. Craig, B. M., Hartman, J. D., Owens, M. A. & Brown, D. S. Prevalence and Losses in Quality-Adjusted Life Years of Child Health Conditions: A Burden of Disease Analysis. *Matern. Child Health J.* **20**, 862–869 (2016).

16. McCarthy, M. I. *et al.* Genome-wide association studies for complex traits: consensus, uncertainty and challenges. *Nat. Rev. Genet.* **9**, 356–369 (2008).

17. Manolio, T. A. *et al.* Finding the missing heritability of complex diseases. *Nature* **461**, 747–753 (2009).

18. Thomas, R. H. & Berkovic, S. F. The hidden genetics of epilepsy—a clinically important new paradigm. *Nat. Rev. Neurol.* **10**, 283–292 (2014).

19. Claes, L. *et al.* De novo SCN1A mutations are a major cause of severe myoclonic epilepsy of infancy. *Hum. Mutat.* **21**, 615–621 (2003).

20. Harkin, L. A. *et al.* The spectrum of SCN1A-related infantile epileptic encephalopathies. *Brain* **130**, 843–852 (2007).

21. Dipple, K. M. & McCabe, E. R. B. Phenotypes of Patients with "Simple" Mendelian Disorders Are Complex Traits: Thresholds, Modifiers, and Systems Dynamics. *Am. J. Hum. Genet.* **66**, 1729–1735 (2000).

22. Dipple, K. M. & McCabe, E. R. B. Modifier Genes Convert "Simple" Mendelian Disorders to Complex Traits. *Mol. Genet. Metab.* **71**, 43–50 (2000).

23. Dipple, K. M., Phelan, J. K. & McCabe, E. R. B. Consequences of Complexity within Biological Networks: Robustness and Health, or Vulnerability and Disease. *Mol. Genet. Metab.* **74**, 45–50 (2001).
24. Nadeau, J. H. Modifier genes in mice and humans. *Nat. Rev. Genet.* **2**, 165–174 (2001).
25. Slavotinek, A. Genetic modifiers in human development and malformation syndromes, including chaperone proteins. *Hum. Mol. Genet.* **12**, 45R – 50 (2003).
26. Noebels, J. Pathway-driven discovery of epilepsy genes. *Nat. Neurosci.* **18**, 344–350 (2015).
27. Satterstrom, F. K. *et al.* Large-Scale Exome Sequencing Study Implicates Both Developmental and Functional Changes in the Neurobiology of Autism. *Cell* **180**, 568-584.e23 (2020).
28. Campbell, C. *et al.* The role of common genetic variation in presumed monogenic epilepsies. *eBioMedicine* **81**, 104098 (2022).
29. Meisler, M. H. & Kearney, J. A. Sodium channel mutations in epilepsy and other neurological disorders. *J. Clin. Invest.* **115**, 2010–2017 (2005).
30. Lerche, H. *et al.* Ion channels in genetic and acquired forms of epilepsy. *J. Physiol.* **591**, 753–764 (2013).
31. Meisler, M. H., Hill, S. F. & Yu, W. Sodium channelopathies in neurodevelopmental disorders. *Nat. Rev. Neurosci.* 1–15 (2021) doi:10.1038/s41583-020-00418-4.
32. Gur Barzilai, M. *et al.* Convergent Evolution of Sodium Ion Selectivity in Metazoan Neuronal Signaling. *Cell Rep.* **2**, 242–248 (2012).
33. Zakon, H. H. Adaptive evolution of voltage-gated sodium channels: The first 800 million years. *Proc. Natl. Acad. Sci. U. S. A.* **109**, 10619–10625 (2012).
34. Plummer, N. W. & Meisler, M. H. Evolution and Diversity of Mammalian Sodium Channel Genes. *Genomics* **57**, 323–331 (1999).

35. Sanders, S. J. *et al.* Progress in Understanding and Treating SCN2A-Mediated Disorders. *Trends Neurosci.* **41**, 442–456 (2018).

36. Isom, L. L., De Jongh, K. S. & Catterall, W. A. Auxiliary subunits of voltage-gated ion channels. *Neuron* **12**, 1183–1194 (1994).

37. Isom, L. L. *et al.* Structure and function of the β2 subunit of brain sodium channels, a transmembrane glycoprotein with a CAM motif. *Cell* **83**, 433–442 (1995).

38. Marban, E., Yamagishi, T. & Tomaselli, G. F. Structure and function of voltage-gated sodium channels. *J. Physiol.* **508**, 647–657 (1998).

39. Yellen, G., Jurman, M. E., Abramson, T. & MacKinnon, R. Mutations affecting internal TEA blockade identify the probable pore-forming region of a K+ channel. *Science* **251**, 939–942 (1991).

40. Dudev, T. & Lim, C. Ion Selectivity Strategies of Sodium Channel Selectivity Filters. *Acc. Chem. Res.* **47**, 3580–3587 (2014).

41. Zhou, W., Chung, I., Liu, Z., Goldin, A. L. & Dong, K. A Voltage-Gated Calcium-Selective Channel Encoded by a Sodium Channel-like Gene. *Neuron* **42**, 101–112 (2004).

42. Stephens, R. F., Guan, W., Zhorov, B. S. & Spafford, J. D. Selectivity filters and cysteine-rich extracellular loops in voltage-gated sodium, calcium, and NALCN channels. *Front. Physiol.* **6**, (2015).

43. Meves, H. & Vogel, W. Calcium inward currents in internally perfused giant axons. *J. Physiol.* **235**, 225–265 (1973).

44. Kawai, T. *et al.* Heterologous functional expression of ascidian Nav1 channels and close relationship with the evolutionary ancestor of vertebrate Nav channels. *J. Biol. Chem.* **296**, (2021).

45. Yang, N. & Horn, R. Evidence for voltage-dependent S4 movement in sodium channels. *Neuron* **15**, 213–218 (1995).

46. Yang, N., George, A. L. & Horn, R. Molecular Basis of Charge Movement in Voltage-Gated Sodium Channels. *Neuron* **16**, 113–122 (1996).

47. Yang, N., George, A. L. & Horn, R. Probing the outer vestibule of a sodium channel voltage sensor. *Biophys. J.* **73**, 2260–2268 (1997).

48. Stühmer, W. *et al.* Structural parts involved in activation and inactivation of the sodium channel. *Nature* **339**, 597–603 (1989).

49. West, J. W. *et al.* A cluster of hydrophobic amino acid residues required for fast Na(+)-channel inactivation. *Proc. Natl. Acad. Sci. U. S. A.* **89**, 10910–10914 (1992).

50. Hille, B. Ionic channels in excitable membranes. Current problems and biophysical approaches. *Biophys. J.* **22**, 283–294 (1978).

51. Du, J. *et al.* Differential excitatory vs inhibitory SCN expression at single cell level regulates brain sodium channel function in neurodevelopmental disorders. *Eur. J. Paediatr. Neurol.* (2019) doi:10.1016/j.ejpn.2019.12.019.

52. Hu, W. *et al.* Distinct contributions of Na v 1.6 and Na v 1.2 in action potential initiation and backpropagation. *Nat. Neurosci.* **12**, 996–1002 (2009).

53. Li, T. *et al.* Action Potential Initiation in Neocortical Inhibitory Interneurons. *PLoS Biol.* **12**, e1001944 (2014).

54. Planells-Cases, R. *et al.* Neuronal death and perinatal lethality in voltage-gated sodium channel alpha(II)-deficient mice. *Biophys. J.* **78**, 2878–2891 (2000).

55. Osorio, N. *et al.* Differential targeting and functional specialization of sodium channels in cultured cerebellar granule cells. *J. Physiol.* **569**, 801–816 (2005).

56. Lorincz, A. & Nusser, Z. Molecular Identity of Dendritic Voltage-Gated Sodium Channels. *Science* **328**, 906–909 (2010).

57. Yamagata, T., Ogiwara, I., Mazaki, E., Yanagawa, Y. & Yamakawa, K. Nav1.2 is expressed in caudal ganglionic eminence-derived disinhibitory interneurons: Mutually exclusive distributions of Nav1.1 and Nav1.2. *Biochem. Biophys. Res. Commun.* **491**, 1070–1076 (2017).

58. Spratt, P. W. E. *et al.* The Autism-Associated Gene Scn2a Contributes to Dendritic Excitability and Synaptic Function in the Prefrontal Cortex. *Neuron* **103**, 673-685.e5 (2019).

59. Workman, A. D., Charvet, C. J., Clancy, B., Darlington, R. B. & Finlay, B. L. Modeling transformations of neurodevelopmental sequences across mammalian species. *J. Neurosci. Off. J. Soc. Neurosci.* **33**, 7368–7383 (2013).

60. Boiko, T. *et al.* Compact myelin dictates the differential targeting of two sodium channel isoforms in the same axon. *Neuron* **30**, 91–104 (2001).

61. Gazina, E. V. *et al.* 'Neonatal' Nav1.2 reduces neuronal excitability and affects seizure susceptibility and behaviour. *Hum. Mol. Genet.* **24**, 1457–1468 (2015).

62. Kaplan, M. R. *et al.* Differential Control of Clustering of the Sodium Channels Nav1.2 and Nav1.6 at Developing CNS Nodes of Ranvier. *Neuron* **30**, 105–119 (2001).

63. Rush, A. M., Dib-Hajj, S. D. & Waxman, S. G. Electrophysiological properties of two axonal sodium channels, Nav1.2 and Nav1.6, expressed in mouse spinal sensory neurones. *J. Physiol.* **564**, 803–815 (2005).

64. Kole, M. H. P. *et al.* Action potential generation requires a high sodium channel density in the axon initial segment. *Nat. Neurosci.* **11**, 178–186 (2008).

65. Westenbroek, R. E., Merrick, D. K. & Catterall, W. A. Differential subcellular localization of the RI and RII Na+ channel subtypes in central neurons. *Neuron* **3**, 695–704 (1989).

66. Gong, B., Rhodes, K. J., Bekele-Arcuri, Z. & Trimmer, J. S. Type I and type II Na+ channel α-subunit polypeptides exhibit distinct spatial and temporal patterning, and association with auxiliary subunits in rat brain. *J. Comp. Neurol.* **412**, 342–352 (1999).

67. Sarao, R., Gupta, S. K., Auld, V. J. & Dunn, R. J. Developmentally regulated alternative RNA splicing of rat brain sodium channel mRNAs. *Nucleic Acids Res.* **19**, 5673–5679 (1991).

68. Xu, R. *et al.* A childhood epilepsy mutation reveals a role for developmentally regulated splicing of a sodium channel. *Mol. Cell. Neurosci.* **35**, 292–301 (2007).

69. Gazina, E. V. *et al.* Differential expression of exon 5 splice variants of sodium channel α subunit mRNAs in the developing mouse brain. *Neuroscience* **166**, 195–200 (2010).

70. Ben-Shalom, R. *et al.* Opposing Effects on Na V 1.2 Function Underlie Differences Between SCN2A Variants Observed in Individuals With Autism Spectrum Disorder or Infantile Seizures. *Biol. Psychiatry* **82**, 224–232 (2017).

71. Wolff, M. *et al.* Genetic and phenotypic heterogeneity suggest therapeutic implications in SCN2A-related disorders. *Brain* **140**, 1316–1336 (2017).

72. Wolff, M., Brunklaus, A. & Zuberi, S. M. Phenotypic spectrum and genetics of SCN2A-related disorders, treatment options, and outcomes in epilepsy and beyond. *Epilepsia* **60**, S59–S67 (2019).

73. Sanders, S. J. *et al.* De novo mutations revealed by whole exome sequencing are strongly associated with autism. *Nature* **485**, 237–241 (2012).

74. Shi, X. *et al.* Clinical spectrum of SCN2A mutations. *Brain Dev.* **34**, 541–545 (2012).

75. Krumm, N., O'Roak, B. J., Shendure, J. & Eichler, E. E. A de novo convergence of autism genetics and molecular neuroscience. *Trends Neurosci.* **37**, 95–105 (2014).

76. Rees, E. *et al.* Analysis of exome sequence in 604 trios for recessive genotypes in schizophrenia. *Transl. Psychiatry* **5**, e607 (2015).

77. Kobayashi, Y. *et al.* High prevalence of genetic alterations in early-onset epileptic encephalopathies associated with infantile movement disorders. *Brain Dev.* **38**, 285–292 (2016).

78. Dimassi, S. *et al.* Whole-exome sequencing improves the diagnosis yield in sporadic infantile spasm syndrome. *Clin. Genet.* **89**, 198–204 (2016).

79. Allen, N. M. *et al.* Unexplained early onset epileptic encephalopathy: Exome screening and phenotype expansion. *Epilepsia* **57**, e12–e17 (2016).

80. Olson, H. E. *et al.* Genetics and genotype-phenotype correlations in early onset epileptic encephalopathy with burst suppression. *Ann. Neurol.* **81**, 419–429 (2017).

81. Brunklaus, A., Ellis, R., Reavey, E., Semsarian, C. & Zuberi, S. M. Genotype phenotype associations across the voltage-gated sodium channel family. *J. Med. Genet.* **51**, 650–658 (2014).

82. Begemann, A. *et al.* Further corroboration of distinct functional features in SCN2A variants causing intellectual disability or epileptic phenotypes. *Mol. Med.* **25**, (2019).

83. Thompson, C. H., Ben-Shalom, R., Bender, K. J. & George, A. L. Alternative splicing potentiates dysfunction of early-onset epileptic encephalopathy SCN2A variants. *J. Gen. Physiol.* **152**, e201912442 (2020).

84. Ogiwara, I. *et al.* De novo mutations of voltage-gated sodium channel αII gene SCN2A in intractable epilepsies. *Neurology* **73**, 1046–1053 (2009).

85. Sundaram, S. K., Chugani, H. T., Tiwari, V. N. & Huq, A. M. SCN2A mutation is associated with infantile spasms and bitemporal glucose hypometabolism. *Pediatr. Neurol.* **49**, (2013).

86. Touma, M. *et al.* Whole genome sequencing identifies SCN2A mutation in monozygotic twins with Ohtahara Syndrome and unique neuropathological findings. *Epilepsia* **54**, e81–e85 (2013).

87. Nakamura, K. *et al.* Clinical spectrum of SCN2A mutations expanding to Ohtahara syndrome. *Neurology* **81**, 992–998 (2013).

88. Zerem, A. *et al.* Paternal germline mosaicism of a SCN2A mutation results in Ohtahara syndrome in half siblings. *Eur. J. Paediatr. Neurol.* **18**, 567–571 (2014).

89. Martin, H. C. *et al.* Clinical whole-genome sequencing in severe early-onset epilepsy reveals new genes and improves molecular diagnosis. *Hum. Mol. Genet.* **23**, 3200–3211 (2014).

90. Howell, K. B. *et al.* SCN2A encephalopathy. *Neurology* **85**, 958–966 (2015).

91. Syrbe, S. *et al.* Phenotypic Variability from Benign Infantile Epilepsy to Ohtahara Syndrome Associated with a Novel Mutation in SCN2A. *Mol. Syndromol.* **7**, 182–188 (2016).
92. Scheffer, I. E. *et al.* ILAE classification of the epilepsies: Position paper of the ILAE Commission for Classification and Terminology. *Epilepsia* **58**, 512–521 (2017).
93. Sugawara, T. *et al.* A missense mutation of the Na+ channel alpha II subunit gene Na(v)1.2 in a patient with febrile and afebrile seizures causes channel dysfunction. *Proc. Natl. Acad. Sci. U. S. A.* **98**, 6384–6389 (2001).
94. Heron, S. E. *et al.* Sodium-channel defects in benign familial neonatal-infantile seizures. *The Lancet* **360**, 851–852 (2002).
95. Zuberi, S. M. *et al.* ILAE classification and definition of epilepsy syndromes with onset in neonates and infants: Position statement by the ILAE Task Force on Nosology and Definitions. *Epilepsia* **63**, 1349–1397 (2022).
96. Liao, Y. *et al.* Molecular correlates of age-dependent seizures in an inherited neonatal-infantile epilepsy. *Brain* **133**, 1403–1414 (2010).
97. Scalmani, P. *et al.* Effects in Neocortical Neurons of Mutations of the Nav1.2 Na+ Channel causing Benign Familial Neonatal-Infantile Seizures. *J. Neurosci.* **26**, 10100–10109 (2006).
98. Misra, S. N., Kahlig, K. M. & George, A. L. Impaired NaV1.2 function and reduced cell surface expression in benign familial neonatal-infantile seizures. *Epilepsia* **49**, 1535–1545 (2008).
99. Berecki, G. *et al.* Dynamic action potential clamp predicts functional separation in mild familial and severe de novo forms of *SCN2A* epilepsy. *Proc. Natl. Acad. Sci.* **115**, E5516–E5525 (2018).
100. Yang, X.-R. *et al.* *SCN2A* -related epilepsy of infancy with migrating focal seizures: report of a variant with apparent gain- and loss-of-function effects. *J. Neurophysiol.* **127**, 1388–1397 (2022).

101. Que, Z. *et al.* Hyperexcitability and pharmacological responsiveness of cortical neurons derived from human iPSCs carrying epilepsy-associated sodium channel Nav1.2-L1342P genetic variant. *J. Neurosci.* (2021) doi:10.1523/JNEUROSCI.0564-21.2021.

102. Crawford, K. *et al.* Computational analysis of 10,860 phenotypic annotations in individuals with SCN2A -related disorders. *Genet. Med.* 1–10 (2021) doi:10.1038/s41436-021-01120-1.

103. Kearney, J. A. *et al.* A gain-of-function mutation in the sodium channel gene Scn2a results in seizures and behavioral abnormalities. *Neuroscience* **102**, 307–317 (2001).

104. Kile, K. B., Tian, N. & Durand, D. M. Scn2a Sodium Channel Mutation Results in Hyperexcitability in the Hippocampus in vitro. *Epilepsia* **49**, 488–499 (2008).

105. Escayg, A. *et al.* A novel SCN1A mutation associated with generalized epilepsy with febrile seizures plus--and prevalence of variants in patients with epilepsy. *Am. J. Hum. Genet.* **68**, 866–873 (2001).

106. Weiss, L. A. *et al.* Sodium channels SCN1A, SCN2A and SCN3A in familial autism. *Mol. Psychiatry* **8**, 186–194 (2003).

107. Veeramah, K. R. *et al.* De novo pathogenic SCN8A mutation identified by whole-genome sequencing of a family quartet affected by infantile epileptic encephalopathy and SUDEP. *Am. J. Hum. Genet.* **90**, 502–510 (2012).

108. Steward, C. A. *et al.* Genome annotation for clinical genomic diagnostics: strengths and weaknesses. *Genome Med.* **9**, 49 (2017).

109. Møller, R. S. *et al.* Gene Panel Testing in Epileptic Encephalopathies and Familial Epilepsies. *Mol. Syndromol.* **7**, 210–219 (2016).

110. Ogiwara, I. *et al.* Nav1.2 haplodeficiency in excitatory neurons causes absence-like seizures in mice. *Commun. Biol.* **1**, 1–16 (2018).

111. Léna, I. & Mantegazza, M. NaV1.2 haploinsufficiency in Scn2a knock-out mice causes an autistic-like phenotype attenuated with age. *Sci. Rep.* **9**, 12886 (2019).

112. Tatsukawa, T. *et al.* Scn2a haploinsufficient mice display a spectrum of phenotypes affecting anxiety, sociability, memory flexibility and ampakine CX516 rescues their hyperactivity. *Mol. Autism* **10**, 15 (2019).

113. Mishra, V. *et al.* Scn2a deletion improves survival and brain–heart dynamics in the Kcna1-null mouse model of sudden unexpected death in epilepsy (SUDEP). *Hum. Mol. Genet.* **26**, 2091–2103 (2017).

114. Wang, H.-G. *et al. Scn2a* severe hypomorphic mutation decreases excitatory synaptic input and causes autism-associated behaviors. *JCI Insight* **6**, (2021).

115. Indumathy, J., Pruitt, A., Gautier, N. M., Crane, K. & Glasscock, E. Kv1.1 deficiency alters repetitive and social behaviors in mice and rescues autistic-like behaviors due to Scn2a haploinsufficiency. *Brain Behav.* **11**, (2021).

116. Shin, W. *et al.* Scn2a Haploinsufficiency in Mice Suppresses Hippocampal Neuronal Excitability, Excitatory Synaptic Drive, and Long-Term Potentiation, and Spatial Learning and Memory. *Front. Mol. Neurosci.* **12**, 145 (2019).

117. Eaton, M. *et al.* Generation and basic characterization of a gene-trap knockout mouse model of Scn2a with a substantial reduction of voltage-gated sodium channel Nav1.2 expression. *Genes Brain Behav.* **20**, e12725 (2021).

118. Troublesome variability in mouse studies. *Nat. Neurosci.* **12**, 1075–1075 (2009).

119. Saré, R. M., Lemons, A. & Smith, C. B. Behavior Testing in Rodents: Highlighting Potential Confounds Affecting Variability and Reproducibility. *Brain Sci.* **11**, 522 (2021).

120. Silverman, J. L., Yang, M., Lord, C. & Crawley, J. N. Behavioural phenotyping assays for mouse models of autism. *Nat. Rev. Neurosci.* **11**, 490–502 (2010).

121. Barak, B. & Feng, G. Neurobiology of social behavior abnormalities in autism and Williams syndrome. *Nat. Neurosci.* **19**, 647–655 (2016).

122. Chao, H.-T. *et al.* GABAergic dysfunction mediates autism-like stereotypies and Rett syndrome phenotypes. *Nature* **468**, 263–269 (2010).

123. Mejias, R. *et al.* Gain-of-function glutamate receptor interacting protein 1 variants alter GluA2 recycling and surface distribution in patients with autism. *Proc. Natl. Acad. Sci. U. S. A.* **108**, 4920–4925 (2011).

124. Kadam, S. D. *et al.* Methodological standards and interpretation of video-electroencephalography in adult control rodents. A TASK1-WG1 report of the AES/ILAE Translational Task Force of the ILAE. *Epilepsia* **58**, 10–27 (2017).

125. Spratt, P. W. E. *et al.* Paradoxical hyperexcitability from NaV1.2 sodium channel loss in neocortical pyramidal cells. *Cell Rep.* **36**, 109483 (2021).

126. Zhang, J. *et al.* Severe deficiency of the voltage-gated sodium channel NaV1.2 elevates neuronal excitability in adult mice. *Cell Rep.* **36**, 109495 (2021).

127. Liao, Y. *et al.* SCN2A mutation associated with neonatal epilepsy, late-onset episodic ataxia, myoclonus, and pain. *Neurology* **75**, 1454–1458 (2010).

128. Schattling, B. *et al.* Activity of NaV1.2 promotes neurodegeneration in an animal model of multiple sclerosis. *JCI Insight* **1**, e89810.

129. Schob, S.-C. Characterization of hippocampal network activity and pharmacological pilot study in a Scn2a epilapsy mouse model. (University of Hamberg, 2018).

130. Heinemann, S., Heinrich, T., Stühmer, W., Imoto, K. & Numa, S. Calcium Channel Characteristics Conferred on the Sodium Channel by Single Mutations. *Nature* **356**, 441–443 (1992).

131. Favre, I., Moczydlowski, E. & Schild, L. On the structural basis for ionic selectivity among Na+, K+, and Ca2+ in the voltage-gated sodium channel. *Biophys. J.* **71**, 3110–3125 (1996).

132. Schlief, T., Schönherr, R., Imoto, K. & Heinemann, S. H. Pore properties of rat brain II sodium channels mutated in the selectivity filter domain. *Eur. Biophys. J. EBJ* **25**, 75–91 (1996).

133. Terlau, H. *et al.* Mapping the site of block by tetrodotoxin and saxitoxin of sodium channel II. *FEBS Lett.* **293**, 93–96 (1991).

134. Fozzard, H. A. & Lipkind, G. M. The Tetrodotoxin Binding Site Is within the Outer Vestibule of the Sodium Channel. *Mar. Drugs* **8**, 219–234 (2010).

135. Shao, D., Okuse, K. & Djamgoz, M. B. A. Protein–protein interactions involving voltage-gated sodium channels: Post-translational regulation, intracellular trafficking and functional expression. *Int. J. Biochem. Cell Biol.* **41**, 1471–1481 (2009).

136. Beery, A. K. & Zucker, I. Sex Bias in Neuroscience and Biomedical Research. *Neurosci. Biobehav. Rev.* **35**, 565–572 (2011).

137. Shansky, R. M. & Woolley, C. S. Considering Sex as a Biological Variable Will Be Valuable for Neuroscience Research. *J. Neurosci.* **36**, 11817–11822 (2016).

138. Rocks, D. *et al.* Sex-specific multi-level 3D genome dynamics in the mouse brain. *Nat. Commun.* **13**, 3438 (2022).

139. Rocks, D., Cham, H. & Kundakovic, M. Why the estrous cycle matters for neuroscience. *Biol. Sex Differ.* **13**, 62 (2022).

140. Miguel-Aliaga, I. Let’s talk about (biological) sex. *Nat. Rev. Mol. Cell Biol.* **23**, 227–228 (2022).

141. Gender EURO. https://www.who.int/europe/health-topics/gender.

142. Manandhar, M., Hawkes, S., Buse, K., Nosrati, E. & Magar, V. Gender, health and the 2030 agenda for sustainable development. *Bull. World Health Organ.* **96**, 644–653 (2018).

143. Savic, I. Sex differences in human epilepsy. *Exp. Neurol.* **259**, 38–43 (2014).

144. Jacquemont, S. *et al.* A Higher Mutational Burden in Females Supports a “Female Protective Model” in Neurodevelopmental Disorders. *Am. J. Hum. Genet.* **94**, 415–425 (2014).

145. Werling, D. M. & Geschwind, D. H. Sex differences in autism spectrum disorders. *Curr. Opin. Neurol.* **26**, 146–153 (2013).

146. Rietschel, L. *et al.* Clinical high risk for psychosis: gender differences in symptoms and social functioning. *Early Interv. Psychiatry* **11**, 306–313 (2017).

147. Christian, C. A., Reddy, D. S., Maguire, J. & Forcelli, P. A. Sex Differences in the Epilepsies and Associated Comorbidities: Implications for Use and Development of Pharmacotherapies. *Pharmacol. Rev.* **72**, 767–800 (2020).

148. Reddy, D. S., Thompson, W. & Calderara, G. Molecular mechanisms of sex differences in epilepsy and seizure susceptibility in chemical, genetic and acquired epileptogenesis. *Neurosci. Lett.* **750**, 135753 (2021).

149. McHugh, J. C. & Delanty, N. Chapter 2 Epidemiology and Classification of Epilepsy: Gender Comparisons. in *International Review of Neurobiology* vol. 83 11–26 (Academic Press, 2008).

150. Fombonne, E. Epidemiology of Pervasive Developmental Disorders. *Pediatr. Res.* **65**, 591–598 (2009).

151. Virkud, Y. V., Todd, R. D., Abbacchi, A. M., Zhang, Y. & Constantino, J. N. Familial Aggregation of Quantitative Autistic Traits in Multiplex versus Simplex Autism. *Am. J. Med. Genet. Part B Neuropsychiatr. Genet. Off. Publ. Int. Soc. Psychiatr. Genet.* **150B**, 328–334 (2009).

152. Gockley, J. *et al.* The female protective effect in autism spectrum disorder is not mediated by a single genetic locus. *Mol. Autism* **6**, 25 (2015).

153. Werling, D. M. The role of sex-differential biology in risk for autism spectrum disorder. *Biol. Sex Differ.* **7**, 58 (2016).

154. Baron-Cohen, S. The extreme male brain theory of autism. *Trends Cogn. Sci.* **6**, 248–254 (2002).

155. Newmark, M. E. & Penry, J. K. Catamenial Epilepsy: A Review. *Epilepsia* **21**, 281–300 (1980).

156. Reddy, D. S. Role of neurosteroids in catamenial epilepsy. *Epilepsy Res.* **62**, 99–118 (2004).

157. Herzog, A. G. & Fowler, K. M. Sensitivity and Specificity of the Association Between Catamenial Seizure Patterns and Ovulation. *Neurology* **70**, 486–487 (2008).

158. Reddy, D. S. The Role of Neurosteroids in the Pathophysiology and Treatment of Catamenial Epilepsy. *Epilepsy Res.* **85**, 1–30 (2009).

159. Herzog, A. G. Progesterone therapy in women with epilepsy: A 3-year follow-up. *Neurology* **52**, 1917-a (1999).

160. Velíšková, J. & DeSantis, K. A. Sex and Hormonal influences on Seizures and Epilepsy. *Horm. Behav.* **63**, 267–277 (2013).

161. Beck, J. A. *et al.* Genealogies of mouse inbred strains. *Nat. Genet.* **24**, 23–25 (2000).

162. Crawley, J. N. *et al.* Behavioral phenotypes of inbred mouse strains: implications and recommendations for molecular studies. *Psychopharmacology (Berl.)* **132**, 107–124 (1997).

163. Bergren, S. K., Chen, S., Galecki, A. & Kearney, J. A. Genetic modifiers affecting severity of epilepsy caused by mutation of sodium channel Scn2a. *Mamm. Genome Off. J. Int. Mamm. Genome Soc.* **16**, 683–690 (2005).

164. Connor, J. X. *et al.* Genetic modifiers of the Kvβ2-null phenotype in mice. *Genes Brain Behav.* **4**, 77–88 (2005).

165. Frankel, W. N., Mahaffey, C. L., McGarr, T. C., Beyer, B. J. & Letts, V. A. Unraveling Genetic Modifiers in the Gria4 Mouse Model of Absence Epilepsy. *PLoS Genet.* **10**, (2014).

166. Kehrl, J. M. *et al.* Gain-of-function mutation in Gnao1: A murine model of epileptiform encephalopathy (EIEE17)? *Mamm. Genome* **25**, 202–210 (2014).

167. Miller, A. R., Hawkins, N. A., McCollom, C. E. & Kearney, J. A. Mapping genetic modifiers of survival in a mouse model of Dravet syndrome. *Genes Brain Behav.* **13**, 163–172 (2014).

168. Brandt, C., Bankstahl, M., Töllner, K., Klee, R. & Löscher, W. The pilocarpine model of temporal lobe epilepsy: Marked intrastrain differences in female Sprague–Dawley rats and the effect of estrous cycle. *Epilepsy Behav.* **61**, 141–152 (2016).

169. Thompson, C. H., Hawkins, N. A., Kearney, J. A. & George, A. L. CaMKII modulates sodium current in neurons from epileptic Scn2a mutant mice. *Proc. Natl. Acad. Sci.* **114**, 1696–1701 (2017).

170. Santos, V. R., Kobayashi, I., Hammack, R., Danko, G. & Forcelli, P. A. Impact of strain, sex, and estrous cycle on gamma butyrolactone-evoked absence seizures in rats. *Epilepsy Res.* **147**, 62–70 (2018).

171. Ryan, L. J. Characterization of cortical spindles in DBA/2 and C57BL/6 inbred mice. *Brain Res. Bull.* **13**, 549–558 (1984).

172. Ferraro, T. N., Golden, G. T., Smith, G. G. & Berrettini, W. H. Differential Susceptibility to Seizures Induced by Systemic Kainic Acid Treatment in Mature DBA/2J and C57BLl6J Mice. *Epilepsia* **36**, 301–307 (1995).

173. Ferraro, T. N. *et al.* Mapping murine loci for seizure response to kainic acid. *Mamm. Genome* **8**, 200–208 (1997).

174. Ferraro, T. N. *et al.* Quantitative Genetic Study of Maximal Electroshock Seizure Threshold in Mice: Evidence for a Major Seizure Susceptibility Locus on Distal Chromosome 1. *Genomics* **75**, 35–42 (2001).

175. Bessaih, T. *et al.* Quantitative trait locus on distal Chromosome 1 regulates the occurrence of spontaneous Spike Wave Discharges in DBA/2 mice. *Epilepsia* **53**, 1429–1435 (2012).

176. Kearney, J. A. *et al.* Severe epilepsy resulting from genetic interaction between Scn2a and Kcnq2. *Hum. Mol. Genet.* **15**, 1043–1048 (2006).

177. Martin, M. S. *et al.* The voltage-gated sodium channel Scn8a is a genetic modifier of severe myoclonic epilepsy of infancy. *Hum. Mol. Genet.* **16**, 2892–2899 (2007).

178. Bergren, S. K., Rutter, E. D. & Kearney, J. A. Fine mapping of an epilepsy modifier gene on mouse Chromosome 19. *Mamm. Genome Off. J. Int. Mamm. Genome Soc.* **20**, 359–366 (2009).

179. Hawkins, N. A., Martin, M. S., Frankel, W. N., Kearney, J. A. & Escayg, A. Neuronal voltage-gated ion channels are genetic modifiers of generalized epilepsy with febrile seizures plus. *Neurobiol. Dis.* **41**, 655–660 (2011).

180. Jorge, B. S. *et al.* Voltage-gated potassium channel KCNV2 (Kv8.2) contributes to epilepsy susceptibility. *Proc. Natl. Acad. Sci. U. S. A.* **108**, 5443–5448 (2011).

181. Hawkins, N. A. & Kearney, J. A. Confirmation of an Epilepsy Modifier Locus on Mouse Chromosome 11 and Candidate Gene Analysis by RNA-Seq. *Genes Brain Behav.* **11**, 452–460 (2012).

182. Calhoun, J. D., Hawkins, N. A., Zachwieja, N. J. & Kearney, J. A. Cacna1g is a genetic modifier of epilepsy caused by mutation of voltage-gated sodium channel Scn2a. *Epilepsia* **57**, e103-107 (2016).

183. Hawkins, N. A. & Kearney, J. A. Hlf is a genetic modifier of epilepsy caused by voltage-gated sodium channel mutations. *Epilepsy Res.* **119**, 20–23 (2016).

184. Echevarria-Cooper, D. M. *et al.* Cellular and behavioral effects of altered NaV1.2 sodium channel ion permeability in Scn2aK1422E mice. *Hum. Mol. Genet.* ddac087 (2022) doi:10.1093/hmg/ddac087.

185. Adney, S. K. *et al.* Functional and pharmacological evaluation of a novel SCN2A variant linked to early-onset epilepsy. *Ann. Clin. Transl. Neurol.* **7**, 1488–1501 (2020).

186. DeKeyser, J.-M., Thompson, C. H. & George, A. L. Cryptic prokaryotic promoters explain instability of recombinant neuronal sodium channels in bacteria. *J. Biol. Chem.* **296**, 100298 (2021).

187. Thompson, C. H., Kahlig, K. M. & George, A. L. SCN1A Splice Variants Exhibit Divergent Sensitivity to Commonly Used Antiepileptic Drugs. *Epilepsia* **52**, 1000–1009 (2011).

188. Lossin, C., Wang, D. W., Rhodes, T. H., Vanoye, C. G. & George, A. L. Molecular Basis of an Inherited Epilepsy. *Neuron* **34**, 877–884 (2002).

189. Thompson, C. H., Porter, J. C., Kahlig, K. M., Daniels, M. A. & George, A. L. Nontruncating SCN1A Mutations Associated with Severe Myoclonic Epilepsy of Infancy Impair Cell Surface Expression. *J. Biol. Chem.* **287**, 42001–42008 (2012).

190. Hamill, O. P., Marty, A., Neher, E., Sakmann, B. & Sigworth, F. J. Improved patch-clamp techniques for high-resolution current recording from cells and cell-free membrane patches. *Pflüg. Arch. - Eur. J. Physiol.* **391**, 85–100 (1981).

191. Sert, N. P. du *et al.* The ARRIVE guidelines 2.0: Updated guidelines for reporting animal research. *PLOS Biol.* **18**, e3000410 (2020).

192. Milescu, L. S., Bean, B. P. & Smith, J. C. Isolation of Somatic Na+ Currents by Selective Inactivation of Axonal Channels with a Voltage Prepulse. *J. Neurosci.* **30**, 7740–7748 (2010).

193. Mistry, A. M. *et al.* Strain- and Age-dependent Hippocampal Neuron Sodium Currents Correlate with Epilepsy Severity in Dravet Syndrome Mice. *Neurobiol. Dis.* **65**, 1–11 (2014).

194. Hallermann, S., de Kock, C. P. J., Stuart, G. J. & Kole, M. H. P. State and location dependence of action potential metabolic cost in cortical pyramidal neurons. *Nat. Neurosci.* **15**, 1007–1014 (2012).

195. Lipkin, A. M., Cunniff, M. M., Spratt, P. W. E., Lemke, S. M. & Bender, K. J. Functional Microstructure of CaV-Mediated Calcium Signaling in the Axon Initial Segment. *J. Neurosci.* **41**, 3764–3776 (2021).

196. Hawkins, N. A., Zachwieja, N. J., Miller, A. R., Anderson, L. L. & Kearney, J. A. Fine Mapping of a Dravet Syndrome Modifier Locus on Mouse Chromosome 5 and Candidate Gene Analysis by RNA-Seq. *PLoS Genet.* **12**, (2016).

197. Shepherd, J. K., Grewal, S. S., Fletcher, A., Bill, D. J. & Dourish, C. T. Behavioural and pharmacological characterisation of the elevated ‘zero-maze’ as an animal model of anxiety. *Psychopharmacology (Berl.)* **116**, 56–64 (1994).

198. Yang, M. & Crawley, J. N. Simple Behavioral Assessment of Mouse Olfaction. 14 (2010).
199. Naylor, C. E. *et al.* Molecular basis of ion permeability in a voltage-gated sodium channel. *EMBO J.* **35**, 820–830 (2016).
200. Schmalhofer, W. A. *et al.* A K_{V} 2.1 gating modifier binding assay suitable for high throughput screening. *Channels* **3**, 437–447 (2009).
201. Geiger, J. R. P. & Jonas, P. Dynamic Control of Presynaptic Ca2+ Inflow by Fast-Inactivating K+ Channels in Hippocampal Mossy Fiber Boutons. *Neuron* **28**, 927–939 (2000).
202. Ritzau-Jost, A. *et al.* Ultrafast Action Potentials Mediate Kilohertz Signaling at a Central Synapse. *Neuron* **84**, 152–163 (2014).
203. Rowan, M. J. M., Tranquil, E. & Christie, J. M. Distinct Kv Channel Subtypes Contribute to Differences in Spike Signaling Properties in the Axon Initial Segment and Presynaptic Boutons of Cerebellar Interneurons. *J. Neurosci.* **34**, 6611–6623 (2014).
204. Filipis, L. & Canepari, M. Optical measurement of physiological sodium currents in the axon initial segment. *J. Physiol.* **599**, 49–66 (2021).
205. Hanemaaijer, N. A. *et al.* Ca2+ entry through NaV channels generates submillisecond axonal Ca2+ signaling. *eLife* **9**, e54566 (2020).
206. Ferland, R. J. The Repeated Flurothyl Seizure Model in Mice. *Bio-Protoc.* **7**, (2017).
207. Wen, H. & Levitan, I. B. Calmodulin Is an Auxiliary Subunit of KCNQ2/3 Potassium Channels. *J. Neurosci.* **22**, 7991–8001 (2002).
208. Kim, J. *et al.* Calmodulin Mediates Ca2+ Sensitivity of Sodium Channels*. *J. Biol. Chem.* **279**, 45004–45012 (2004).
209. Swain, S. M., Sahoo, N., Dennhardt, S., Schönherr, R. & Heinemann, S. H. Ca(2+)/calmodulin regulates Kvβ1.1-mediated inactivation of voltage-gated K(+) channels. *Sci. Rep.* **5**, 15509 (2015).

210. Clarkson, R. L., Liptak, A. T., Gee, S. M., Sohal, V. S. & Bender, K. J. D3 Receptors Regulate Excitability in a Unique Class of Prefrontal Pyramidal Cells. *J. Neurosci.* **37**, 5846–5860 (2017).

211. Vacher, H., Mohapatra, D. P. & Trimmer, J. S. Localization and Targeting of Voltage-Dependent Ion Channels in Mammalian Central Neurons. *Physiol. Rev.* **88**, 1407–1447 (2008).

212. Zhu, Y., Li, D. & Huang, H. Activity and Cytosolic Na+ Regulate Synaptic Vesicle Endocytosis. *J. Neurosci.* **40**, 6112–6120 (2020).

213. Stanley, E. F. The Nanophysiology of Fast Transmitter Release. *Trends Neurosci.* **39**, 183–197 (2016).

214. Burke, K. J. & Bender, K. J. Modulation of Ion Channels in the Axon: Mechanisms and Function. *Front. Cell. Neurosci.* **13**, 221 (2019).

215. Letts, V. A., Beyer, B. J. & Frankel, W. N. Hidden in plain sight – Spike-wave discharges in mouse inbred strains. *Genes Brain Behav.* **13**, 519–526 (2014).

216. Amador, A. *et al.* Modelling and treating GRIN2A developmental and epileptic encephalopathy in mice. *Brain* **143**, 2039–2057 (2020).

217. Sah, M. *et al.* Altered excitatory transmission onto hippocampal interneurons in the IQSEC2 mouse model of X-linked neurodevelopmental disease. *Neurobiol. Dis.* **137**, 104758 (2020).

218. Papale, L. A. *et al.* Heterozygous mutations of the voltage-gated sodium channel SCN8A are associated with spike-wave discharges and absence epilepsy in mice. *Hum. Mol. Genet.* **18**, 1633–1641 (2009).

219. Woolley, C. S. Estradiol Facilitates Kainic Acid—Induced, but not Flurothyl-Induced, Behavioral Seizure Activity in Adult Female Rats. *Epilepsia* **41**, 510–515 (2000).

220. Scharfman, H. E. *et al.* Seizure susceptibility in intact and ovariectomized female rats treated with the convulsant pilocarpine. *Exp. Neurol.* **196**, 73–86 (2005).

221. Gangisetty, O. & Reddy, D. S. Neurosteroid withdrawal regulates GABA-A receptor α4-subunit expression and seizure susceptibility by activation of progesterone receptor-independent early growth response factor-3 pathway. *Neuroscience* **170**, 865–880 (2010).

222. Kight, K. E. & McCarthy, M. M. Using sex differences in the developing brain to identify nodes of influence for seizure susceptibility and epileptogenesis. *Neurobiol. Dis.* **72**, 136–143 (2014).

223. Joshi, S. & Kapur, J. Neurosteroid regulation of GABAA receptors: A role in catamenial epilepsy. *Brain Res.* **1703**, 31–40 (2019).

224. Li, J., Leverton, L. K., Naganatanahalli, L. M. & Christian-Hinman, C. A. Seizure burden fluctuates with the female reproductive cycle in a mouse model of chronic temporal lobe epilepsy. *Exp. Neurol.* **334**, 113492 (2020).

225. Herzog, A. G. Disorders of reproduction in patients with epilepsy: Primary neurological mechanisms. *Seizure* **17**, 101–110 (2008).

226. Finn, D. A. & Gee, K. W. The estrus cycle, sensitivity to convulsants and the anticonvulsant effect of a neuroactive steroid. *J. Pharmacol. Exp. Ther.* **271**, 164–170 (1994).

227. Riazi, K. *et al.* Sex and Estrus Cycle Differences in the Modulatory Effects of Morphine on Seizure Susceptibility in Mice. *Epilepsia* **45**, 1035–1042 (2004).

228. Maguire, J. L., Stell, B. M., Rafizadeh, M. & Mody, I. Ovarian cycle–linked changes in GABAA receptors mediating tonic inhibition alter seizure susceptibility and anxiety. *Nat. Neurosci.* **8**, 797–804 (2005).

229. Reddy, D. S., Gould, J. & Gangisetty, O. A Mouse Kindling Model of Perimenstrual Catamenial Epilepsy. *J. Pharmacol. Exp. Ther.* **341**, 784–793 (2012).

230. Li, J. *et al.* Dynamic and Sex-Specific Changes in Gonadotropin-Releasing Hormone Neuron Activity and Excitability in a Mouse Model of Temporal Lobe Epilepsy. *eNeuro* **5**, (2018).

231. van Luijtelaar, G. *et al.* The ovarian hormones and absence epilepsy: a long-term EEG study and pharmacological effects in a genetic absence epilepsy model. *Epilepsy Res.* **46**, 225–239 (2001).

232. D'Amour, J. *et al.* Interictal spike frequency varies with ovarian cycle stage in a rat model of epilepsy. *Exp. Neurol.* **269**, 102–119 (2015).

233. Gegenhuber, B., Wu, M. V., Bronstein, R. & Tollkuhn, J. Gene regulation by gonadal hormone receptors underlies brain sex differences. *Nature* 1–7 (2022) doi:10.1038/s41586-022-04686-1.

234. Pantier, L., Li, J. & Christian, C. Estrous Cycle Monitoring in Mice with Rapid Data Visualization and Analysis. *BIO-Protoc.* **9**, (2019).

235. Byers, S. L., Wiles, M. V., Dunn, S. L. & Taft, R. A. Mouse Estrous Cycle Identification Tool and Images. *PLOS ONE* **7**, e35538 (2012).

236. McLean, A. C., Valenzuela, N., Fai, S. & Bennett, S. A. L. Performing Vaginal Lavage, Crystal Violet Staining, and Vaginal Cytological Evaluation for Mouse Estrous Cycle Staging Identification. *JoVE J. Vis. Exp.* e4389 (2012) doi:10.3791/4389.

237. Nelson, J. F., Felicio, L. S., Randall, P. K., Sims, C. & Finch, C. E. A Longitudinal Study of Estrous Cyclicity in Aging C57BL/6J Mice: I. Cycle Frequency, Length and Vaginal Cytology1. *Biol. Reprod.* **27**, 327–339 (1982).

238. Li, J. *et al.* Disrupted female estrous cyclicity in the intrahippocampal kainic acid mouse model of temporal lobe epilepsy. *Epilepsia Open* **2**, 39–47 (2016).

239. Ng, K. Y., Yong, J. & Chakraborty, T. R. Estrous cycle in ob/ob and ovariectomized female mice and its relation with estrogen and leptin. *Physiol. Behav.* **99**, 125–130 (2010).

240. R Core Team. *R: A Language and Environment for Statistical Computing.* (R Foundation for Statistical Computing, 2021).

241. Maechler, M. *Hartigan's Dip Test Statistic for Unimodality – Corrected.* (2021).

242. Ameijeiras-Alonso, J., Crujeiras, R. M. & Rodriguez-Casal, A. **multimode** : An *R* Package for Mode Assessment. *J. Stat. Softw.* **97**, (2021).

243. Hartigan, J. A. & Hartigan, P. M. The Dip Test of Unimodality. *Ann. Stat.* **13**, 70–84 (1985).

244. Ameijeiras-Alonso, J., Crujeiras, R. M. & Rodríguez-Casal, A. Mode testing, critical bandwidth and excess mass. *TEST* **28**, 900–919 (2019).

245. Broestl, L. *et al.* Ovarian Cycle Stages Modulate Alzheimer-Related Cognitive and Brain Network Alterations in Female Mice. *eNeuro* **5**, (2018).

246. Fawley, J. A., Pouliot, W. A. & Dudek, F. E. Pilocarpine-induced status epilepticus and subsequent spontaneous seizures: lack of effect on the number of gonadotropin-releasing hormone-positive neurons in a mouse model of temporal lobe epilepsy. *Neuroscience* **203**, 153–159 (2012).

247. Edwards, H. E., Burnham, W. M., Ng, M. M., Asa, S. & MacLusky, N. J. Limbic Seizures Alter Reproductive Function in the Female Rat. *Epilepsia* **40**, 1370–1377 (1999).

248. Zwain, I. H. & Yen, S. S. C. Neurosteroidogenesis in Astrocytes, Oligodendrocytes, and Neurons of Cerebral Cortex of Rat Brain. *Endocrinology* **140**, 3843–3852 (1999).

249. Diotel, N. *et al.* Steroid Transport, Local Synthesis, and Signaling within the Brain: Roles in Neurogenesis, Neuroprotection, and Sexual Behaviors. *Front. Neurosci.* **12**, 84 (2018).

250. Falkenstein, E., Tillmann, H.-C., Christ, M., Feuring, M. & Wehling, M. Multiple Actions of Steroid Hormones—A Focus on Rapid, Nongenomic Effects. *Pharmacol. Rev.* **52**, 513–556 (2000).

251. deCatanzaro, D., Muir, C., Beaton, E. A. & Jetha, M. Non-invasive repeated measurement of urinary progesterone, 17β-estradiol, and testosterone in developing, cycling, pregnant, and postpartum female mice. *Steroids* **69**, 687–696 (2004).

252. Gebhart, V. M. *et al.* Estrogen receptors and sex hormone binding globulin in neuronal cells and tissue. *Steroids* **142**, 94–99 (2019).

253. Vasudevan, N. & Pfaff, D. W. Non-genomic actions of estrogens and their interaction with genomic actions in the brain. *Front. Neuroendocrinol.* **29**, 238–257 (2008).

254. Lathe, R. The individuality of mice. *Genes Brain Behav.* **3**, 317–327 (2004).

255. Racine, R. J. Modification of seizure activity by electrical stimulation: II. Motor seizure. *Electroencephalogr. Clin. Neurophysiol.* **32**, 281–294 (1972).

256. McLin, J. P. & Steward, O. Comparison of seizure phenotype and neurodegeneration induced by systemic kainic acid in inbred, outbred, and hybrid mouse strains. *Eur. J. Neurosci.* **24**, 2191–2202 (2006).

257. Schreiber, R. A. & Graham Jr., J. M. Audiogenic priming in DBA/2J and C57 BL/6J mice: Interactions among age, prime-to-test interval, and index of seizure. *Dev. Psychobiol.* **9**, 57–66 (1976).

258. Sangdee, P., Turkanis, S. A., Karler, R. & Sanchez, A. P. Kindling-like Effect Induced by Repeated Corneal Electro shock in Mice. *Epilepsia* **23**, 471–479 (1982).

259. Hawkins, N. A. *et al.* Screening of conventional anticonvulsants in a genetic mouse model of epilepsy. *Ann. Clin. Transl. Neurol.* **4**, 326–339 (2017).

260. Banko, M. L., Allen, K. M., Dolina, S., Neumann, P. E. & Seyfried, T. N. Genomic imprinting and audiogenic seizures in mice. *Behav. Genet.* **27**, 465–475 (1997).

261. Lawson, H. A., Cheverud, J. M. & Wolf, J. B. Genomic imprinting and parent-of-origin effects on complex traits. *Nat. Rev. Genet.* **14**, 609–617 (2013).

262. Lagarrigue, S. *et al.* Analysis of allele-specific expression in mouse liver by RNA-Seq: a comparison with Cis-eQTL identified using genetic linkage. *Genetics* **195**, 1157–1166 (2013).

263. Mott, R. *et al.* The Architecture of Parent-of-Origin Effects in Mice. *Cell* **156**, 332–342 (2014).

264. Isles, A. R. The contribution of imprinted genes to neurodevelopmental and neuropsychiatric disorders. *Transl. Psychiatry* **12**, 1–8 (2022).

265. Pinto, D. J., Patrick, S. L., Huang, W. C. & Connors, B. W. Initiation, Propagation, and Termination of Epileptiform Activity in Rodent Neocortex In Vitro Involve Distinct Mechanisms. *J. Neurosci.* **25**, 8131–8140 (2005).

266. Spring, M. G., Schoolcraft, K. D. & López, H. H. The effects of adolescent cannabinoid exposure on seizure susceptibility and lethality in adult male rats. *Neurotoxicol. Teratol.* **58**, 101–106 (2016).

267. Faingold, C. L., Randall, M. & Kommajosyula, S. P. Susceptibility to seizure-induced sudden death in DBA/2 mice is altered by adenosine. *Epilepsy Res.* **124**, 49–54 (2016).

268. Sugathan, A. *et al.* CHD8 regulates neurodevelopmental pathways associated with autism spectrum disorder in neural progenitors. *Proc. Natl. Acad. Sci. U. S. A.* **111**, E4468–E4477 (2014).

269. De Rubeis, S. *et al.* Synaptic, transcriptional, and chromatin genes disrupted in autism. *Nature* **515**, 209–215 (2014).

270. Sahly, A. N., Shevell, M., Sadleir, L. G. & Myers, K. A. SUDEP risk and autonomic dysfunction in genetic epilepsies. *Auton. Neurosci.* **237**, 102907 (2022).

271. Ryvlin, P. *et al.* Incidence and mechanisms of cardiorespiratory arrests in epilepsy monitoring units (MORTEMUS): a retrospective study. *Lancet Neurol.* **12**, 966–977 (2013).

272. Aiba, I. & Noebels, J. L. Spreading depolarization in the brainstem mediates sudden cardiorespiratory arrest in mouse SUDEP models. *Sci. Transl. Med.* **7**, 282ra46 (2015).

273. Glasscock, E., Qian, J., Yoo, J. W. & Noebels, J. L. Masking epilepsy by combining two epilepsy genes. *Nat. Neurosci.* **10**, 1554–1558 (2007).

274. Fletcher, C. F. *et al.* Absence Epilepsy in Tottering Mutant Mice Is Associated with Calcium Channel Defects. *Cell* **87**, 607–617 (1996).

275. Qian, J. & Noebels, J. L. Presynaptic Ca2+ Influx at a Mouse Central Synapse with Ca2+ Channel Subunit Mutations. *J. Neurosci.* **20**, 163–170 (2000).

276. Aiba, I., Wehrens, X. H. T. & Noebels, J. L. Leaky RyR2 channels unleash a brainstem spreading depolarization mechanism of sudden cardiac death. *Proc. Natl. Acad. Sci. U. S. A.* **113**, E4895–E4903 (2016).

277. Fill, M. & Copello, J. A. Ryanodine Receptor Calcium Release Channels. *Physiol. Rev.* **82**, 893–922 (2002).

278. Shen, H.-Y., Li, T. & Boison, D. A novel mouse model for sudden unexpected death in epilepsy (SUDEP): role of impaired adenosine clearance. *Epilepsia* **51**, 465–468 (2010).

279. Jefferys, J. G. R., Arafat, M. A., Irazoqui, P. P. & Lovick, T. A. Brainstem activity, apnea, and death during seizures induced by intrahippocampal kainic acid in anaesthetized rats. *Epilepsia* **60**, 2346–2358 (2019).

280. Biggers, J. D. & Claringbold, P. J. Why Use Inbred Lines? *Nature* **174**, 596–597 (1954).

281. Jensen, V. S., Porsgaard, T., Lykkesfeldt, J. & Hvid, H. Rodent model choice has major impact on variability of standard preclinical readouts associated with diabetes and obesity research. *Am. J. Transl. Res.* **8**, 3574–3584 (2016).

282. Tuttle, A. H., Philip, V. M., Chesler, E. J. & Mogil, J. S. Comparing phenotypic variation between inbred and outbred mice. *Nat. Methods* **15**, 994–996 (2018).

283. Begley, C. G. & Ellis, L. M. Raise standards for preclinical cancer research. *Nature* **483**, 531–533 (2012).

284. Threadgill, D. W., Miller, D. R., Churchill, G. A. & de Villena, F. P.-M. The collaborative cross: a recombinant inbred mouse population for the systems genetic era. *ILAR J.* **52**, 24–31 (2011).

285. Rosshart, S. P. *et al.* Laboratory mice born to wild mice have natural microbiota and model human immune responses. *Science* **365**, eaaw4361 (2019).

286. Graham, A. L. Naturalizing mouse models for immunology. *Nat. Immunol.* **22**, 111–117 (2021).

287. Prendergast, B. J., Onishi, K. G. & Zucker, I. Female mice liberated for inclusion in neuroscience and biomedical research. *Neurosci. Biobehav. Rev.* **40**, 1–5 (2014).

288. Becker, J. B., Prendergast, B. J. & Liang, J. W. Female rats are not more variable than male rats: a meta-analysis of neuroscience studies. *Biol. Sex Differ.* **7**, 34 (2016).

289. Maney, D. L. Perils and pitfalls of reporting sex differences. *Philos. Trans. R. Soc. B Biol. Sci.* **371**, 20150119 (2016).

290. Tabbaa, M., Knoll, A. & Levitt, P. Mouse population genetics phenocopies heterogeneity of human Chd8 haploinsufficiency. *Neuron* **0**, (2023).

291. Ashbrook, D. G. *et al.* A platform for experimental precision medicine: The extended BXD mouse family. *Cell Syst.* **12**, 235-247.e9 (2021).

292. Swanzey, E., O'Connor, C. & Reinholdt, L. G. Mouse Genetic Reference Populations: Cellular Platforms for Integrative Systems Genetics. *Trends Genet.* **37**, 251–265 (2021).

293. Florio, M. & Huttner, W. B. Neural progenitors, neurogenesis and the evolution of the neocortex. *Development* **141**, 2182–2194 (2014).

294. Mason, J. O. & Price, D. J. Building brains in a dish: Prospects for growing cerebral organoids from stem cells. *Neuroscience* **334**, 105–118 (2016).

295. Hodge, R. D. *et al.* Conserved cell types with divergent features in human versus mouse cortex. *Nature* **573**, 61–68 (2019).

296. Loomba, S. *et al.* Connectomic comparison of mouse and human cortex. *Science* **377**, eabo0924 (2022).

297. Beaulieu-Laroche, L. *et al.* Enhanced dendritic compartmentalization in human cortical neurons. *Cell* **175**, 643-651.e14 (2018).

298. Gidon, A. *et al.* Dendritic action potentials and computation in human layer 2/3 cortical neurons. *Science* **367**, 83–87 (2020).

299. Testa-Silva, G. *et al.* High synaptic threshold for dendritic NMDA spike generation in human layer 2/3 pyramidal neurons. *Cell Rep.* **41**, (2022).